Optically detected Electron Paramagnetic Resonance of Metalloproteins

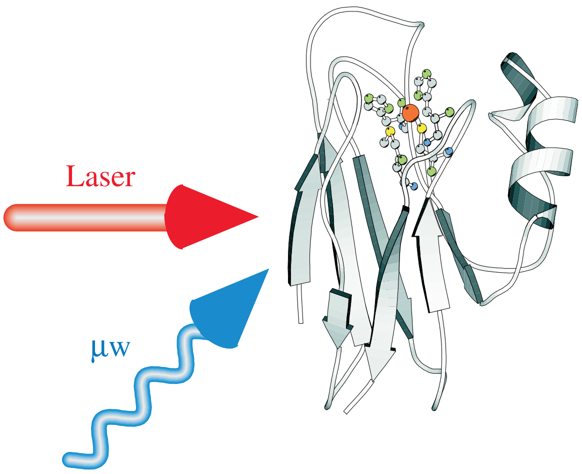

Dissertation for the degree of
Doktor der Naturwissenschaften
in the Fachbereich Physik
at the University of Dortmund

Birgit Börger-Enkisch

Dortmund, May 2001

Contents

Chapter 1

Introduction

Metalloproteins, that is proteins containing transition metal ions, play key roles in biochemical processes such as oxygen transport, respiration, photosynthesis, and nitrogen fixation. The extraordinary features of these interesting compounds are a result of the unusual geometric and electronic structures that can be imposed on the metal ion in a protein environment. The electronic structure of a metalloprotein characterizes the biological reactivity of the active site and the functional role of the protein. Thus, one of the major goals of research has been to understand the origin of the spectral features of metalloproteins in order to obtain detailed insight into the electronic structure of an active site. For this purpose a variety of experimental methods are often combined with a quantum mechanical model.

Numerous types of spectroscopy are currently used to study metalloproteins. Transition metal complexes often possess a paramagnetic ground state which can be investigated with electron paramagnetic resonance (EPR) spectroscopy. Low energy transitions between d-orbitals and high-energy charge-transfer transitions both contribute to the visible and infrared absorption spectra of the protein. Additional information is provided by magnetic circular dichroism spectroscopy (MCD), which measures the absorption of circularly polarised light in the presence of a magnetic field.

In this thesis, we present a new spectroscopic technique which uses electron paramagnetic resonance probed by a laser field and is thus called optically detected electron paramagnetic resonance spectroscopy (ODEPR). This technique is based on coherent Raman scattering but can also be conclusively interpreted in terms of a modulation of the incident laser beam by the transverse magnetisation. It is the objective of this thesis to demonstrate the application of ODEPR spectroscopy to the investigation of metalloproteins.

In Chapter 2 we give an introduction into the theoretical principles of EPR and MCD and discuss the theory of ODEPR signals. An introduction to related experiments combining magnetic resonance and optical methods is also provided. Chapter 3 discusses the experimental setup for ODEPR spectroscopy. Chapter 4 summarizes the behaviour of the ODEPR spectra as a function of wavelength of the laser. In addition, the influence of the polarisation of the detecting laser beam is discussed. These results firmly establish the interpretation of the experiment as analogous to coherent Raman scattering or transverse, microwave modulated MCD.

We use these results in the two following chapters, where the experimental findings from two well-characterized electron-transfer proteins and from synthetic model-complexes are presented. ODEPR spectra from the mononuclear copper protein, azurin, are discussed in Chapter 5. We present ODEPR spectra measured over a wide range of the visible and infrared spectrum. These results are compared with experimental spectra from conventional EPR and MCD spectroscopy and are related to a theoretical model. By means of ODEPR, we are able to deconvolute the optical spectrum and to extract new information about the polarisation of the individual optical bands relative to the magnetic axes. In the same chapter, results from synthetic copper compounds are compared with the results from azurin.

EPR and ODEPR spectra from the charge-transfer bands of the high-spin iron protein, rubredoxin, are shown in Chapter 6. A novel model is presented to fit the features of the rubredoxin EPR spectrum. This model is applied to the interpretation of the ODEPR spectra, which allows us to investigate the polarisations of the optical transitions and to relate the magnetic and optical anisotropies.

The results of this thesis show that ODEPR spectroscopy can yield information about the electronic structure of metalloproteins which cannot be gained with other methods. Therefore, this new spectroscopic technique can contribute to our current knowlegde of biological systems. This work comprises fundamental research in chemical and optical physics but has also implications for biochemistry.

Chapter 2

Principles

2.1 Electron Paramagnetic Resonance

2.1.1 The Resonance Phenomenon

Electron paramagnetic resonance (EPR) spectroscopy is a widely employed method suitable for the investigation of paramagnetic substances, such as transition metal ions or free radicals [1, 2, 3, 4, 5]. These species possess an odd number of electrons or a partly filled inner shell. The unpaired electrons give rise to a permanent magnetic moment $\vec{\mu}$ of the atom. $\vec{\mu}$ consists of contributions from the orbital $\hbar L$ and the spin angular momentum $\hbar S$, such that

$$\vec{\mu} = -g\mu_B \vec{J} \quad \text{with} \quad \vec{J} = \vec{L} + \vec{S}, \tag{2.1}$$

where μ_B is the Bohr magneton and g the g-value. In the simplest case where the magnetic moment arises solely from the spin of one free electron, the g-value is approximately 2.

The interaction of the magnetic moment with an applied static magnetic field $\vec{B}_0$ is described by a Hamiltonian of the following form:

$$\mathcal{H} = g\mu_B \vec{B}_0 \vec{J}. \tag{2.2}$$

If the magnetic field is applied along the laboratory z-axis, we find two eigenvalues of the Hamiltonian, which lead to two different energy levels $\pm\frac{1}{2}g\mu_B B_0$, as indicated in Fig. 2.1. In a sample containing many paramagnetic centres these levels are thermally populated according to Boltzmann's law; this is indicated by the shaded circles in the Figure.

Transitions between the states are excited with a radiation of frequency $\omega_{mw} = \omega_0$. The EPR resonance condition is therefore

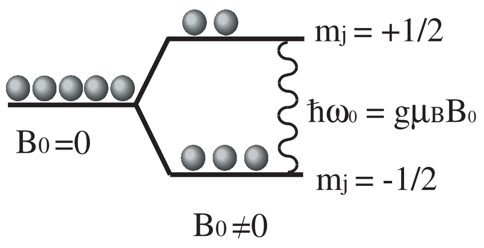

Figure 2.1: *A magnetic field B_0 induces a Zeeman splitting. A transition of the electron spin can be induced with a microwave field of frequency $\omega_{mw} = \omega_0$.*

$$E = \hbar\omega_0 = g\mu_B B_0, \tag{2.3}$$

where ω_0 is called the Larmor frequency.

Common radiation sources used in EPR spectroscopy are oscillators creating microwave radiation ($\omega_{mw}/2\pi = 1$ to 100 GHz). For technical reasons the frequency is kept constant, while the magnetic field is scanned until the magnetic resonance condition is reached.

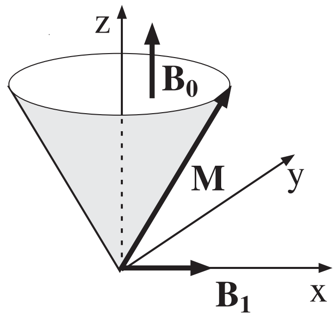

Figure 2.2: *A microwave field B_1 creates a precession of the magnetisation M about the static magnetic field B_0.*

In presence of a static magnetic field only certain equilibrium positions of the magnetic moments with respect to the field are possible. The vector sum of all magnetic moments normalized to a certain volume of a sample is the magnetisation M. If B_0 is applied along the laboratory z-axis, the magnetisation will also point along z. If a continuous wave microwave field B_1 with frequency ω_{mw} is applied perpendicular to B_0, the magnetisation will be moved away from its equilibrium position and start to precess around the z-axis with ω_{mw}, as indicated in Fig. 2.2. On a basic level these dynamics are described by the Bloch equations. The Bloch equations are particularly simple in a coordinate system rotating at the same frequency as the magnetisation. In the “rotating reference frame” we find in absence of saturation for the transverse components of the magnetisation, M_a and M_d, as a function of the frequency ω_{mw} [5, 3]:

$$M_d = \frac{(\omega_0 - \omega_{mw})T_2}{1 + (\omega_{mw} - \omega_0)^2 T_2^2}\,\omega_0 T_2\,\frac{B_1 M_0}{B_0} \tag{2.4}$$

$$M_a = \frac{1}{1 + (\omega_{mw} - \omega_0)^2 T_2^2}\,\omega_0 T_2\,\frac{B_1 M_0}{B_0}. \tag{2.5}$$

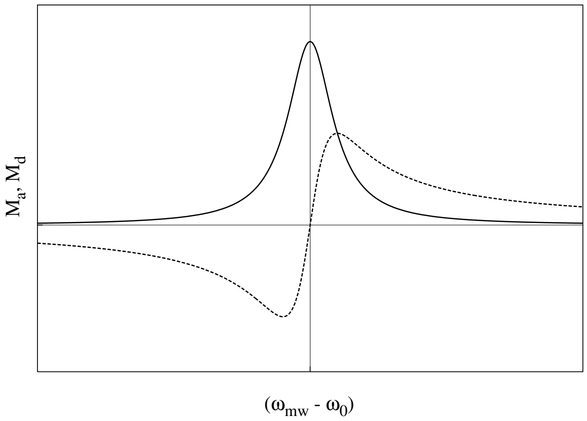

Figure 2.3: *Transverse components of the magnetisation as a function of* $(\omega_{mw} - \omega_0)$. M_a: *absorption lineshape (solid line).* M_d: *dispersion lineshape (dashed line).*

The interaction of the magnetisation with the surrounding lattice is introduced phenomenologically via the spin-lattice relaxation time T_1 and the phase memory time T_2, which determines the linewidth of the resonance. M_0 is the equilibrium magnetisation. Inspection of these equations shows that the M_a-component has its maximum in resonance where $\omega_{mw} = \omega_0$. The component M_d, which rotates perpendicular to M_a, is zero in resonance. The behaviour of both components as a function of $\omega_{mw} - \omega_0$ is depicted in Fig. 2.3. Although normally only the absorption component M_a is measured in a conventional EPR experiment, the dispersion component M_d contains in principle the same information as M_a since both are linked by Kramers-Kronig integral transforms.

A Lorentzian lineshape as predicted by the Bloch-equations is rarely observed in reality. Due to anisotropy, inhomogenous broadening, and saturation the lineshape is frequently much more complicated. Nevertheless, these obscured lines can normally be decomposed into single Lorentzian or Gaussian resonance lines. Thus, absorption and dispersion oscillating with a $\pi/2$ phase difference are an important concept for the understanding of EPR and ODEPR spectra.

2.1.2 The Spin Hamiltonian and Anisotropy

A paramagnetic ion in a molecule is surrounded by diamagnetic atoms imposing a local symmetry on the ion. Frequently the orbital angular momentum contributes to the magnetic moment of a paramagnetic ion only via spin-orbit coupling. This effect is usually incorporated in the g-value, which as a consequence deviates from the free electron value. If the local environment of an ion is anisotropic, this leads to different g-values along the different symmetry axes of the molecule. A suitable spin Hamiltonian expressing the

Zeeman-interaction for an ion with S=1/2 in an anisotropic environment is [2, 3]

$$\mathcal{H} = \mu_B B_0 (g_x S_x \sin\theta \cos\phi + g_y S_y \sin\theta \sin\phi + g_z S_z \cos\theta). \qquad (2.6)$$

The orientation angles θ and ϕ describe the components of the magnetic field along each molecular axis. θ is the angle between B_0 and the molecular z-axis and ϕ is the angle between the projection of B_0 onto the molecular xy-plane and the molecular x-axis. Additional terms may appear in the Hamiltonian if S>1/2, or if hyperfine interaction, electron-electron interactions and other types of interactions contribute to the spectrum. If the spin Hamiltonian is known, the eigenvalues of the system dependent on the orientation of the molecule with respect to B_0 can be determined. On the other hand, if the general form of the Hamiltonian could be determined, the exact values of the appearing constants can be extracted from the experimental spectrum. In general, the spin Hamiltonian is a very important tool for the detailed analysis of the eperimentally obtained EPR spetra.

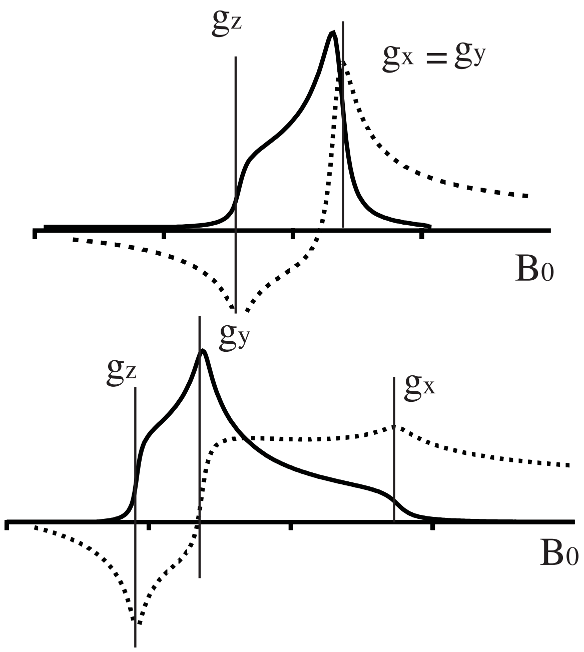

Figure 2.4: *Upper trace: Calculated powder-like EPR absorption and dispersion spectrum for S=1/2 and axial symmetry. Lower trace: Calculated powder-like EPR absorption and dispersion spectrum for S=1/2 and rhombic symmetry.*

An additional complication arises from molecules being statistically oriented in a sample. This is often the case for metalloproteins if protein single crystals are not available. The orientational average can be obtained by integration over θ and ϕ, i.e. taking into account the signal contribution for each possible orientation of the molecule relative to the laboratory system. This procedure is normally performed numerically and is described in detail in Appendix A. Some typical lineshapes are given in Fig. 2.4. In the upper trace of the figure we have assumed that the metal ion in a Spin 1/2 state is surrounded by ligands which impose an axial symmetry. As a consequence only two g-values, g_z and $g_{\perp}=g_x=g_y$ can be distinguished in the spectrum. The lower trace of Fig. 2.4 demonstrates the effect of three different g-values g_z, g_y, and g_x, as they arise from rhombic symmetry for a S=1/2 system. In both figures the absorption and the dispersion spectrum are given in direct analogy to the isotropic case discussed in Section 2.1.1.

2.2 Magnetic Circular Dichroism

Magnetic Circular Dichroism (MCD) is the difference in absorbance of circularly polarised light induced by an externally applied magnetic field [6, 7, 8]. A related effect is the magnetic optical rotary dispersion (MORD), often known as Faraday rotation, wich stems from different refractive indices for left and right circularly polarised light. MCD and MORD are linked by Kramers-Kronig integral transforms and provide equivalent information about the electronic structure of molecules. MCD spectroscopy is frequently used to resolve complex absorption spectra, it can help to detect certain compounds in complex mixtures and to elucidate the electronic structure of molecules such as metalloproteins.

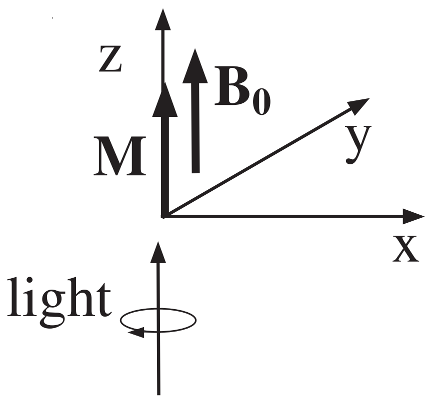

Figure 2.5: *In an MCD experiment the static magnetic field and the incident laser beam are parallel.*

MCD is defined as the differential absorbance ΔA_z of left (LCP) and right circularly polarised light (RCP) in presence of a magnetic field, so that $\Delta A_z = A_{LCP} - A_{RCP}$. B_0 has to be aligned parallel to the incident light beam, as is shown in Fig. 2.5. In standard MCD theory three effects caused by the magnetic field are distinguished. A so-called A-term is a Zeeman splitting of ground and/or excited states. A B-term describes field-induced perturbation and mixing of states. Finally, C-term MCD is a change in the population over the Zeeman-sublevels of a paramagnetic ground level due to Zeeman-splitting in the ground state. At high field and low temperatures C-term MCD dominates the MCD spectrum, and in the following we will focus on this effect.

Fig. 2.6 shows a system with two thermally populated ground and two excited states; the circles represent chromophores in different spin states. The more populated ground state absorbs LCP light, whereas the less populated absorbs RCP light. According to the definition, the MCD from such a system will be positive.

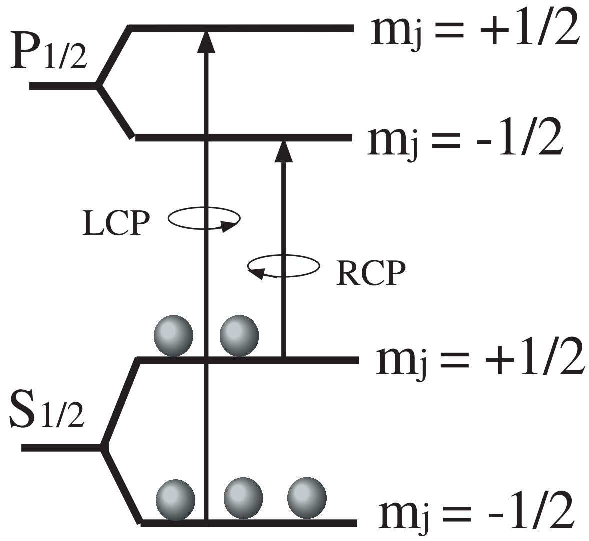

Figure 2.6: *C-term MCD arises from the differential absorption of left and right circularly polarised light due to different population of the Zeeman states.*

The C-term MCD-signal is proportional to the magnetisation in the ground state from where absorption takes place. Thus, in an isotropic system with a spin 1/2 ground state, ΔA_z is proportional to the population difference between both spin states and can be described as a function of field B_0 and temperature T [6, 9]:

$$\Delta A_z \propto \tanh(g\mu_B B_0/2kT), \tag{2.7}$$

where k is the Boltzmann constant. The MCD increases linearly for small B_0/T and the slope of the curve is proportional to g. At very low temperatures however, most molecules will be in the lowest level and a limit will be reached where the MCD-signal shows saturation. Thus, ΔA_z is constant in cases of low temperature and/or high field. One can obtain the g-value of a paramagnetic sample by analysing the slope of the linear part of this MCD detected magnetisation curve.

The situation is more complicated in case of a molecule with g-value anisotropy, since the MCD will have contributions from all three orientational components. However, different g-values can be distinguished in the presence of optical anisotropy. The correlation between the magnetic axes and the optical anisotropy can be described by a matrix whose principal components are the C-parameters C_i, $i = x, y, z$. We assume that the principal

C-value and g-value axes coincide, and obtain for the MCD in the linear limit ($g\mu_B B_0 \ll 2kT$) [6, 9]:

$$\Delta A_z \propto g_z C_z + g_y C_y + g_x C_x. \tag{2.8}$$

The C-parameters contain the optical dipole operators m_j and m_k along the corresponding molecular axes:

$$C_i = \varepsilon_{ijk} Im \sum_E \langle G|\, m_j \,|E\rangle \, \langle E|\, m_k \,|G\rangle \,. \tag{2.9}$$

The sum runs over the exicted states $|E\rangle$, the $|G\rangle$ are the relevant ground states, and ε_{ijk} is the Levi-Civita tensor.

If analysis of the MCD detected magnetisation curve shows that the slope is solely due to g_z, one can conclude that C_x=C_y=0. Thus, only the transition dipoles m_x and m_y are involved in the optical transition, which is as a consequence xy-polarised. This case is found for example in haem-proteins. The experiment is capable to be orientationally selective via the optical transition dipoles, i.e. molecules with certain orientations with respect to the laboratory axes contribute to the signal, while contributions from other molecules are suppressed.

At higher fields the approximation used for the derivation of Eq. 2.8 does not hold any longer. The MCD signal over the full range of field and temperature for a powder-like sample is described with [10, 11, 12]

$$\begin{aligned} \Delta A_z \quad \propto \quad & \int_{\theta=0}^{\pi/2} \int_{\phi=0}^{\pi/2} T(\theta,\phi) \left(\frac{g_x}{g} C_x \sin^2\theta \cos^2\phi \right. \\ & \left. + \frac{g_y}{g} C_y \sin^2\theta \sin^2\phi + \frac{g_z}{g} C_z \cos^2\theta \right) \sin\theta d\theta d\phi, \end{aligned} \tag{2.10}$$

where $T(\theta,\phi) = \tanh(g(\theta,\phi)\mu_B B_0/2kT)$ is the Boltzmann population factor. Eq. 2.10 can be lead back to Eq. 2.8 for the case that $\tanh x = x$. The powder average is here obtained via an integration over θ and ϕ. Several magnetisation curves for a system with three g-values and various polarisations of the optical transitions are depicted in Fig. 2.7. The resolution of the magnetisation curves is of the order of kT and therefore relatively low; only for a relatively large g-value anisotropy it is possible to distinguish the curves.

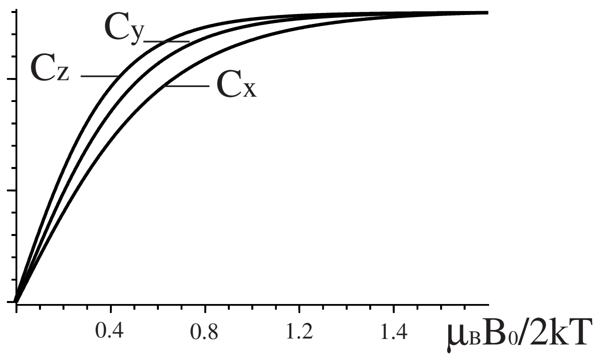

Figure 2.7: *Calculated MCD detected magnetisation curves from a species with g_z=3, g_y=2, g_x=1 for different optical polarisations.*

2.3 Optically Detected EPR

2.3.1 Related Experiments

Various applications combining optical and EPR techniques have been reported in the literature. In most experiments the microwave radiation is used to create a redistribution of population either in the excited or ground state, which effects a change in intensity, polarisation or another feature of emitted or absorbed light [13]. If the population difference between the Zeeman-substates is equalized, i.e. the longitudinal magnetisation is destroyed with an intense microwave pulse, it is possible to monitor the recovery of the magnetisation after the end of the pulse and to determine relaxation rates of the spin system.

To this group belong also experiments where the quenching of the MCD signal due to a saturating microwave field is measured [14, 15]. First applications of this technique have been already reported for a synthetic copper complex and and a metalloprotein [16]. The reduction of the MCD signal will be maximal if the EPR resonance condition is fulfilled. This is especially attractive if two centers with different resonant frequencies are present. By selecting each center via the resonance condition one can investigate its particular contribution to the MCD spectrum. However, this technique is only succesful if saturation of the microwave transition is possible at all. In addition, the quenching effect is ruled by relaxation processes, which can produce a strong coupling between different centers and result in the simultaneous saturation of signals from different species. If the relaxation processes are unfavourable, this effect leads to the partial or complete removal of the desired chemical specificity.

Similar problems can effect the orientational specificity, which in principle should be superior to the relatively poor resolution of the MCD magnetisation curve technique. For an anisotropic center different g-values can be selected via the resonance condition, and the quenching of the MCD can be monitored for each g-value separately. From this effect one can draw conclusions about the polarisation of the corresponding optical transition. Since the relaxation can vary on temperature, frequency, and orientation of the molecule with respect to B_0, the obtained spectra can vary quite drastically in dependence on the experimental conditions. This complicates the analysis and makes a quantitative determination of the polarisation parameters difficult [17].

2.3.2 Optically Detected EPR as Microwave Modulated MCD

The alternative approach we present here is the optical detection of the transverse magnetisation created by a microwave field. This experiment has been proposed for the first time for ruby [18]. The feasibility was demonstrated for Eu:CaF_2 [19] and later for ruby [20].

Like in conventional EPR, in ODEPR spectroscopy the magnetisation is excited by a resonant microwave field. A circularly polarised laser beam perpendicular to the static field probes the magnetisation in the direction of the laser field. The precessing spins modulate the absorptivity of the sample for circularly polarised light and the transmitted laser beam is therefore modulated at the microwave frequency as [21]

$$\begin{aligned} P &= P_0 10^{-(A_0 + \frac{\Delta A_x}{2} \sin \omega_{mw} t)} \\ & \quad \text{and for small modulations (typically } A_x < 10^{-6}) \\ &\simeq P_{d.c.} - P_0 10^{-A_0} \ln(10) \frac{\Delta A_x}{2} \sin \omega_{mw} t, \end{aligned} \tag{2.11}$$

where P_0 and P is the light power before and after the sample, respectively, A_0 is the absorption of the unpolarised sample, and $P_{d.c.}$ a d.c. offset. A_x is the transverse MCD created by the transverse component of the magnetisation. The experimental geometry is depicted in Fig. 2.8. When this modulation is measured as a function of the static magnetic field strength, one obtains optically detected EPR spectra.

If the sample contains two chromophores with different optical and magnetic properties, a suitable choice of the optical wavelength will result in different, distinguishable optically detected EPR spectra. Thus, this method is able to select chemical species in a mixture of different components or to suppress contributions from impurities.

In addition, ODEPR provides orientational selectivity via the different components of the optical anisotropy (C-parameters), which contribute to different parts of the EPR spectrum. Since the optical and magnetic anisotropy are fixed to the same molecular axis system, the spectral position (determined by the g-value) and the amplitude (determined by the C-value) are correlated. Thus, only molecules with certain orientations with respect to the laser beam contribute to the ODEPR spectrum, which as a consequence differs fundamentally from a conventional EPR spectrum.

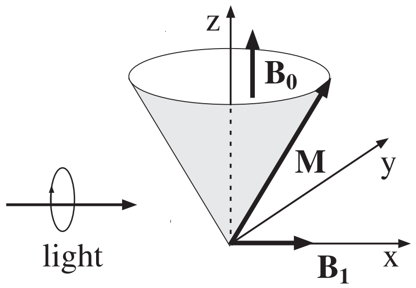

Figure 2.8: *In an ODEPR experiment the incident laser beam is perpendicular to B_0 and detects the transverse, precessing component of the magnetisation.*

To illustrate this effect consider a molecule with axial symmetry, i.e. two g-values g_z and $g_\perp$ and two C-parameters C_z and $C_\perp$. We assume first that C_z is the only nonvanishing component. The main signal contribution arises then from molecules whose symmetry axis lies along the laser beam (see Fig. 2.9b)). For those molecules, the magnetic field is parallel to $g_\perp$ and the microwave excitation of the transverse magnetisation is most efficient when the static magnetic field matches the resonance condition $B_0 = \hbar\omega_{mw}/(g_\perp \mu_B)$, where ω_{mw} is the microwave frequency. For molecules whose molecular z axis lies along the magnetic field, the laser beam propagates in the xy plane, where the MCD sensitivity vanishes, and the signal at the corresponding field position is negligible (Fig. 2.9 a)). For an intermediate orientation the signal amplitude is obtained by projecting the laser beam and the magnetisation onto the molecular z-direction, resulting in a weight factor of $\sin^2\theta$.

If in contrast the optical anisotropy is perpendicular to the z-axis ($C_z = 0$), the strongest signal contributions arise from molecules for which the laser beam propagates perpendicular to the symmetry axis. The total signal contribution from such molecules is proportional to $1 + \cos^2\theta$ if the effect of g-value anisotropy is small.

These weight factors describe the dependence of the signal on the orientation of the molecules relative to the laser beam. To calculate actual spectra, one needs to take into account also the effect of g-value anisotropy on the efficiency of the microwave excitation. A detailed calculation [22, 12] is based on calculating the equation of motion of the ficticious spin from a molecule with S=1/2. It has been shown that for an axially symmetric system the microwave modulated MCD ΔA_x along the direction of laser beam propagation is

$$\Delta A_x \propto \int_{\theta=0}^{\pi/2} T(\theta) f(\theta,\sigma) \left[C_z g_z \frac{g_\perp^2}{g^2} \sin^2\theta + C_\perp g_\perp \left(\frac{g_z^2}{g^2} \cos^2\theta + 1 \right) \right] \sin\theta d\theta, \tag{2.12}$$

where $f(\theta, \sigma)$ is a lineshape function with linewidth σ and $C_\perp = (C_x + C_y)/2$.

Figure 2.9 c) shows the corresponding ODEPR powder spectrum for an axially symmetric g-tensor and $C_\perp = 0$. The orientational average has been obtained by integrating over all possible orientations. This ODEPR spectrum shows a strong decrease in the field region of the g_z-resonance stemming from vanishing signal contribution from molecules whose symmetry axis lies along B_0. In row d) the ODEPR spectrum for $C_z = 0$ is given. Comparison with the conventional absorption EPR spectrum in the bottom row demonstrates the orientational selectivity of the optical method.

In the general case of rhombic symmetry three different g-values and integration over the additional angle ϕ has to be considered. It has been shown [12] that the ODEPR signal in this case is

$$\begin{aligned} \Delta A_x \quad \propto \quad & \int_{\theta=0}^{\pi/2} \int_{\phi=0}^{\pi/2} T(\theta,\phi) f(\theta,\phi,\sigma) \left[C_z g_z \frac{g_\perp^2}{g^2} \sin^2\theta \right. \\ & + C_x \left(\frac{g_x^3 g_z^2}{g^2 g_\perp^2} \cos^2\theta \cos^2\phi + \frac{g_x g_y^2}{g_\perp^2} \sin^2\phi \right) \\ & \left. + C_y \left(\frac{g_y^3 g_z^2}{g^2 g_\perp^2} \cos^2\theta \sin^2\phi + \frac{g_y g_x^2}{g_\perp^2} \cos^2\phi \right) \right] \sin\theta d\theta d\phi. \end{aligned} \tag{2.13}$$

Fig. 2.9 demonstrates that the correlation of magnetic and optical properties gives rise to lineshapes deviating from conventional EPR. Analysing the lineshape allows conclusions about the optical anisotropy even for samples containing non-oriented molecules, thus removing the need for single crystals. This is especially useful for proteins, where single crystals are rarely available. ODEPR spectroscopy can provide information about the electronic structure of the investigated molecules which cannot be obtained with other techniques. In comparison to MCD spectroscopy, the resolution of ODEPR spectroscopy can be up to two orders of magnitude higher, since it is limited only by the EPR linewidth which has to be small compared to the energy difference given by different g-values. ODEPR is clearly superior to the technique of measuring MCD detected magnetisation curves in particular for molecules whose g-value anisotropy is relatively small such as copper and low spin haem proteins.

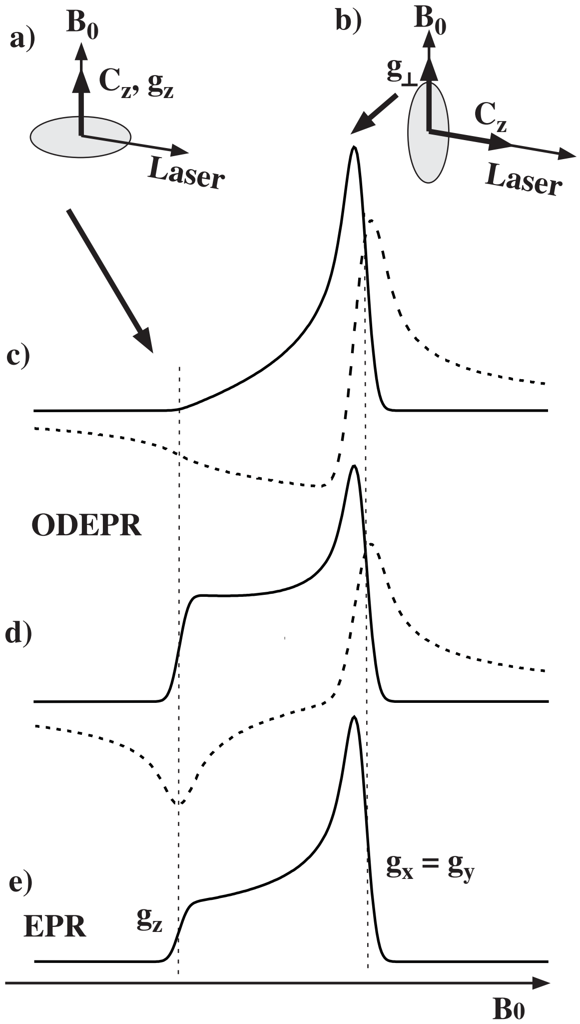

Figure 2.9: *a) Molecules whose z-axis is parallel to the magnetic field do not contribute to the signal if* $C_x = C_y = 0$*. The shaded disk represents the* xy*-plane of the molecule. b) For molecules with* $C_z \parallel$ *to the laser beam, the EPR resonance condition is determined by* $g_\perp$*. c) Calculated ODEPR absorption and dispersion spectra (solid and dashed line, respectively) of an axially symmetric species for* $C_x = C_y = 0$*; note the vanishing signal at* g_z*. d) Calculated ODEPR absorption and dispersion spectra (solid and dashed line, respectively) of an axially symmetric species for* $C_z = 0$*; the signal at* $g_\perp$ *decreases. e) Conventional EPR absorption spectrum.*

2.3.3 Optically Detected EPR as Coherent Raman Scattering

Raman scattering is a nonlinear process in which light is inelastically scattered due to an energy exchange with the sample. The energy of the scattered photons may be lower (Stokes process) or higher (Anti-Stokes process) than of the incident photons. In spontaneous Raman scattering the energy transfer occurs via vibrational transitions of molecules, which mainly increase their energy while simultaneously decreasing the photon energy. Thus, in spontaneous Raman scattering most of the photons are Stokes-shifted.

In contrast, for coherent Raman scattering [23, 24] it is necessary to prepare a coherent material excitation before the Raman process takes place. This is indicated on the left hand side of Fig. 2.10 by the wavy line, which represents a microwave field creating a coherent superposition of the magnetic substates $|1\rangle$ and $|2\rangle$. A laser field couples to an adjacent optical transition $|1\rangle \rightarrow |3\rangle$ and transfers coherence into the second optical transition $|2\rangle \rightarrow |3\rangle$. This coherence leads to an optical polarisation, which is the source of the frequency shifted Raman field.

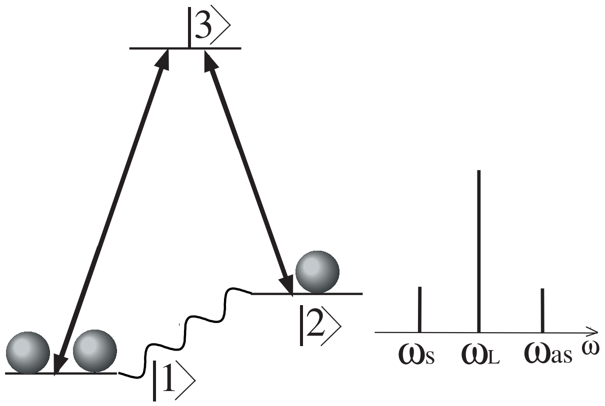

Figure 2.10: *Left hand side: transitions involved in coherent Raman scattering. Right hand side: frequency components of the scattered light.*

If the optical transition is broader than the microwave energy the Raman field contains equal amounts of Stokes- and Anti-Stokes components. The frequency spectrum of the scattered light is depicted on the right hand side of Fig. 2.10. The largest peak is at the laser frequency ω_L. The Stokes-shifted component has a frequency ω_s=ω_L-ω_{mw}, the Anti-Stokes component is shifted to the higher frequency ω_{as}=ω_L+ω_{mw}, where ω_{mw} is the microwave frequency.

The Raman field propagates parallel to the laser field. The fields interfere on a detector and the laser beam acts as a local oscillator for the heterodyne detection of the Raman field. Together they produce a beat signal oscillating at the frequency ω_{mw}. This signal is equivalent to the microwave modulated absorption of the laser beam discussed in the previous section. In fact the interpretation of ODEPR as microwave modulated MCD or as coherent Raman scattering are different, but well compatible concepts, and to some extent it is a question of taste which picture is used. However, the former concept contains some restrictions which are not necessary if one applies the latter picture. The interpretation of the signal as transverse MCD is possible if the optical linewidth is broad compared to the microwave frequency, since the Stokes- and Anti-Stokes component have equal amplitudes and the optically induced electric dipoles adjust instantaneously compared to the oscillation of the magnetisation, thus allowing the concept of a microwave modulated absorption probability to be used.

Indeed the optical bands of most metallproteins are very broad (some hundred wavenumbers). In contrast to metalloproteins the ODEPR experiment has to be described within the coherent Raman picture in cases where the optical absorption resonance lines are narrow, as can be found for example for the ruby R-lines. Also effects like optical pumping and spectral holeburning cannot be described in the transverse MCD-picture. However, although holeburning effects have been reported for some proteins without metal center [25, 26], we have been unable to observe any holeburning effects for the proteins investigated in this thesis. In general the coherent Raman concept provides a more general description of the involved optical and magnetic processes. In this thesis however, we present results demonstrating that the picture of transverse, oscillating MCD is valid for the description and interpretation of the experimental results from several metalloproteins. This allows us to interpret our results in the light of the experimental findings from MCD spectroscopy and in specific cases it enables us to develop further certain theoretical models made for the interpretation of the MCD spectra. The close relation of MCD and ODEPR proves especially useful for the analysis of the ODEPR results from blue copper proteins and Fe-Sulfur proteins, since these species have been already extensively studied with conventional magnetooptical methods. We have successfully applied the theoretical approaches from these studies to our experimental results, allowing us new insights into the electronic structure of these metalloproteins which cannot be gained with other techniques.

Chapter 3

Experimental

3.1 Instrumentation

3.1.1 EPR Spectrometer

For the EPR measurements presented in this thesis a conventional X-band EPR spectrometer was used which operates at approximately 9.6 GHz. This instrument provides a magnetic field up to 1 Tesla by means of an electromagnet. The microwave bridge contains a klystron microwave generator, from where the microwaves are transferred into the cavity by a waveguide.

The coupling between the waveguide and the cavity determines the amount of power stored in the cavity. If the magnetic field is scanned so that the sample absorbs microwave energy, the quality factor of the cavity is lowered due to increased losses. The absorbing sample changes the impedance of the cavity and the coupling so that microwaves will be reflected back to the bridge, resulting in an EPR signal. This signal is usually converted into electrical current by means of a Schottky-diode.

To suppress noise and baseline-instabilites a lock-in detection system is used. To the static magnetic field a small sinusodial field modulation is added, so that the EPR signal is also amplitude modulated at the same frequency. A lock-in amplifier referenced to the modulation frequency produces a d.c. voltage proportional to the first derivative of the original absorption line shape. The spectra presented in this thesis were measured with the commercial Bruker EPR spectrometers at the UEA Norwich and the MPI Mühlheim. A more detailed discussion of these common spectrometers can be found in the literature [3, 27].

3.1.2 Absorption Measurements

The Beer-Lambert Law describes the attenuation of a light beam transversing an absorbant material. The initial power P_0 of the beam is reduced to the power P

$$P = P_0 10^{-c\epsilon l} \tag{3.1}$$

where c is the concentration, ϵ the molar extinction coefficient, and l the thickness of the sample. An absorption spectrometer measures the intensity of the initial and the transmitted light intensity as a function of wavelength. From this the absorbance A is calculated as

$$A = \log \frac{P_0}{P} = c\epsilon l. \tag{3.2}$$

If the extinction coefficient at a certain wavelength is given in the literature, the absorption at this wavelength can serve to determine the concentration of a sample. Absorption spectra shown in this thesis have been recorded on commercial spectrometers at the UEA Norwich, the *MPI für molekulare Physiologie*, and at the spectrometer of the group of Professor Weber from the University of Dortmund.

3.1.3 MCD Spectrometer

The general outline of an MCD-spectromter is shown schematically in Figure 3.1. Frequently a Xe-arc lamp is used as a light source. The light from the lamp is focused into a monochromator. The monochromatized light beam is linearly polarised and modulated with a photoelastic modulator (PEM) at 50 kHz. During one period the PEM converts the polarisation of the linearly polarised light beam first into right circularly and then into left circularly polarised light while keeping the total intensity constant (for the modulation scheme see also Fig. 3.3 in the following section). ΔA_z, the difference between left and right circularly polarised light can now be determined by measuring the power difference ΔP between right and left circularly polarised light as

$$\Delta P = P_{LCP} - P_{RCP} = P_0(10^{-(A+\Delta A_z/2)} - 10^{-(A-\Delta A_z/2)}), \tag{3.3}$$

whereby P_0 is the input power of the beam [8]. Series expansion of the exponential terms and solving for ΔA_z gives

$$\Delta A_z = \frac{-\Delta P}{\ln 10 P}, \tag{3.4}$$

where $P = P_0 10^{-A}$ is the power of the transmitted light. After passing through the sample the beam intensity is measured with a photomultiplier tube or a photodetector. ΔP occurs as a 50 kHz modulation which can be separately detected with a lock-in amplifier (LIA) referenced to the PEM, whereas the unmodulated component P_0 creates a d.c. photocurrent on the detector.

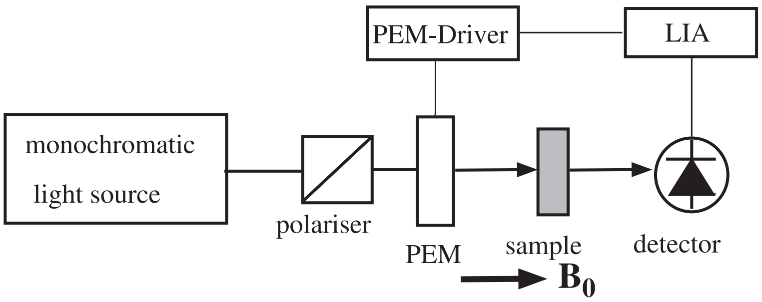

Figure 3.1: *Schematical outline of an MCD-spectrometer. The light beam is monochromatized and then modulated with a PEM. It traverses the sample parallel to the static magnetic field B_0. The differential absortion between left and right circularly polarised light is measured with a photomultiplier or a photodiode.*

The optical cryostat (not shown in Figure 3.1) contains not only the sample probe but also superconducting coils which provide a magnetic field up to 5 T. Two common methods to measure the MCD can be distinguished: (i) the field is kept constant while the wavelength is scanned; (ii) the wavelength is kept constant while the field is increased. The latter technique results in measuring an MCD-detected magnetisation curve. MCD spectra presented in this thesis are measured with a commercial device at the UEA Norwich. More details about instrumentation and operation of MCD spectrometer can be found in the literature [9, 8].

3.1.4 ODEPR: Experimental Apparatus

The setup for the ODEPR experiment is closely related to conventional EPR: microwave radiation is used to create a precession of the magnetisation about the static magnetic field. In addition, one requires a laser beam perpendicular to the static magnetic field which detects the precessing magnetisation. The microwave modulated light beam is detected with an ultrafast photodiode. Figure 3.2 shows schematically the elements of the experimental apparatus.

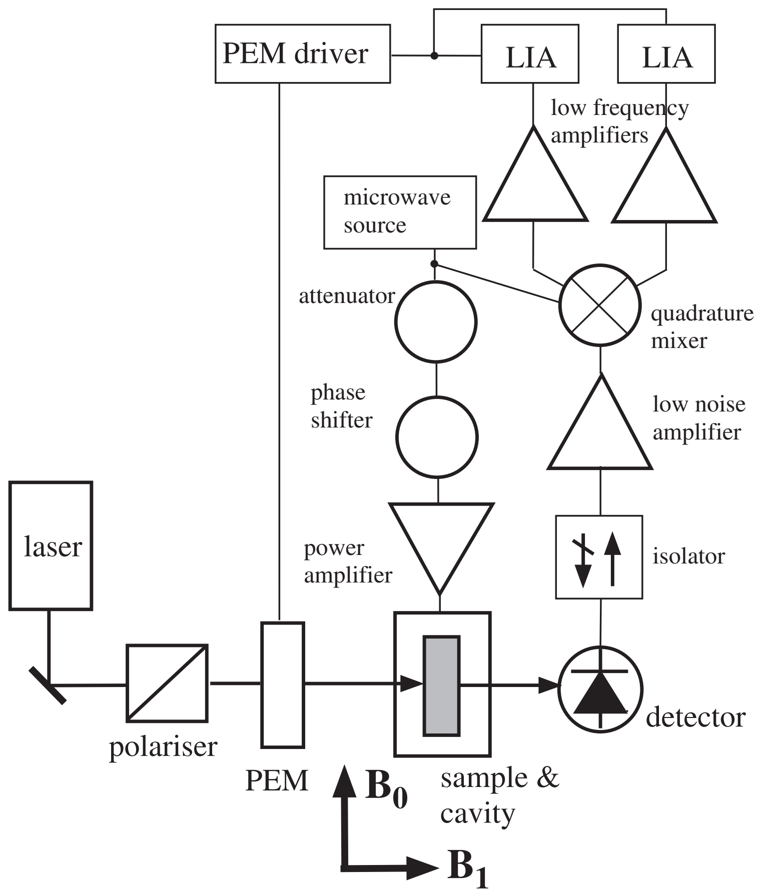

Figure 3.2: *Spectrometer for ODEPR measurements. Microwave radiation creates a microwave field in a cavity containing the sample. A laser beam probes the transverse component of the magnetisation. The modulation of the laser beam creates an a.c. photocurrent on the photodiode; this current is amplified and phase sensitively detected.*

Microwave Excitation We use a solid state oscillator producing continuous wave microwave radiation which can be tuned between 13.4 and 14.1 GHz. The microwave power can be controlled with a variable attenuator (0 - 50 dB). The maximum power after amplification varies between 500 and 1000 mW dependent on the microwave frequency. Via a coaxial cable the microwave radiation is directed into a cavity creating a standing wave. This amplified microwave field leads to excitation of EPR transitions if the resonance condition is fulfilled.

Sample Among several cuvette designs developed during this work a glass cuvette turned out to be most appropriate. This cuvette consists of two glassplates (thickness 0.5 mm, ⊘ 5 mm) which are glued on an C-shape glass ring (outer ⊘ 5 mm, inner ⊘ 3 mm). The protein liquid is inserted at room temperature in the cuvette by a syringe. The sample is held in the cavity by a tube made from a synthetic material with an especially low dielectric constant (Q200.5, Polypenco). In this tube the cuvette is placed. Then the probe rod bearing the cavity at its end is inserted in the sample space of the cryostat, which has been filled with liquid helium. From experience a rapid freezing of the sample gives best optical qualities. If the optical quality of the frozen sample is not sufficient, the procedure can be repeated until better results have been reached.

Sample Space and Magnet The probe with the microwave cavity containing the sample is placed in an optical cryostat (not shown in Figure 3.2). The cryostat also contains a superconducting split-coil magnet, which provides a homogeneous (better than 1 part in 10^4 over the sample volume) magnetic field (0 - 3 Tesla), indicated as B_0. Perpendicular to the static magnetic field the weak microwave field B_1 ($\leq 2 \times 10^{-4}$ Tesla) is applied. Since the sample space is isolated from the liquid helium reservoir of the magnet, it is possible to vary the temperature in the sample compartment between 1.6 - 4.2 K using liquid helium and between 4.2 - 300 K using helium gas. Detailed drawings of a split-coil superconducting magnet can be found elsewhere [9, 28].

Optical Excitation Various laser sources have been used for ODEPR experiments, which are summarized in Table 3.1. The laser beam is linearly polarised by means of a polariser. In order ot suppress drift and low-frequency noise, and to obtain light with a chosen polarisation, the laser beam is modulated with a PEM (see Section 3.1.3) or a mechanical light chopper.

Signal Detection The photodiode has to have a broad electrical bandwidth (21 GHz in our instrument) to be able to follow the oscillation of the microwave modulated laser beam. Since the size of the diode influences its capacitance and therefore its behaviour as a low pass filter, the diode must be small (25 μm diameter). The beam is focused with a lens (focal length 30 mm) onto the diode; exact adjustment of the lens is realised with a precision *xyz* stage.

After amplification the microwave signal is mixed with a part of the microwave radiation from the oscillator. Thus, the signal is demodulated so that

wavelength (range) / nm	laser source
915	diode laser (Man.No. 74.16)
852	diode laser (Man.No. 74.4)
830 - 720	Ti-Sapphire laser
686	diode laser (Man.No. 74.8)
610 - 570	ring dye laser, R110
560 - 555	ring dye laser, R6G
532	frequency doubled Nd:YVO_4
514,501,488,476,458	Ar-Ion-laser

Table 3.1: *Laser sources which were used for different optical wavelengths.*

only modulation with the frequency of the optical modulation remains. The quadrature mixer provides two local oscillator waves which possess a relative phase shift of $\pi/2$. An adequate setting of the phase of the microwave excitation with the phase shifter allows one to measure absorption and dispersion signals seperately. Amplification with two 60 dB low frequency amplifiers finally enables the detection of the signal with two lock-in amplifiers (LIA). The digital signal from the lock-in amplifiers is recorded with a computer. A more detailed discussion of the elements of the microwave bridge can be found elsewhere [29].

From the voltages measured with the lock-in amplifier, it is possible to determine the microwave modulation depths of the light beam. This is possible by considering the amplifications and attenuations of each element of the microwave bridge. In addition, the bridge was calibrated by a beat experiment. For this experiment two parallel, linearly polarised laser beams with known intensities were focused on the photo diode. If the frequencies of these beams have a frequency difference of approximately 14 GHz, they produce a well defined beat signal oscillating at the frequency corresponding to the offset between the beams. This experiment revealed an excellent agreement between calculated and experimental amplification of the bridge. A detailed discussion of the beat experiment can also be found in [29]. The calibration of the microwave bridge enables us to recalculate from the measured lock-in amplifier voltage the amplitude modulation of the laser beam responsible for this voltage, and as a consequence to give all experimental spectra in units of ΔA_x.

Modulation Schemes Different optical modulators allow one to irradiate the sample with differently polarised light. The standard setup of the PEM enables one to measure the difference between the microwave modulated absorption signal from right and left circularly polarised light. This is achieved by adjusting the polarisation of the laser beam by means of the optical polariser at 45° to the main axes of the PEM and setting the PEM modulation to $\pi/4$. Thus, the PEM creates a phase shift along one axis which varies between 0 and $\pm\pi/4$. The resulting modulation of the light is depicted in Fig. 3.3 as a function of time. The modulation frequency is 50 kHz.

Setting the PEM modulation mode to $\pi/2$ means a phase shift of $\pm\pi/2$ along one PEM axis and results in irradiation with linearly polarised light which is alternatively horizontal and vertical. This setting is depicted in Fig. 3.4. This modulation now occurs at 100 kHz, which has to be taken into account by setting the lock-in amplifier detection frequency to the second harmonic. For the detection of Faraday rotation it is necessary to use a second polariser behind the sample.

The use of a mechanical light chopper results in excitation with only one polarisation depending on the polarisation set in front of the chopper. We used this device with linearly polarised light whose plane of polarisation was alternatively horizontally or vertically.

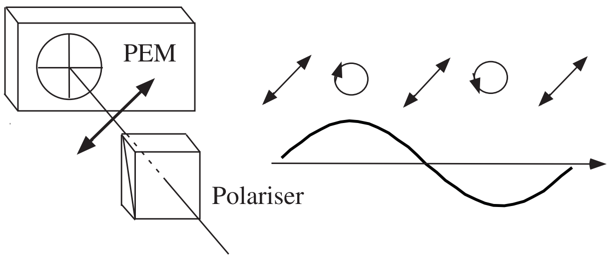

Figure 3.3: *Left hand side: the polarisation of light after the polariser is at 45° to the PEM axes. Right hand side: Setting the PEM to $\pi/4$-mode results in modulation with alternating right and left circularly polarised light.*

3.2 Samples

3.2.1 Azurin

Azurin is a small mononuclear copper protein with a molecular weight of 14.6 kDalton. The sample was a generous gift from the Biochemistry Department of the UEA Norwich. We investigated azurin in the oxidized form, since

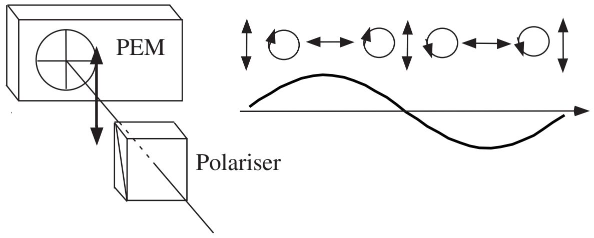

Figure 3.4: *Left hand side: the polarisation of light after the polariser is at 45° to the PEM. Right hand side: Setting the PEM to $\pi/2$-mode results in modulation with alternating horizontally and vertically linearly polarised light.*

the reduced species is EPR silent. The extinction coefficient of the blue absorption band is 3800 M^{-1} cm^{-1} at 631 nm [30] [1].

Wild type azurin from *Pseudomonas aeruginosa* frequently shows impurities from the haem protein cytochrome c. A method to produce azurin without these impurities is the expression of a cloned gene from *Pseudomonas aeruginosa* in another bacterial strain [31]. The azurin which we investigated experimentally was expressed in *Escherichia coli*. This recombinant azurin is spectroscopically identical compared with azurin from *Pseudomonas aeruginosa* [32].

The sample consisted of a buffered aqueous solution of azurin mixed with the glassing agent glycerol (1:1). The buffer was PIPES (Piperazine-N,N'-bis[2-ethanesulfonic acid]; 1,4-Piperazinediethanesulfonic acid) with a pH of 6.7. The concentration used for the EPR and ODEPR experiments was approximately 4.6 mM. The sample used for the MCD experiment was more dilute and had a concentration of 1.6 mM.

3.2.2 Copper Films

Tetraethylammoniumtetrachlorocuprate ($(Et_4N)_2Cu(II)Cl_4$) and tetraethylammoniumtetrabromocuprate ($(Et_4N)_2Cu(II)Br_4$)-films were produced with the method described by Rivoal and Briat [33, 34]: Tetraethylammoniumchlorid (-bromid) and copperchlorid (-bromid) were mixed (2-3:1 by molar weight) and dissolved in acetonitrile. Cellulose diacetate was also dissolved in acetonitrile and mixed with the other solution. A drop of this mixture was allowed to evaporate on a glass surface. The amount of cellulose which was

[1] 1 M = 1 mole per litre

required to produce clear, stable films was determined by trial and error [2]. The films have to be stored in a desiccator to avoid contact with atmospheric humidity. CuCl-films show an intense yellow colour, while the CuBr-films are deep purple/blue.

3.2.3 Rubredoxin

Rubredoxin is a protein containing a sulphur-ligated iron atom. The protein was purchased from “Sigma”. The extinction coefficient at 492 nm is 7 mM^{-1} cm^{-1} [35]. With a molecular weight of approximately 6000 Dalton rubredoxin molecules are relatively small [36]. Oxidized rubredoxin from *Clostridium pasteurianum*, which we investigated in our experiments, was expressed in *Escherichia coli* with the same method as described for azurin. The buffer was TRIS (Trishydroxymethylaminomethane) at a pH of 7.4. The concentration of the EPR sample was 0.5 mM. The concentration of the ODEPR sample was approximately 0.14 mM. For both samples we used glycerol as a glassing agent.

3.2.4 Cytochrome c-551

The low spin haem protein cytochrome c-551 contains a haem-ring with an Fe^{3+}-ion. The Biochemistry Department of the UEA Norwich provided the sample. The extinction coefficient of the closely related protein cytochrome *b*-558 at the Soret peak (414 nm) is 123 mM^{-1} cm^{-1}. [37]. This value has also been used to determine the concentration of the cytochrome c-551 sample, which was found to be approximately 2.9 mM. The glassing agent was ethanediol.

[2] For more details see the notes of the *Präparationslabor* of the University of Dortmund.

Chapter 4

ODEPR as Microwave Modulated MCD

4.1 Wavelength Dependence of the ODEPR Spectra

The Bloch equations relate the transverse and the longitudinal componenents of the magnetisation (Eq. 2.5). For a beam along the laboratory x-axis, the absorption component reaches at resonance a maximum:

$$M_x(\omega_0 = \omega_{mw}) = \omega_0 \frac{B_1}{B_0} T_2 M_0, \tag{4.1}$$

where the index x indicates the laboratory x-axis. The conventional MCD signal A_z is proportional to the static magnetisation along the field direction. In an ODEPR experiment the laser beam is modulated by the transverse component of the magnetisation. We therefore assume that the transverse MCD along the laser beam direction is proportional to the transverse component of the magnetisation M_x and that the proportionality factor between longitudinal and transverse MCD is the same as for longitudinal and transverse magnetisation. Thus, for resonant microwave excitation the transverse MCD is:

$$\Delta A_x = \omega_0 \frac{B_1}{B_0} T_2 \Delta A_z. \tag{4.2}$$

The amplitude of the light beam modulated at the microwave frequency ω_{mw} is (Eq. 2.11)

$$P(\omega_{mw}) = P_0 10^{-A_0} \ln 10 \frac{\Delta A_x}{2} \sin \omega_{mw} t \tag{4.3}$$

$$= \quad P_0 10^{-A_0} \ln 10 \frac{\omega_0 B_1}{2B_0} T_2 \Delta A_z \sin \omega_{mw} t. \qquad (4.4)$$

Thus, the ODEPR signal is directly proportional to A_z. In particular, the wavelength dependence of the ODEPR signal will reflect that of the longitudinal MCD. We could demonstrate this for the first time for ruby single crystals and the metalloprotein cytochrome *c*-551 [21, 38]. This protein contains a low-spin ferric haem with a spin S=1/2 ground level. Due to the large g-anisotropy ($g_z = 3.2, g_y = 2.05$, and $g_x \simeq 1$ [39]) the EPR spectrum of a frozen solution is strongly broadened.

We measured several ODEPR spectra from cytochrome *c*-551 between 586 and 610 nm at a temperature of 2.2 K. A dispersion type ODEPR spectrum measured at $\lambda = 587.5$ nm is depicted in Fig. 4.1(a). The spectrum is presented in units of ΔA_x which was obtained from Eq. 4.4, using an accurate calibration of the instrument (see [29] and Ch. 3.1). The lineshape of the ODEPR signal differs from that of the conventional EPR spectrum because molecules for which the g-value z-axis (normal to the haem plane) is oriented parallel to the magnetic field do not contribute to the signal [40]. This effect is due to the polarisation of the optical transition. It is well established that the electric dipole transitions of the molecule lie along the molecular x- and y-axis. Thus, an ODEPR signal only occurs if the xy-plane is perpendicular to the laser beam and parallel to the magnetic field; for the z-axis being parallel to B_0 the transverse MCD signal vanishes. In the following discussion we approximate the EPR lineshape by a Lorentzian. This allows us to introduce a "resonant field" B_r, as indicated in Fig. 4.1(a).

Although the absorption component of the EPR signal is strongly saturated at the given experimental conditions, the dispersion signal is unaffected. Measurements at different temperatures show similar lineshapes, while the amplitude is inversely proportional to the sample temperature. We may therefore use the peak-to-peak amplitudes as a measure of the transverse MCD ΔA_x. Its dependence on the optical wavelength is indicated by square symbols in Fig. 4.1(b). The longitudinal MCD of cytochrome c-551 was first measured by Foote et al. [41] and is reproduced in Fig. 4.1(c). The spectrum is given in units of the extinction coefficient $\Delta\varepsilon_z$, which is proportional to the differential absorption via the equation $\Delta A_z = \Delta\varepsilon_z cl$ (c: concentration, l: optical pathlength). We compare the wavelength dependence of the transverse MCD with that of the longitudinal MCD which is scaled by a factor of 1.1×10^{-4} and is represented by the full line in Fig. 4.1(b). The comparison shows that the ODEPR spectra mirror the MCD wavelength characteristics, which is especially emphasized by the change of sign around 572 nm.

We now estimate the ratio between MCD and transverse ODEPR signal as discussed above. The width of the optical transition is large enough to

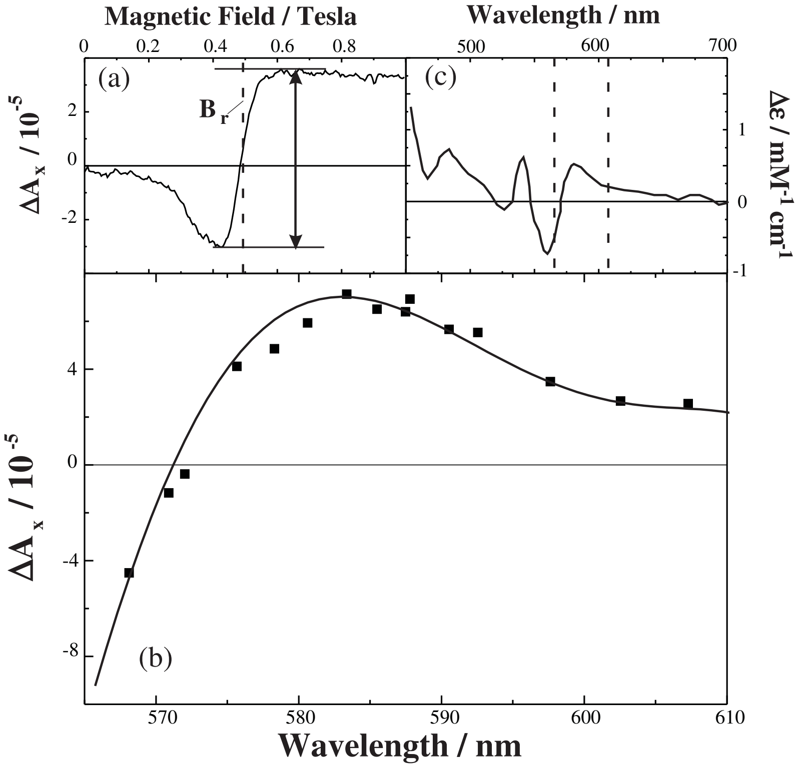

Figure 4.1: *(a) ODEPR spectrum of cytochrome c-551, λ=587.5 nm, temperature 2.2 K, microwave frequency 13.66 GHz. (b) Amplitude of ODEPR spectra as a function of wavelength (squares); scaled longitudinal MCD (solid line). (c) Longitudinal MCD of cytochrome c-551 at B_0=4.9 Tesla and a temperature of 4.2 K [41]; the wavelength range of (b) is indicated with vertical lines.*

satisfy the requirement that the linewidth of the optical excitation be much bigger than the microwave frequency. Since the experimental conditions were different for the measurements of MCD and transverse ODEPR, we first calculate the scaling factor between the parameters used for the MCD (magnetic field $B = 4.9$ Tesla, temperature $\vartheta = 4.2$ K) and those for the ODEPR measurement (magnetic field $B' = B_r$, temperature $\vartheta' = 2.2$ K). According to [9], the two values are related by

$$\Delta A_z(B,\vartheta) = \Delta A_z(B',\vartheta') \frac{\tanh \frac{g\mu_B B}{k\vartheta}}{\tanh \frac{g\mu_B B'}{k\vartheta'}} \tag{4.5}$$

for a spin S=1/2 system.

Inserting ΔA_z in Eq. (4.2) yields the transverse MCD ΔA_x. From the observed linewidth of the ODEPR spectrum we find $T_2 \simeq 2.7 \times 10^{-10}$ s; the factor $\omega_0/2\pi\frac{B_1}{B_0}$ was estimated as 1.55 MHz. The scaling factor thus becomes 5.5×10^{-5}, which agrees with the experimentally determined scaling factor within a factor of $\simeq 2$, which is rather gratifying given the uncertainties in the determination of several experimental parameters.

4.2 Alternative Modulation Schemes

We have indicated in Chapter 2 that different experimental setups can be used in order to irradiate the sample with differently polarised light. We discussed already the case of irradiation with alternating left and right circularly polarised light. Now we shall discuss the experimental findings if linearly polarised light is used.

4.2.1 Faraday Rotation

Faraday rotation results from different refractive indices of left and right circularly polarised light. Linearly polarised light with a given plane of polarisation can be represented as a superposition of left and right circularly polarised waves. Different refractive indices of these two components will lead to a rotation of the plane of the polarisation of linearly polarised light. In case of transverse Faraday Rotation, this rotation will oscillate at the microwave frequency. However, since it does not lead to an amplitude modulation, it will not result in a measurable signal (see left hand side of Fig. 4.2). This cancellation can be avoided by placing a polariser behind the sample. One obtains amplitude modulation from a projection of the tilted polarisation vector of the light onto the axis of the polariser, as is indicated on the right hand side of Fig. 4.2.

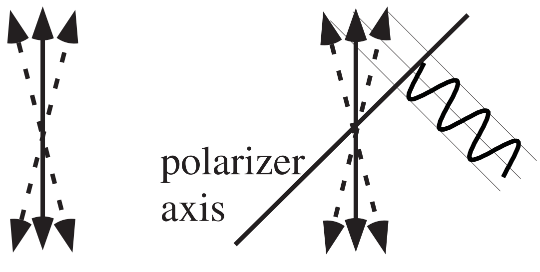

Figure 4.2: *Left hand side: a transverse, microwave modulated Faraday effect leads only to a modulation of the plane of polarisation. Right hand side: placing a polariser behind the sample results in an amplitude modulation due to the Faraday effect.*

In a first experiment for the detection of transverse, microwave modulated

Faraday rotation we investigated the dominant optical transition of azurin at 685 nm (Cu $d_{xy} \rightarrow$ Cys-Sπ). No Faraday signal could be observed. This is not too surprising since the MCD is close to an extremum at this wavelength (see Fig. 5.8). Since Faraday rotation is the related dispersive effect, the dispersion at this point should be rather small [1]. We therefore tried $(Et_4N)_2CuBr_4$-films as an alternative sample. At 501 nm the MCD, which is depicted in Fig. 4.3, has a very strong slope, indicating a region with strong dispersive effects. Indeed a Faraday rotation signal was easily observed, and is depicted in Fig. 4.4 as a dashed line. For comparison, we measured the transverse MCD signal at 514 nm, where the MCD has a maximum. As expected, the signal from MCD and Faraday rotation look similar (compare to the solid line in the same Figure). To allow comparison between both spectra, we have scaled the Faraday rotation signal by factor of 10.

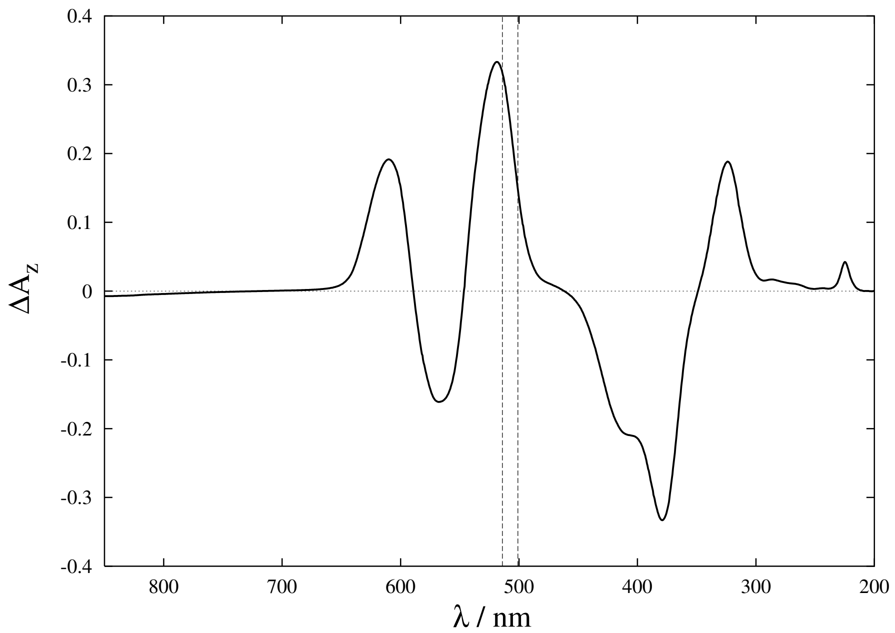

Figure 4.3: *MCD spectrum in the visible of a prototypical ($(Et_4N)_2Cu(II)Br_4$)-film. 501 nm and 514 nm are indicated by vertical lines. The temperature was 1.6 K with a with field of 5 Tesla.*

[1] A technical problem is the installation of the additional polariser. Since this optical element slightly moves the beam alignment, the focus on the diode can get lost. If the Faraday rotation signal has approximately the same size as the noise, it might not be possible to refocus the signal, even if this was clearly visible for transverse MCD before.

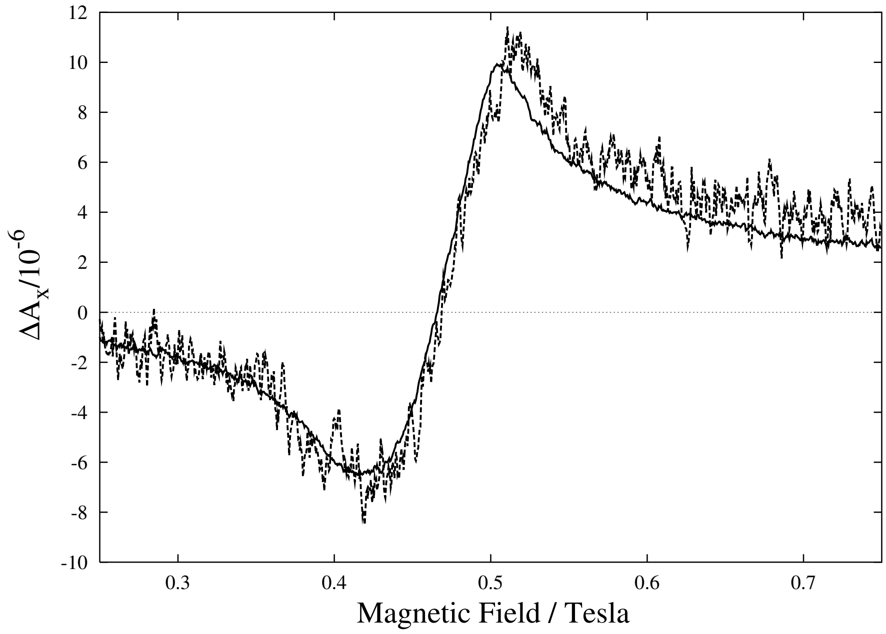

Figure 4.4: *ODEPR signal from transverse, microwave modulated Faraday rotation (dashed line) at $(Et_4N)_2CuBr_4$-films, 501 nm. For comparison an ODEPR signal from transverse, microwave modulated MCD at $(Et_4N)_2CuBr_4$-films, 514 nm is also given. For convenience we have scaled the MORD signal by a factor of 10 to the same size as the MCD signal. The temperature was 1.8 K with a microwave power of 100 mW.*

4.2.2 Other Modulation Schemes Involving Linearly Polarised Light

The results of some other modulation schemes were also investigated for azurin (Cu $d_{xy}\rightarrow$ Cys-Sπ transition at 686 nm) and $(Et_4N)_2CuBr_4$-films (501 nm). The difference between horizontally and vertically polarised light was studied. This approach serves to detect contributions from linear magnetic dichroism, i.e. the different absorption of light with parallel and perpendicular polarisation with respect to an applied magnetic field [42]. No signal could be detected at a wavelength of 514 nm. We also used a chopper in combination with vertically or horizontally linearly polarised light. These experiments also did not lead to any measurable results. The spectra measured from transverse, microwave modulated MCD possess a signal-to-noise ratio of approximately 100 at 514 nm for $(Et_4N)_2CuBr_4$-films. Thus, we conclude that signals based on linear dichroism are at least by two orders of magnitude smaller than the spectra based on circular dichroism. This has been confirmed by experiments with ruby [43].

4.3 Holeburning Experiments

Spectral holeburning can take place when optical pumping proceeds in solid materials, where the optical resonance line experiences strong inhomogenous broadening. Fig. 4.5 illustrates the principle of optical pumping: The intense resonant laser field depletes state $|1\rangle$ and increases the population in state $|2\rangle$. The absorption of the laser resonant with the optical transition $|1\rangle \rightarrow |3\rangle$ therefore decreases. The resulting reduced absorption of the laser is referred to as a "hole" if it occurs in an inhomogenously broadened optical absorption line.

Spectral holeburning on proteins was so far reported for proteins without metal centers which are mostly involved in photosynthesis [25, 26]. In these experiments the chromophores are excited and transferred to some photoproduct state with different spectral properties. Hole burning times based on this photobleaching process have been reported to be in the order of minutes. The objective of the work presented here was to investigate the occurence of spectral holeburning in the metalloproteins which have been the subject of this thesis.

We focused on the Cu $d_{xy}\rightarrow$ Cys-Sπ transition at 686 nm of azurin. First we measured the transmitted laser power of the sample as a function of incident laser power. In presence of holeburning the transmitted power is expected to increase superlinearly with increasing input power. The result is presented in Fig. 4.6. The very linear behaviour shows that the existence of holeburning is unlikely. The absorption (right hand axis) is constant as a function of input laser power. The second step was a time-resolved holeburning experiment. This was realized with a mechanical chopper and allows one to observe changes in the absorption on a millisecond time scale. No time-dependent changes of the absorption were observed. Blocking the light beam and removing the beam block after several seconds or minutes also did not result in any modification of the absorption.

4.4 Discussion

The proportionality of the amplitude of the ODEPR spectra and the longitudinal MCD shows that ODEPR can not only be described as coherent Raman scattering, but also as transverse, microwave modulated MCD. This is an important result since it allows an estimate of the expected signal size and an optimization of the experimental parameters, particularly the optical wavelength. Indeed we have observed the described behaviour for all investigated samples in this thesis. In addition, also for azurin and rubredoxin we have found reasonable scaling factors between transverse and longitudinal MCD in analogy to transverse and longitudinal magnetisation. Our results have shown that the model of a microwave modulated MCD is suitable to describe the experimental findings.

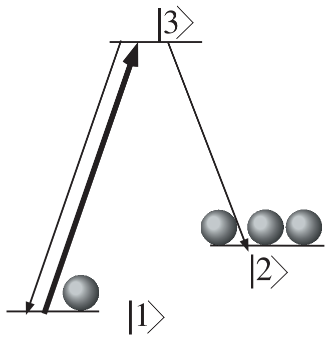

Figure 4.5: *Mechanism of optical pumping: a laser field (thick arrow) depletes state $|1\rangle$, so that the population of state $|2\rangle$ is enhanced.*

The detection of microwave modulated Faraday rotation is an additional confirmation for our theoretical model. The similarity of the ODEPR signals demonstrates that similar information about the electronic structure can be extracted from MCD- and Faraday-created ODEPR signals. In contrast to MCD transverse Faraday rotation can be obtained at wavelengths where the optical absorption of the sample is low. This allows one to increase the incident laser power and yields a larger ODEPR signal. However, the Faraday rotation effect has the disadvantage to reduce the local oscillator power due to the second polariser behind the sample. In addition, due to the strong overlap of broad optical dispersion lines a deconvolution of the optical spectrum in separate transitions and an assignment of the bands is more complicated than for MCD. Clearly, the real significance of this effect has not been investigated in detail yet, instead only a few experiments have been presented here to demonstrate the feasibility of the method.

No ODEPR signal from linearly polarised light excluding Faraday rotation could be detected from two prototypical samples. This indicates that such signals are too small to be found on metalloproteins. One has to conclude that metalloproteins are not appropriate samples for the investigation of these "exotic" effects, since the signal-to-noise ratio is already rather poor for circular dichroism. Single crystals like ruby are clearly more adequate samples for studies on ODEPR signals from linearly polarised light.

No holeburning and optical pumping effects could be found at the strongest optical transition of azurin. Optical holeburning might be prevented due to very fast relaxation between the groundstate sublevels. As a confirmation of this result, we suggest to apply a pump-probe experiment where the probe beam is frequency scanned in presence of a strong pump laser. If optical pumping cannot be achieved, it is uncertain if the population difference between the groundstate sublevels, which is normally given by Boltzmann's law, can be increased.

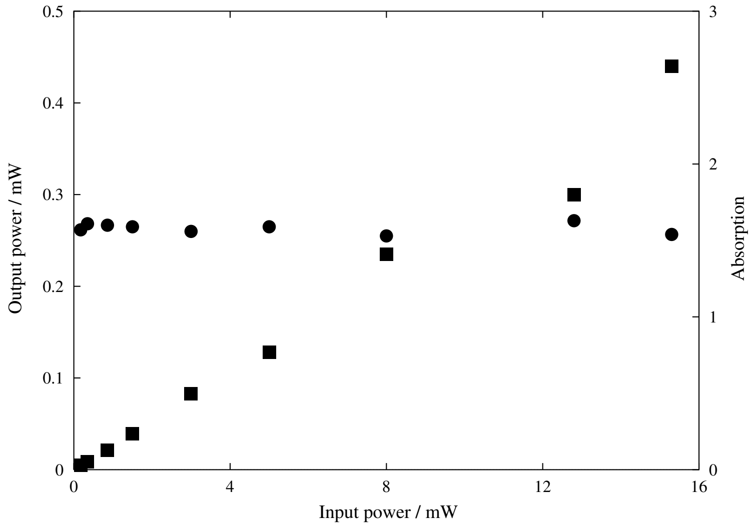

Figure 4.6: *Transmitted versus incident laser power (squares, left hand axis) for azurin, 686 nm. Absorption versus incident laser power (circles, right hand axis).*

Chapter 5

Copper Proteins and Model Complexes

5.1 Azurin

Azurin belongs to the group of blue copper proteins. The development of a detailed understanding of the unique spectroscopic features of the blue copper site has been a major goal of many experimental and theoretical studies. The blue copper site possesses characteristic properties such as an intense blue colour stemming from a strong absorption band at approximately 600 nm and an unusually small hyperfine coupling.

Azurins are found in the respiratory chains of various denitrifying bacteria, where their role is to transport electrons between cytochrome c-551 and cytochrome oxidases [44]. The protein structure of *Pseudomonas aeruginosa* azurin is depicted in Fig. 5.1 [1]. The protein chain is represented by grey ribbons partially arranged in a β-sheet configuration forming a so-called β-barrel structure around the protein's active site. On the right hand side the amino acid chain forms a short α-helix. The ligating amino acids of the copper protein are two histidines, a cysteine, a methionine and a distant glycine. The details of the active site are depicted in Fig. 5.2. Single crystal EPR studies revealed the approximately axial symmetry of the ground-state g-tensor, where the g_z-axis is almost parallel to the bond from the copper to the sulfur of the methionine ligand [46]. This is also indicated in the Figure.

A blue copper protein found in higher plants and algae is plastocyanin, which is involved in photosynthetic processes [44]. The structure of the active site of plastocyanin is very similar to azurin, and also the spectroscopic

[1] The corresponding pdb-file is 1AZU. The figure was produced using the program Molscript by Per J. Kraulis [45].

Figure 5.1: *Chain structure of Pseudomonas aeruginosa azurin.*

features are closely related. Many spectroscopic studies [47, 48] have been done on plastocyanin, and during the analysis of the experiments on azurin we will frequently refer to the results from plastocyanin.

5.1.1 Electron Paramagnetic Resonance

The conventional EPR spectrum of azurin measured at 9.6 GHz is shown in Fig. 5.3 (dashed line). Also the two g-values g_z and $g_\perp$ are indicated by arrows.

To fit the experimental ODEPR spectra, we first extracted the spectral parameters such as g-values, hyperfine coupling constants, and linewidth from the conventional EPR spectrum. The EPR spectrum shows some anomalies in the splitting and broadening of the hyperfine peaks in this

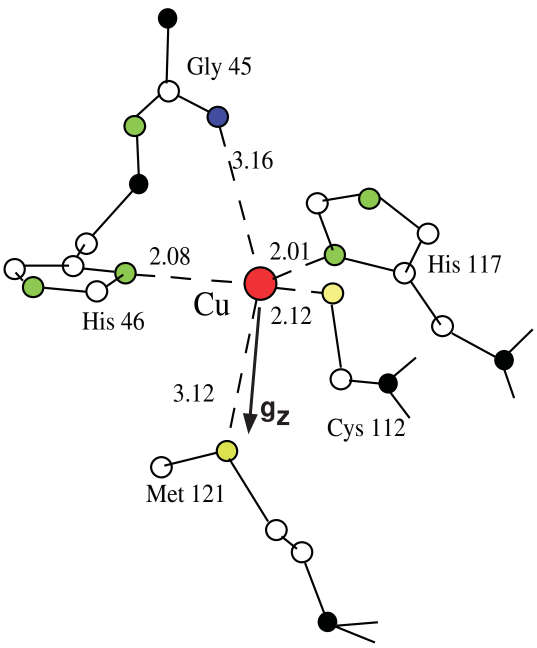

Figure 5.2: *Active site of Ps. aeruginosa* azurin. *green: N. yellow: S. blue: O. white, black: C. red: Cu. Also given is the g_z-axis of the g-tensor.*

region. Aqualino et al. [49] suggested a correlated distribution of g_z and A_z values to take into account these anomalies. Such a correlation models the features in the low-field region very well, especially for Q-band spectra, where the hyperfine-quartet is collapsed into a single, broad peak. However, the modifications made to a dispersion spectrum measured at 9.6 GHz are rather small since the dispersion line itself broadens and obscures the hyperfine peaks. The g-A-correlation therefore seems not to make an essential contribution for the simulation of the ODEPR spectra where only dispersion lines are investigated.

Another feature becoming visible at Q-band and W-band is the rhombic character of the cupric site, where the difference between $g_y = 2.0568$ and $g_x = 2.0393$ [46] is very small. However, we found that a simple axial model yields already good agreement between theoretical and experimental data without taking the rhombic distortion into account. The hyperfine coupling to the copper nucleus (single isotope, I=3/2) was taken into account to first order. The best fit was obtained with the following parameters: $g_z = 2.26$, $g_\perp$ =2.045, A_z=172 MHz, $A_\perp = 27$ MHz, and a homogeneous lineshape $f(\sigma, \theta)$ equal to a Gaussian with a linewidth $\sigma = 55$ MHz. These parameters are in agreement with values found in the literature [49, 50]. The experimental spectrum and the fit curve are shown in Fig. 5.3. The quality of the fit is very convincing although the used model is rather simple.

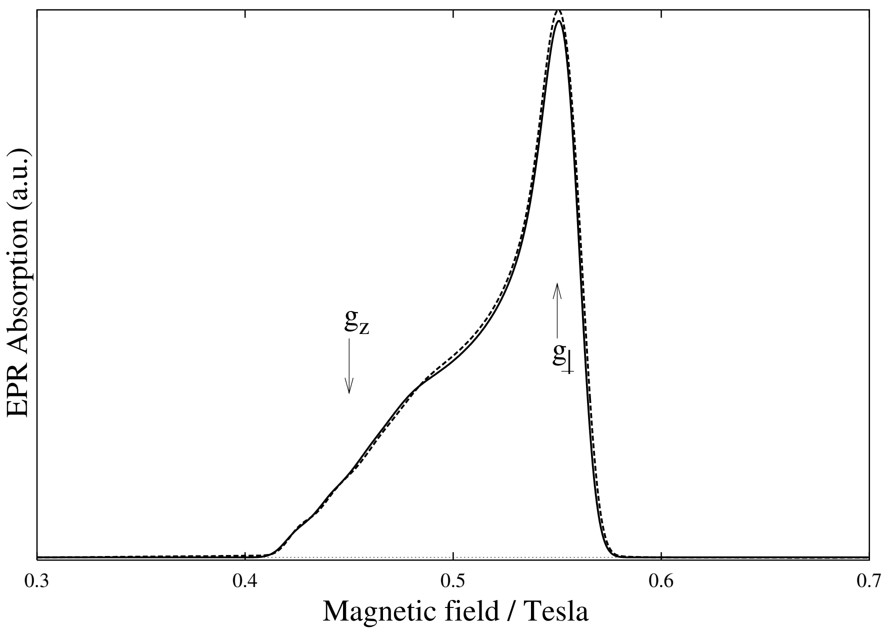

Figure 5.3: *Azurin EPR spectrum at 9.6 GHz, 20 K, 2 mW microwave power (dashed line) and simulated spectrum (solid line) with the parameters as given in the text.*

We also investigated the saturation of the azurin resonance spectrum at high microwave powers. At low temperatures and high microwave fields the EPR absorption spectrum can be easily saturated. Two typical spectra are depicted in Fig. 5.4. Both spectra are measured at 2 K, the unsaturated one with a microwave power of 0.2 mW (solid line), while the spectrum measured at 200 mW (dashed line) is anisotropically saturated especially at the g_z-resonance. However, we found that the dispersion spectrum is not so strongly affected by the saturation so that the basic lineshape remains undistorted. This will be demonstrated in Section 5.1.2.

5.1.2 Optically Detected EPR

ODEPR spectra were measured at different wavelengths in the range from 450 to 850 nm, where we expect ligand-field as well as charge transfer transitions. We used a number of different laser sources to cover this range (see Table 3.1). Figure 5.5 b) - d) summarizes some typical lineshapes. Only the dispersion signal is shown, since the absorption signal is strongly saturated under our experimental conditions. The ODEPR spectra were measured at 1.8 K with

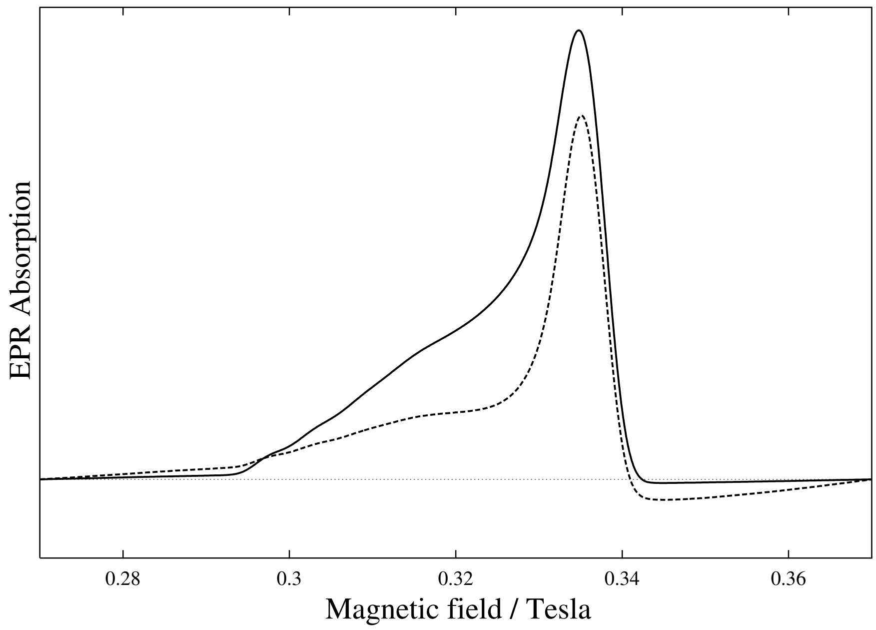

Figure 5.4: *Two conventional EPR absorption spectra (2 K, 9.6 GHz) at different microwave powers. Solid line: 0.2 mW. Dashed line: 200 mW. The gain is adjusted so that without saturation the spectra would have the same amplitude.*

a microwave power of 100 mW and are plotted as $\Delta\varepsilon_x$, the difference in extinction coefficients for left and right circularly polarised light along the direction of the laser beam. Lineshapes at all wavelengths differ from the conventional EPR spectrum, which is given in Fig. 5.5 a). The experimental spectra are compared to theoretical spectra, where the ratio of $C_\perp$ to C_z was adjusted to produce the best fit to the experimental data.

The parameters obtained from fitting the conventional EPR spectra were used as a starting point for fitting the optically detected EPR spectra according to Eq. 2.12, Section 2.3. An adequate simulation of most spectra at 1.8 K was possible with $\sigma = 125$ MHz. The results are shown as solid lines in Figure 5.5. The spectrum at 720 nm (13899 cm^{-1}) with a ratio $C_\perp/C_z$=0.12 is a typical example for predominantly C_z-MCD, while the spectrum at 514 nm (19455 cm^{-1}) shows predominantly $C_\perp$-MCD ($C_\perp/C_z$ = -4). Finally the spectrum at 810 nm (12346 cm^{-1}) with $C_\perp/C_z$ = -0.45 is an example of a region with mixed polarisations.

The larger homogeneous linewidth of the ODPER spectra compared to the conventional EPR spectra (125 MHz vs. 55 MHz) may be an indication of partial saturation at 1.8 K. Temperature dependent studies show that

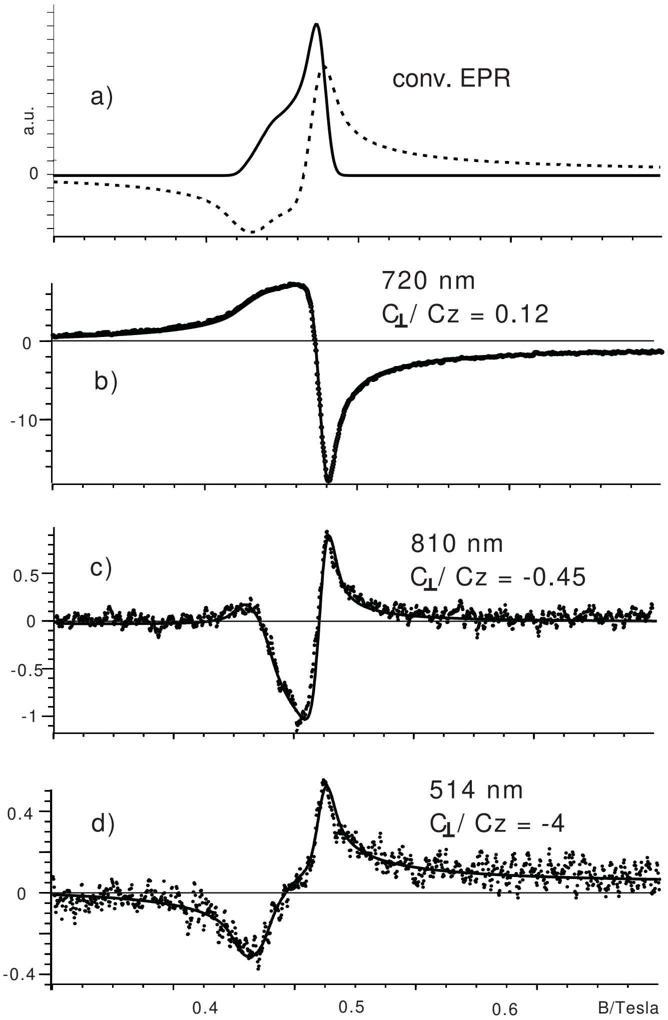

Figure 5.5: *Three ODEPR dispersion spectra measured at at 720, 810, and 514 nm in units of* $\Delta\varepsilon_x \times 10^{-3}$ *(dots). The fits were calculated according to Eq. 2.12. For comparison in a) the conventional EPR spectrum is given.*

around 45 K, where relaxation is faster, the linewidth of the ODEPR spectra decreases to values obtained from conventional EPR. The ratio of $C_\perp/C_z$ is hardly affected by this behaviour. This is demonstrated in Figure 5.6, where two ODEPR dispersion spectra are given measured at different temperatures. For convenience we have scaled the high temperature spectrum to the same amplitude as the low temperature spectrum. Where at 1.8 K the ratio $C_\perp/C_z$ is 0.08 $\pm$ 0.04, we find at 45 K $C_\perp/C_z$ = 0.15 $\pm$ 0.05. The difference can be explained from anisotropic saturation in the g_z region as was already observed for the conventional EPR absorption lines (Fig. 5.4). However, the deviation for both temperatures is rather small. Light power dependent studies and microwave power dependent studies also show that the influence of the saturation on the dispersion is weak. Thus, information about optical anisotropies can be extracted even if saturation effects occur.

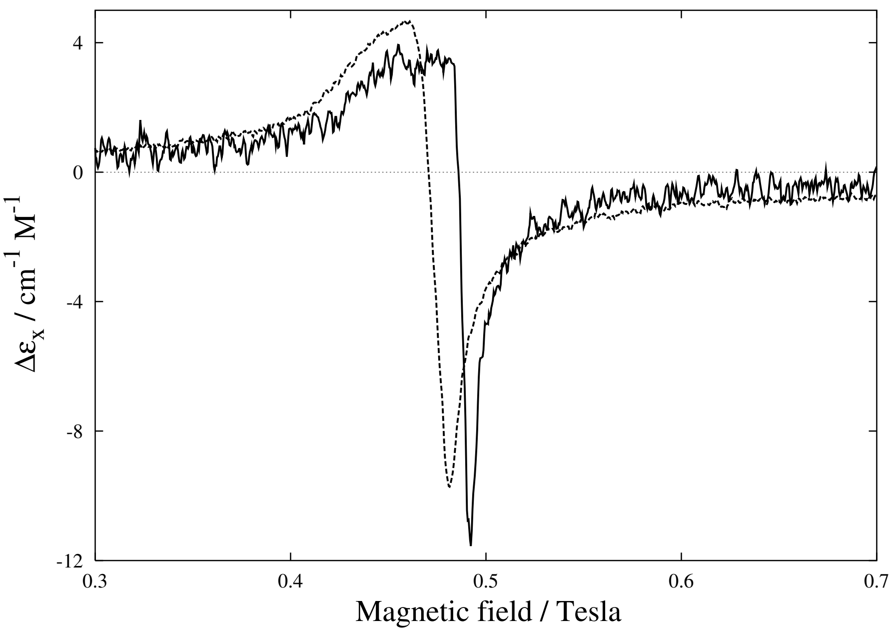

Figure 5.6: *Two ODEPR dispersion spectra measured at at 739 nm in units of $\Delta\varepsilon_x \times 10^{-3}$, a microwave power of approximately 100 mW and different temperatures. Solid line: 45 K, 14.05 GHz. Dashed line: 1.8 K, 13.67 GHz.*

The relevant quantity for our analysis is the ratio of the two C-parameters, which may conveniently be expressed as an orientation angle: $C_z = C \cos\gamma$ and $C_\perp = C \sin\gamma$. Since the absolute value of $C_\perp$ and C_z cannot be extracted from the spectra, we have for convenience introduced a factor k which scales C in such a way that comparison with the longitudinal MCD bands is possible.

Figure 5.7 shows the variation of these parameters with the detection wavelength. The filled squares represent γ and the open squares kC. The inset defines γ. In the intermediate energy region between 13500 and 18000 cm^{-1} the angle is close to π, indicating a dominating contribution of negative C_z-MCD. At 12700 cm^{-1} γ approaches 2π, indicating that positive C_z dominates over smaller contributions of negative $C_\perp$-MCD. Around 19200 cm^{-1} γ is close to $\pi/2$, indicating positive $C_\perp$-MCD.

In regions of high optical absorption (compare Fig. 5.8, inset), absorption of the detection laser raised the sample temperature. This resulted in

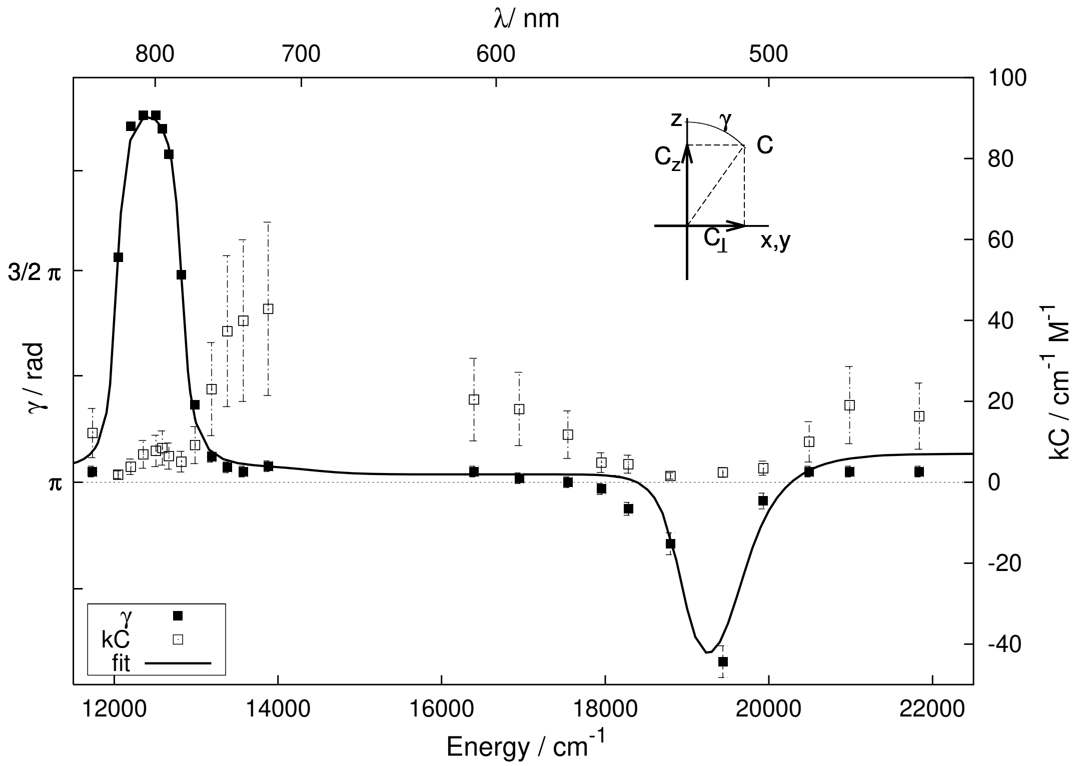

Figure 5.7: *Fitting the ODEPR spectra gives the different C-parameters for each wavelength. The data are presented as* $kC = k\sqrt{C_z^2 + C_\perp^2}$ *(open squares) and* γ=arctan $\frac{C_\perp}{C_z}$ *(filled squares). The fit curve for* γ *(solid line) was obtained with the parameters given in Table 5.1.*

a slightly smaller linewidth (≈110 MHz) and a decrease of the signal size resulting from the smaller Boltzmann factor. The results obtained for the orientation angle γ are not affected by these variations, in contrast to the amplitude kC. Sample heating did not occur in the longitudinal MCD, which was recorded with a conventional light source at much lower intensity. As a result, the two spectra are not proportional in this wavelength range, in contrast to the usual behaviour [21]. The ODEPR measurements near 19000 cm^{-1} were obtained from a different sample than the other spectra. Differences in the optical quality of this sample led to deviations in the apparent magnitude parameter kC, but did not affect the orientational parameter γ.

5.1.3 Relation to MCD and Band Structure

In addition to the wavelength dependence of the ODEPR spectra, we also measured the conventional MCD spectrum, which is reproduced in Fig. 5.8

as a dotted line. $\Delta\varepsilon_z$ is the MCD given in units of the difference in extinction coefficients for left and right circularly polarised light. In the linear limit, the MCD depends on the g-values and C-parameters as reproduced in Eq. 2.8, which we give here for an axial system:

$$\Delta\varepsilon_z \propto g_z C_z + 2g_\perp C_\perp. \tag{5.1}$$

This equation describes the relation between total MCD and C-terms adequately, although, according to the experimental conditions (1.8 K, 5 T), we are in the strict sense not anymore in the linear limit. In contrast to ODEPR, it is clearly impossible to determine both C-parameters from a single MCD spectrum.

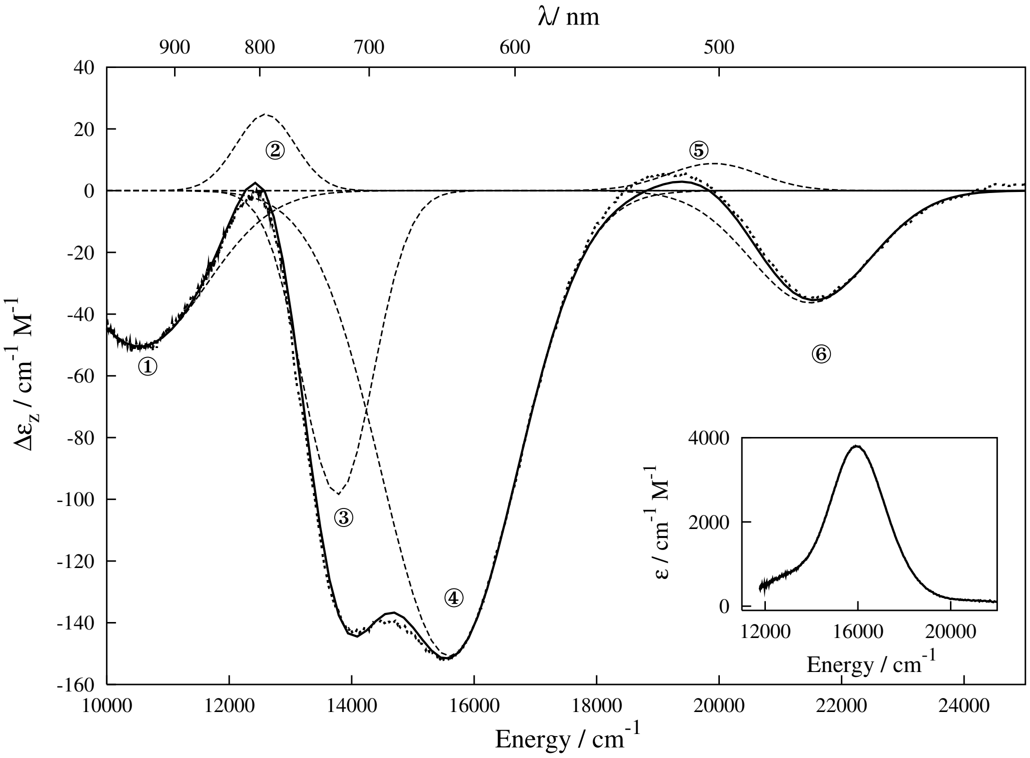

Figure 5.8: *MCD spectrum of azurin at 1.8 K, 5 Tesla. Six bands are used to fit the features of the MCD curve in the visible region. An inset shows the absorption of azurin.*

The next step in the data analysis was the decomposition into individual transitions with individual energy, linewidth, and optical anisotropy. The longitudinal MCD data were calculated as

$$\Delta\varepsilon_z(\nu) = \sum_i \Delta\varepsilon_{zi} e^{-\frac{(\nu-p_i)^2}{2w_i^2}} \tag{5.2}$$

with ν indicating the photon energy, p_i and w_i the position and width of each band. $\Delta\varepsilon_{zi}$ is the MCD amplitude for each band.

In the case of the transverse, microwave modulated MCD (ODEPR), the precision of the magnitude kC is considerably lower than that of the parameter γ. Accordingly we only fitted the orientational parameter, using

$$\gamma(\nu) = \tan^{-1}\left(\sum_i C_{\perp i} e^{-\frac{(\nu-p_i)^2}{2w_i^2}} \Big/ \sum_i C_{zi} e^{-\frac{(\nu-p_i)^2}{2w_i^2}}\right). \tag{5.3}$$

A simultaneous fit of both the ODEPR and MCD data sets yielded the most convincing agreement when the 450-850 nm region was decomposed into six Gaussian lines. This number agrees with that found for the MCD of poplar plastocyanin [47]. The parameters that produced this fit are summarized in Table 5.1. In addition, the fit was restrained by Eq. 5.1. Fig. 5.7 compares the experimental values of γ to the result of the fitting procedure, while Fig. 5.8 compares the experimental MCD spectrum to the calculated spectrum (solid line) and shows the contributions from the individual transitions.

The fitting process showed that it is essential to use both data sets. As discussed above, the longitudinal MCD does not provide orientational information, while the transverse MCD does not provide sufficiently precise magnitudes. Furthermore, cancellations between bands of opposite sign make the determination of band positions from the MCD alone relatively unreliable. This is particularly severe for the bands 2 and 3 and for bands 5 and 6. The orientational information from the ODEPR spectra provides here a significant improvement.

The fitted curve agrees well with the experimentally determined orientation γ, particularly in the low energy region. The first four bands have strong C_z-character. The opposite sign of C_z and $C_\perp$ for band 2 leads to the peculiar lineshapes encountered in this wavelength region. Clearly, the existence of band 2 is necessary to fit the ODEPR data. ODEPR can therefore help to find optical bands even where the total MCD is small (compare Fig. 5.8). For band 5 we find strong $C_\perp$-MCD, while band 6 is again mainly C_z-polarised. Also the major features of the high-energy region, i.e. the decrease towards $\pi/2$ in the center of band 5 are well reproduced. The remaining deviations may be attributed to the small size of the MCD in this region, which results in relatively noisy spectra and larger errors (see Fig. 5.7). In addition, the influence of the wings of optical transitions lying at higher energies have not been taken into account.

5.1.4 Comparison with Theory and Assignment

The central ion of copper proteins is a d^9 system; it is therefore sufficient to consider single electron orbitals. Since the position of the principal g-value axes in the molecular frame has been determined from single crystal spectroscopy [51], we are able not only to investigate the relative orientation of the optical and magnetic system, but also to determine the electronic transition dipoles along the molecular axes.

Ligand Field Transitions

We first consider transitions between fully occupied d-orbitals and the half-filled d_{xy}-orbital, which fall into the low energy part of our spectral region. The electronic structure of blue copper proteins has been studied by various quantum chemical techniques [51, 52, 53, 54]. Here we follow the choice of Gewirth and Solomon [47] who used D_{2d}-symmetry to predict the signs of the MCD bands of plastocyanin. The z-axis of our molecular coordinate system is close to the Cu-Met direction, while the x-axis is along the Cu-Cys direction.[2] In this symmetry the groundstate d_{xy} (i.e. the highest orbital) transforms as B_2, $d_{x^2-y^2}$ as B_1, d_{z^2} as A_1, and d_{xz}, and d_{yz} as E. The only allowed transitions are those from E to B_2 in xy-polarisation and from A_1 to B_2 for z-polarised light. For a detailed discussion of the group theory part see Appendix B.

To calculate the MCD, we must include the electron spin and consider the double group D'_{2d} [55]. In this group d_{xy} transforms as E" (Γ_7), $d_{x^2-y^2}$ as E" (Γ_7), d_{z^2} as E' (Γ_6), and d_{xz}, d_{yz} as E' + E" (Γ_6 + Γ_7) [34, 7]. This assignment of the orbitals to irreducible representations is also summarized in the level diagram in Fig. 5.9.

We consider first the allowed transition between the B_2 (E") ground state to the doubly degenerate state E (E' + E"). E' includes the $m_j = \pm 1/2$ states, E" the $m_j = \pm 3/2$ states. We expect negative MCD for the transition E (E") to B_2 (E") and positive MCD for E (E') to B_2 (E") [47].

The transition from B_1 is group theoretically forbidden. The transition from A_1 is allowed in z polarisation, but the MCD should vanish. However, spin-orbit coupling mixes these states with the E-states, thus adding xy-character to the corresponding transitions [56]. Accordingly, we expect the transition from B_1 (E") to show negative MCD and from A_1 (E') to show positive MCD. Considering the orientation of the MCD, we expect the xy-

[2]Please note that we have chosen a coordinate system which corresponds to the usual axes system in D_{2d}-symmetry and thus is rotated by 45° about the z-axis compared to the axes system used by Solomon et al.

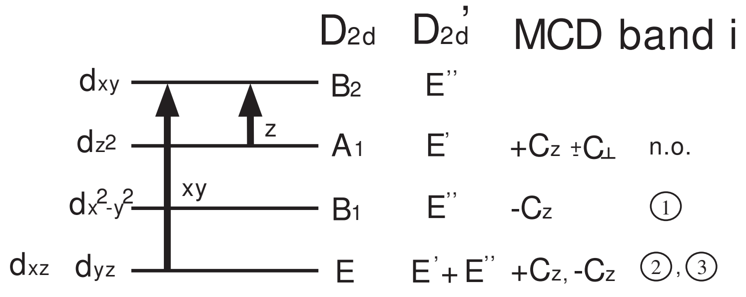

Figure 5.9: *Level diagram of d-orbitals and states in D_{2d}-symmetry and D'_{2d}-symmetry. Allowed transitions to the half occupied d_{xy}-orbital are indicated with arrows. The polarisations of these transitions are also given. The MCD-column gives the optical anisotropies which are predicted for D'_{2d}-symmetry. The right hand column gives the number of the assigned band allowing the comparison with Fig. 5.8. A transition from d_{z^2} was not observed (n.o.).*

polarised transitions from B_1 and E to contribute primarily through C_z, while the transition from A_1 should contribute to C_z as well as to $C_\perp$. These predicted optical anisotropies are also given in Fig. 5.9.

These predictions suggest the following assignment of the observed transitions (see Fig. 5.9): band 1 (10542 cm^{-1}) corresponds to the $d_{x^2-y^2} \rightarrow d_{xy}$ transition, band 2 (12594 cm^{-1}) to $d_{xz} \rightarrow d_{xy}$, and band 3 (13766 cm^{-1}) to $d_{yz} \rightarrow d_{xy}$. The transition from d_{z^2} is not observed, since its transition energy is below the range observed in our experiments [57]. We have summarized the assignment of the experimentally observed bands in the right hand column of Fig. 5.9. Our assignment predicts the correct signs and orientations for the observed transitions and leads to the same sequence of energy levels as in plastocyanin [47], whose active site is very similar to that of azurin.

Charge Transfer Transitions

Transitions between d_{xy} and fully occupied ligand orbitals dominate the high-energy region of the optical spectrum. The main absorption band 4 of azurin is at 15600 cm^{-1} (plastocyanin: 16700 cm^{-1}). The MCD of this band is dominated by C_z (see Table 5.1.). This can be rationalized in terms of a crystal field calculation taking into account spin-orbit coupling [58, 3]. Single crystal polarised absorption spectroscopy of plastocyanin showed that the dominant linear transition in this wavelength range originates from a

band i	p_i (cm^{-1})	$\Delta\varepsilon_{zi}$ (M^{-1} cm^{-1})	w_i (cm^{-1})	kC_{zi} (M^{-1}cm^{-1})	$kC_{\perp i}$ (M^{-1}cm^{-1})	γ_i
1	10542 ± 50	-50.6 ± 0.9	1080 ± 45	-18.5 ± 6.2	-1.8 ± 0.4	$1.03\pi \pm 0.01\pi$
2	12594 ± 110	22.4 ± 1.8	479 ± 55	15.4 ± 0.9	-2.6 ± 0.4	$1.95\pi \pm 0.01\pi$
3	13766 ± 75	-112 ± 4.4	587 ± 55	-33.9 ± 3.1	-5.3 ± 2.2	$1.05\pi \pm 0.02\pi$
4	15592 ± 20	-150.9 ± 0.9	1105 ± 15	-60.3 ± 10.1	-3.5 ± 1.8	$1.02\pi \pm 0.01\pi$
5	19907 ± 200	8.8 ± 0.9	744 ± 220	1.8 ± 0.9	1.8 ± 0.9	$0.25\pi \pm 0.11\pi$
6	21490 ± 200	-36.5 ± 1.3	976 ± 75	-11.4 ± 1.3	-2.6 ± 0.9	$1.07\pi \pm 0.02\pi$

Table 5.1: *Parameters of the six Gaussians (columns 2-4) which were used to fit the azurin MCD, Fig. 5.8. C_z- and $C_\perp$-character of the major optical transitions obtained from fitting the parameter γ (column 5,6). Column 7 contains the orientational parameter $\gamma_i = \arctan(C_{\perp i}/C_{zi})$ for each band.*

Cys S $\pi \to$ Cu d_{xy} transition. Spin orbit coupling (SOC) mixes character of other d-orbitals into the half-occupied d_{xy}-orbital. The corresponding matrix elements are tabulated (see for example [59], Ch. 6, and [3], Table E.2) and show that predominantly $d_{x^2-y^2}$-character is mixed into the ground state, so that the ground state $|G\rangle$ can be written as:

$$|G\rangle \simeq \left(|d_{xy}\rangle + \frac{i\lambda}{\Delta_{x^2-y^2}}\,|d_{x^2-y^2}\rangle\right)|+\rangle - \left(\frac{\lambda}{2\Delta_{yz}}\,|d_{yz}\rangle + \frac{i\lambda}{2\Delta_{xz}}\,|d_{xz}\rangle\right)|-\rangle\,, \tag{5.4}$$

and correspondingly the Kramers conjugate $\left|\bar{G}\right\rangle$

$$\left|\bar{G}\right\rangle \simeq \left(|d_{xy}\rangle - \frac{i\lambda}{\Delta_{x^2-y^2}}\,|d_{x^2-y^2}\rangle\right)|-\rangle + \left(\frac{\lambda}{2\Delta_{yz}}\,|d_{yz}\rangle - \frac{i\lambda}{2\Delta_{xz}}\,|d_{xz}\rangle\right)|+\rangle\,. \tag{5.5}$$

Δ_{d_i} are the energies of the corresponding d-orbital in comparison to d_{xy}, λ is the SOC constant, and $|\pm\rangle$ indicates a spin up and down state respectively. The excited state sulphur π-orbitals can be approximated as:

$$|E\rangle = |p_y\rangle\,|+\rangle \text{ and } \left|\bar{E}\right\rangle = |p_y\rangle\,|-\rangle \tag{5.6}$$

.

The optical transitions $|G\rangle \to |E\rangle$, $\left|\bar{G}\right\rangle \to \left|\bar{E}\right\rangle$ are represented by the matrixelements $\langle G|\,\hat{d}\,|E\rangle$ and $\left\langle\bar{G}\right|\hat{d}\left|\bar{E}\right\rangle$, where $\hat{d}$ is the optical dipole operator. While the transition from d_{xy} is polarised along the molecular x-axis (the direction of the Cu-Cys bond), the contribution from $d_{x^2-y^2}$ adds a transition dipole which is perpendicular and oscillates in phase quadrature. The contributions from d_{yz} and d_{xz} are much smaller due to the energy seperation and can therefore be neglected. As a consequence, the transition $\langle G|\,\hat{d}\,|E\rangle$ has opposite circular polarisation compared to $\left\langle \bar{G}\right|\hat{d}\left|\bar{E}\right\rangle$, and the different thermal population of the Zeeman substates leads to almost pure C_z-MCD [22]. Thus, band 4 is in excellent agreement with the assignment of this band as a Cys S $\pi \rightarrow$ Cu d_{xy} transition.

The remaining bands are the very weak, positive band 5 centered at 19900 cm^{-1} with predominantly $C_\perp$-MCD and the stronger negative band 6 at 21500 cm^{-1} with C_z character. Using the same arguments as for the Cys S $\pi \rightarrow$ Cu d_{xy} transition, we expect the transition His N $\rightarrow$ Cu d_{xy} to contribute mainly to C_z-MCD. This would allow us to assign this transition with band 6, in analogy to plastocyanin [47]. Since the g-tensor is axially symmetric, we cannot orient the dipole moment in the xy-plane and are therefore unable to distinguish contributions from the two histidines.

As we discussed in the previous section, the weak band 5 shows a significant $C_\perp$-MCD, i.e. this transition has components along the z-axis. Since this band is relatively weak, the precision of the orientation angle is relatively low for this band and does not allow a detailed analysis. Gewirth et al. assign the corresponding band in plastocyanin to a Cu $d_{xy} \rightarrow$ pseudo-σ S transition. Our results are compatible with such an assignment but indicate that the transition moment is significantly tilted from the Cu-S axis.

5.1.5 Discussion

In this chapter we presented the results of ODEPR measurements on the blue copper protein azurin. We have shown that the microwave-modulated MCD from optically detected EPR spectra provides an excellent opportunity to determine the orientation of optical transition dipoles relative to the molecular axis system for this protein. This is achieved by correlating the optical anisotropy with the known orientation of the magnetic axis system. Compared to alternative methods like MCD saturation curves, the accuracy of ODEPR is much higher, since different components of the optical anisotropy contribute to different parts of the ODEPR spectrum. This is particularly important in systems with small g-value anisotropy like copper proteins [11].

To extract the spectral information we analysed the active center in terms of the D_{2d}-symmetry group. While this is a relatively crude approximation of the site, it appears to lead to a consistent assignment of the optical spectrum. The molecular geometry and the high-field EPR spectra [46] indicate significant rhombic distortions from an axial symmetry, as in plastocyanin [47]. This provides an explanation for the weak but significant

$C_\perp$-character in all d-d bands. We have also given an interpretation of the charge-transfer bands by including spin-orbit coupling in the ground state. For plastocyanin, Gewirth et al. have verified and refined their assignment with SCF-calculations; similar calculations would also be desirable for azurin.

The application of this technique to azurin has clearly shown that the combination of longitudinal and transverse MCD spectra provides additional information for the distinction and assignment of optical transitions. While the absorption spectrum is almost featureless, the MCD indicates the presence of several bands. Extracting positions, amplitudes and linewidths from the MCD spectrum alone remains difficult, however, particularly in regions where bands of opposite sign overlap. The additional information on the orientation of the optical anisotropy from the transverse MCD provides significant improvement in these spectral regions.

Sample heating and microwave saturation are critical points in our experiment and put limits on the accuracy of the data. However, we have shown that the basic information nevertheless can be extracted from the data. Clearly some more work is necessary to improve the optical quality of our samples.

5.2 Copper Model Complexes

Due to the relative simplicity of their geometric and electronic structure, tetrahalogeno copper complexes have been extensively studied with theoretical and spectroscopical methods [34, 60, 61]. These complexes have also been of interest as model compounds for the blue copper site. Solomon and coworkers enlarged their theoretical treatment of CuCl-complexes towards the interpretation of the results from plastocyanin [47, 30]. Our motivation for the study of these species was the possibility to investigate another copper complex, which allows us to draw a parallel to the results from azurin. In addition, we were able to compare the results from ODEPR with those obtained from MCD-quenching experiments, where some experimental results have been reported previously [62, 17]. Another advantage is the practicality of model compounds: the samples are readily prepared (see section Experimental) as randomly oriented molecules in a film matrix, their optical quality is mostly superior to protein samples, and they can be easily handled in the ODEPR experiment.

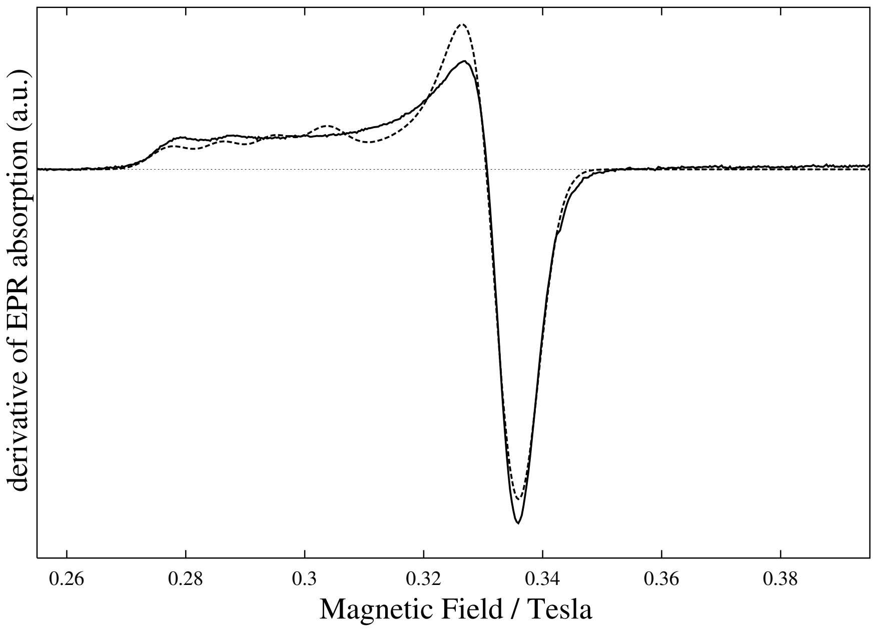

Figure 5.10: *EPR spectrum of a ($Et_4N)_2CuCl_4$-film at 9.5 K, 9.6 GHz (solid line) and fit curve (dashed line).*

5.2.1 $(Et_4N)_2CuCl_4$-Films

The conventional EPR spectrum of a $(Et_4N)_2CuCl_4$ in a cellulose acetate film is shown in Fig. 5.10 as solid line. A simulation of the spectrum is also given (dashed line). The parameters obtained from the fit are $g_z = 2.37$, $g_\perp = 2.07$, A_z=288 MHz, $A_\perp$=34 MHz. A Gaussian lineshape was used with σ=109 MHz. A_z has a typical value for inorganic copper complexes and is much larger than A_z for azurin. The agreement between the experimental spectrum and the fit curve is not very convincing. This can of course be a lack of the model, which is the same as for azurin, but with optimized parameters. It might however also indicate some distortion due to the high concentration of copper ions in the sample. This idea is supported by the rather broad linewidth of 109 MHz, which is nearly twice the linewidth used for the azurin simulation.

The infrared MCD spectrum of a $(Et_4N)_2CuCl_4$-film is given in units of ΔA_z in Fig. 5.11. Additional data like the MCD spectrum and the absorption spectrum in the visible region is shown in Appendix C. The absorption for the infrared is not given since the films do not exhibit any measurable absorption bands in this wavelength region. It is well established that the ligand-field transitions lie in the infrared region, while the charge-transfer transitions can be found in the visible region of the spectrum. The signal amplitudes are given in units of ΔA_z instead of $\Delta\varepsilon_z$ since we were unable to determine the exact thickness and thus the concentration of the film.

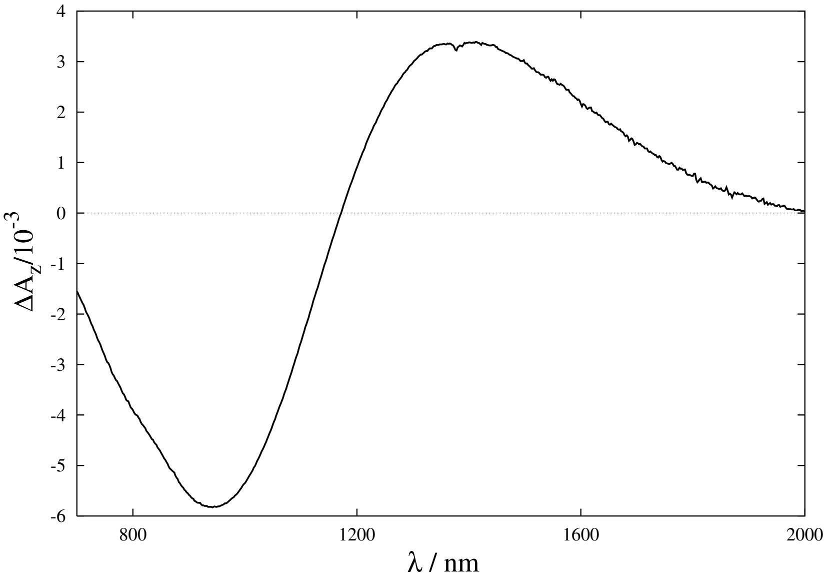

Figure 5.11: *Infrared MCD of a $(Et_4N)_2CuCl_4$-film at 1.6 K, 5 Tesla.*

The only transition easily accessible with equipment from our laboratory was the ligand-field transition around 915 nm. The ODEPR dispersion signal measured at this wavelength is shown in Fig. 5.12 (thin, solid line). The spectrum looks rather broadened and does not possess a very good signal-to-noise ratio. A simulation of the ODEPR spectrum with the parameters obtained from the fit of the conventional EPR has been performed. We found that a linewidth of 400 MHz is suitable to model the ODEPR spectrum. This is much larger than the linewidth of the conventional EPR and therefore indicates saturation also of the dispersion lineshape.

The fitting process revealed that the ODEPR spectrum of the CuCl-film can be modelled best with complete $C_\perp$-anisotropy. The corresponding spectrum is given in Fig. 5.12 (thick line). Especially the low-field region of the experimental spectrum is well reproduced, while the high-field peak is not in optimal agreement with the data. For comparison we have also given an ODEPR spectrum with complete C_z-polarisation (dashed line). Clearly this spectrum is not suitable to fit the experimental data. Therefore we can be quite confident with the assignment of the 915 nm-transition to be strongly $C_\perp$-polarised, although line broadening obscures the features of the spectrum. This finding is in agreement with previous measurements [62, 17].

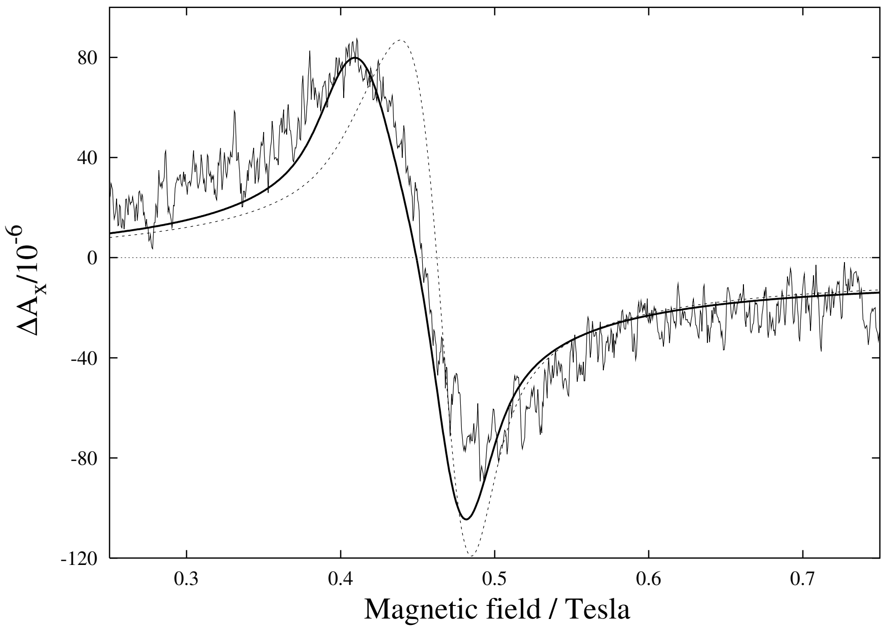

Figure 5.12: *ODEPR signal of a* $(Et_4N)_2CuCl_4$*-film (thin, solid line) at 915 nm, 1.8 K, 13.67 GHz. The fit curve shows that the optical transition is dominated by* $C_\perp$ *(thick, solid line). For comparison also a curve for* C_z*-anisotropy is given (dashed line).*

5.2.2 $(Et_4N)_2CuBr_4$-Films

Conventional EPR spectra of $(Et_4N)_2CuBr_4$ in cellulose acetate films did not reveal a typical copper EPR spectrum with clearly resolved hyperfine peaks, but just showed a single broad resonance at g=2.13. Thus, the EPR spectrum is not reproduced here. The lineshape is probably a consequence of a too high concentration of interacting copper ions. This assumption was confirmed by detection of another EPR resonance corresponding to a g-value of 4. This most likely stems from copper ions which form a singlet and a triplet state via exchange interaction. Additional dipolar interaction leads to zero field splitting in the triplet state and makes the transition $m_j = |-1\rangle \rightarrow m_j = |1\rangle$ slightly allowed, resulting in a g=4 signal.

ODEPR spectra could be easily measured (see Fig. 4.4). However, it could be observed that the spectra drastically broadened with increasing microwave power. This unusual effect is also considered to stem from the very high copper ion concentration. It was not possible to detect ODEPR spectra with different lineshapes due to an optical anisotropy of the MCD, which is not surprising taking into account the obscured EPR spectrum.

We restricted the use of this sample to the study of general aspects of our experiment, such as Faraday rotation etc. (Section 4.2). Barrett et al. did manage to demonstrate in the MCD-quenching experiment that the optical anisotropies of different optical bands modified the ODEPR signal. However, since these experiments were done at high magnetic field corresponding to 35 GHz this might have decoupled the interacting copper ions, where at 9 / 14 GHz exchange interaction dominates the EPR spectrum.

We found that the solution of CuBr appeared green, while the $(Et_4N)_2CuBr_4$-films are purple. It is therefore quite obvious that the configuration between liquid and film phase changes drastically, bearing the risk of undefined species in the film.

5.2.3 Comparison with Theory and Discussion

An assignment of the electronic transitions of $CuCl_4$-compounds has been made by several authors on the basis of D_{2d}-symmetry [34, 60, 61], which is indicated in Fig. 5.13. In the light of this symmetry the strong $C_\perp$-character of the transition at 915 nm might indicate that this line stems from a $d_{z^2} \rightarrow d_{xy}$ transition, which is the only transition in D_{2d}-symmetry which should show a significant transition dipole along the molecular z-axis (Fig. 5.9). In contrast to azurin the $d_{z^2} \rightarrow d_{xy}$ transition would then be the d-d transition with the highest energy.

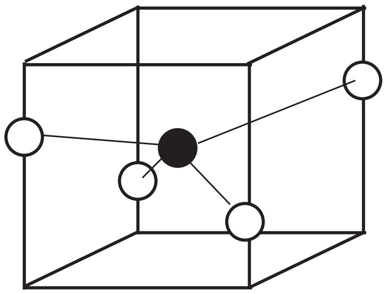

Figure 5.13: *The geometry of CuX_4^{2-} (X=Cl,Br) in D_{2d}-symmetry.*

As expected, the acetate films yield large ODEPR signals with a good signal-to-noise ratio. However, in contrast to proteins the very few atoms ligating the central copper ion lead to very strong interaction between the copper ions. This can only be avoided by a very careful sample preparation and a high dilution of the copper compounds in the film. Some more research in this direction is clearly necessary. In addition, we found it very unsatisfying to do experiments with a sample where the configuration of the molecules is not really clear. Especially for the CuBr there is strong evidence that a mixture of differently ligated copper ions exists in the film [3]. In the light of this result it is doubtful if the investigated complexes are ideal for the ODEPR

[3]Prof. Wieghardt (MPI Mühlheim) declared this sample to be a typical example of the strong tendency of physicists "to measure a crap sample in a sophisticated experimental setup".

experiments described above, since the experimental results can hardly be interpreted. Some copper compounds which are known to be extremely stable against a changing chemical environment would be suitable for preparation in acetate films. First steps in this direction have been made via a contact to the MPI Mühlheim; Dr. Claudio N. Verani generously provided a polycrystalline sample of an appropriate Cu-complex.

Chapter 6

Rubredoxin

Rubredoxins are small proteins containing a single [Fe(S-Cys)$_4$]-cluster, where the iron is approximately tetrahedrally coordinated to the cysteinate sulfurs. This coordination is clearly visible in Fig. 6.1, where the structure of the molecule is schematically depicted. [1]

Rubredoxin is the simplest iron-sulfur system compared to the other members of the family of proteins with iron-sulfur clusters. Other proteins possess two, three, or four sulfur-coordinated Fe-atoms. Many of the proteins function in electron transport [31]. The relative simplicity of the active site of rubredoxin makes the protein an ideal candidate for investigations with a variety of spectroscopic techniques.

6.1 Electron Paramagnetic Resonance

6.1.1 The Rubredoxin Groundstate

An adequate, phenomenological spin Hamiltonian (SH) describing the groundstate of a Fe(III)-high spin complex (S=5/2) with rhombic symmetry is [2]

$$\mathcal{H} = \mu_B g(B_x\hat{S}_x + B_y\hat{S}_y + B_z\hat{S}_z) + D(\hat{S}_z^2 - 1/3S(S+1)) + E(\hat{S}_x^2 - \hat{S}_y^2), \quad (6.1)$$

where μ_B is the Bohr magneton, g is the isotropic g-value (g=2), and the B_i are the components of the static magnetic field along the corresponding SH-axis. D and E are the second rank axial and rhombic coefficients, respectively, of the zero-field spin Hamiltonian. It is convention in EPR spectroscopy to choose the axes of the spin Hamiltonian such that $E/D \leq 1/3$,

[1] The corresponding pdb-file was 1IRO. The figure was produced using the programs Molmol and Povray.

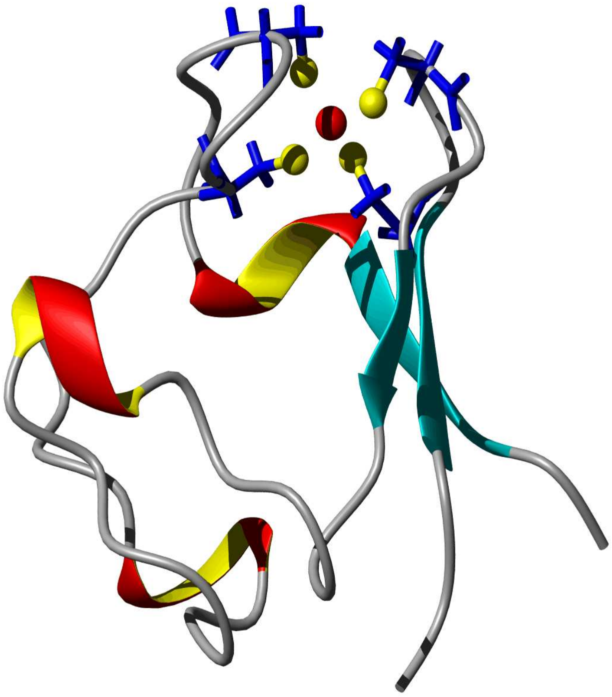

Figure 6.1: *Chain structure of Clostridium pasteurianum rubredoxin. Clearly visible is the Fe-atom (red) tetrahedally coordinated by four sulfur atoms (yellow).*

which means that the major splitting axis is labelled z. For an axial case, E=0, whereas in an extreme rhombic geometry the ratio $E/D = 1/3$. For rubredoxin, a slight deviation from extreme rhombic symmetry is observed [63]. Diagonalisation of the Hamiltonian yields the energy levels for each principal direction, as is depicted in Fig. 6.2. For small fields, the states can be described as three Kramers doublets, which are well seperated by a zero-field splitting of approximately $4\sqrt{7}/3D \simeq 3.5D$. As a consequence, these doublets can be treated as three S=1/2 states and effective g-values for three Kramers doublets can be determined for each doublet. If D is positive, with a ratio of E/D=0.25 we find for the low energy doublet g_{xl} = 1.46, g_{yl} = 9.4, and g_{zl} = 0.92, for the medium energy doublet g_{xm} = 4.08, g_{ym} = 3.76, and g_{zm} = 4.76, and for the highest energy doublet g_{xh} = 0.47, g_{yh} = 0.36, and g_{zh} = 9.84 [63]. Although it is normally the convention in EPR to label the largest g-value g_z and the smallest g_x, we use here the axis system defined by the zero-field spin Hamiltonian for all Kramers doublets. If the sign of D was negative, the g-values for highest and lowest doublet would be exchanged. At high fields, the states begin to mix and the approximation as three seperate S=1/2-doublets does not hold any longer.

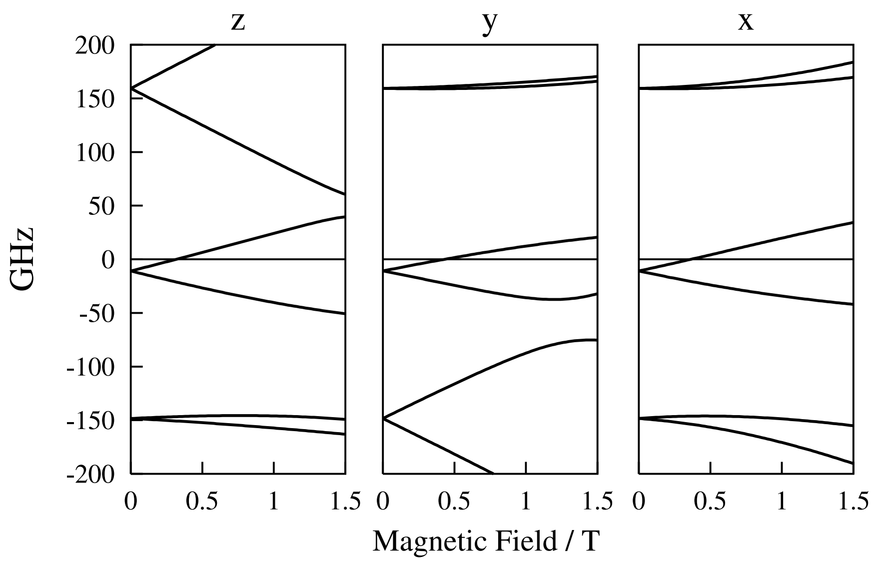

Figure 6.2: *Energy levels in the three principal directions of rubredoxin using D = 46.3 GHz and E/D = 0.25 as a function of the magnetic field. The vertical energy axis is in GHz.*

6.1.2 Conventional EPR Spectra

We measured conventional EPR spectra of rubredoxin at 9.6 GHz at three different temperatures: 4 K, 8.1 K and 18.8 K. The spectrum at 8.1 K is depicted in Fig. 6.3. The feature between 0.12 and 0.2 Tesla stems from the medium energy doublet, the peak at 0.07 Tesla is due to g_{yl}=9.4.

As a first step, we extracted the spectral parameters such as D, E, and linewidth from the conventional EPR spectrum. We focused on the signal from the medium doublet whose splitting is a direct measure for the deviation from complete rhombicity. It is quite striking that the g_{zm} and g_{ym} resonance of the medium doublet are rather broad, while the center peak is very sharp. We assumed that a statistical variation of E and thus the ratio E/D might lead to the observed EPR pattern. A statistical distribution of crystal field parameters is a frequently used concept in EPR theory and normally called "g-strain". We extended this model to an "E/D"-, i.e. a rhombicity-strain.

For the actual calculation of the spectrum, we diagonalized the spin Hamiltonian for a given E and D. From the obtained eigenvalues we calculated the effective g-values. The magnetic resonance condition is then $\hbar\omega_0 =$

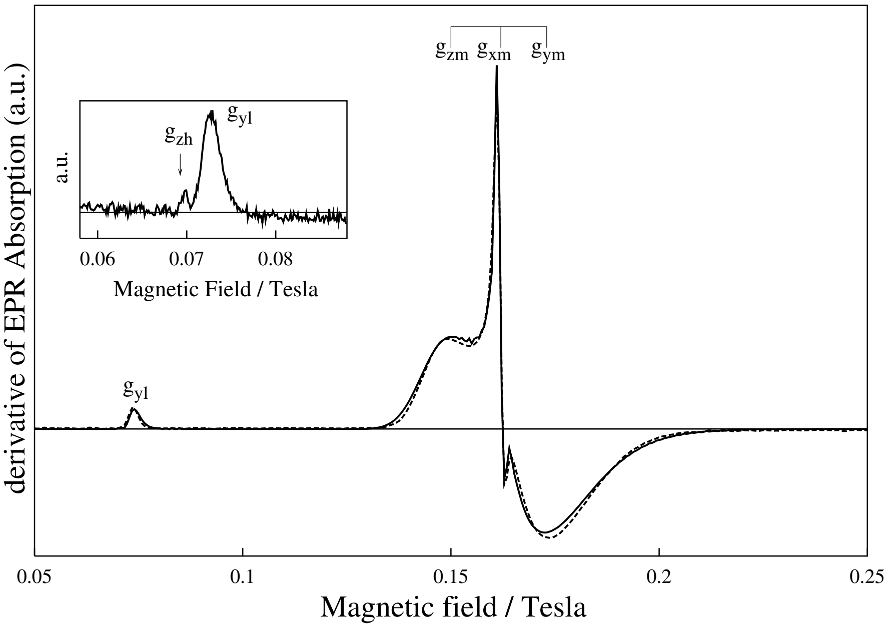

Figure 6.3: *Conventional EPR-spectrum of rubredoxin, 8.1 K, 9.6 GHz (dashed line) and fit curve (solid line). Inset: conventional EPR spectrum at 18 K,* g_{yl}*=9.4 -resonance together with the* g_{zh}*=9.84-resonance at lower field.*

$g_{eff}(\theta,\phi)\mu_B B_0$, where θ is the angle between the g-value z-axis and the static magnetic field B_0 and ϕ is the angle between the projection of B_0 onto the xy-plane and the x-axis. The orientation-dependence of the g_{eff}-factor for each doublet is $g_{eff}(\theta,\phi)^2 = g^2_{z_{eff}} \cos^2\theta + g^2_{x_{eff}} \sin^2\theta \cos^2\phi + g^2_{y_{eff}} \sin^2\theta \sin^2\phi$ [64]. In the following the system was treated as three separate pairs of Zeeman-levels, which are thermally populated. This procedure is much less time consuming than proceeding with the full Hamiltonian, since there exist analytic expressions for the transition matrix elements for a S=1/2 system of a powder-like sample [2, 3] (see also Appendix A). The procedure was then repeated for a slightly changed E/D-value. Some of these spectra are depicted in Fig. 6.4. Finally all spectra with different E/D-values were added up according to a Gaussian distribution with linewidth σ around a center value $(E/D)_0$. With this model a fit of the medium doublet EPR signal (0.12 - 0.2 T, Fig. 6.3) has been performed. The shape of this spectral feature is unsensitive to temperature changes. We obtained a very good agreement between the experimental and the calculated spectrum for a ratio $(E/D)_0 =$ 0.25 and a Gaussian distribution of E/D with a width of $\sigma_{E/D}$=0.03 with a linewidth σ=27 MHz.

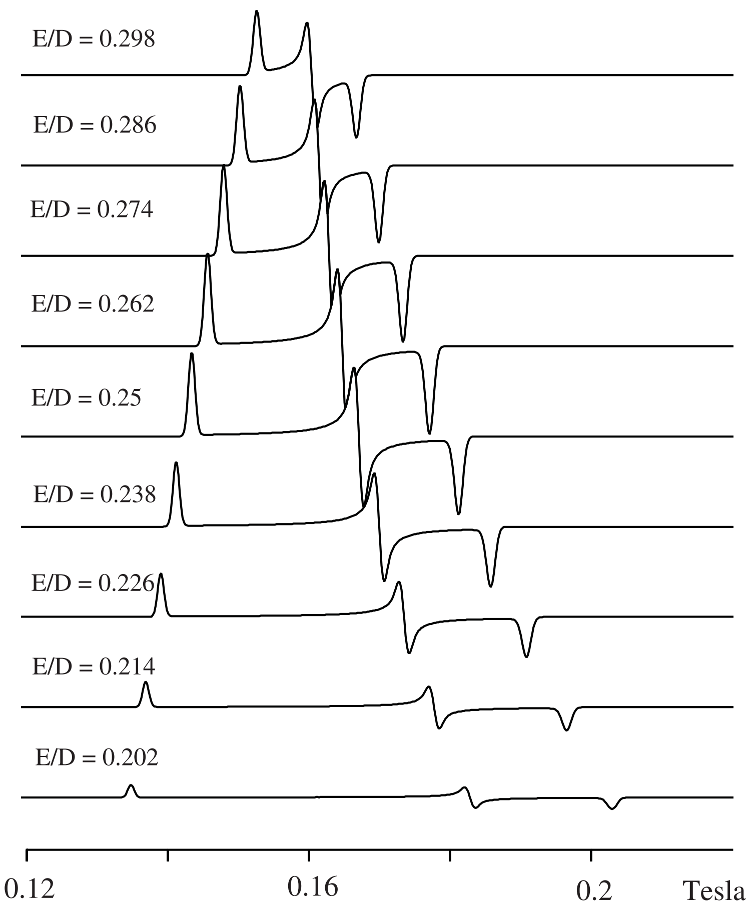

Figure 6.4: *Spectra with various ratios E/D. The spectra are scaled according to a Gaussian distribution.*

As a next step we determined the absolute value of D from a fit of the rubredoxin EPR spectrum over the full field range. The result is depicted in Fig. 6.3 for a spectrum measured at 8.1 K. Due to the different thermal population of the three doublets, a comparison of the signal from the lowest energy doublet, which is basically the g_{yl}=9.4 resonance, and the medium doublet allows a determination of the size of D. Altogether we performed fits at all three different temperatures where spectra have been measured. From these three spectra a value of $D = 46.3 \pm 2.1$ GHz was determined. This is in agreement with results from by Mössbauer studies within the error of the data ($D = 57.8 \pm 8$ GHz [65]), and agrees with previous EPR studies from *Pseudomonas oleovorans* rubredoxin, where a D of 52.8 GHz was obtained [63]. These results show that a treatment of the rubredoxin groundstate as three Zeeman-doublets is an adequate approximation at 9.6 GHz.

The deviation from complete rhombicity enables us to analyse also the sign of D, which we determined within the convention that $0\leq E/D \leq 1/3$ and in agreement with *Pseudomonas oleovorans* [66] to be positive. This can be easily understood by inspection of the low field at high temperatures. A detailed scan shows a small peak on the low field side of the g_{yl}-feature from the low energy doublet (inset, Fig. 6.3). This stems from the highest energy doublet, which becomes thermally populated at 18 K. The small peak corresponds to a g_{zh}-value of 9.84. If the sign of D was negative, the lowest and the highest energy doublet would swap, so that the small high energy doublet peak should lie at g_{yh}=9.4 and appear on the *high field side* of the dominating g_{zl}=9.84 feature. This is in contradiction to our observation, leading to conclusion that D must have a positive sign.

6.2 Optically Detected EPR

Fig. 6.5 gives a survey of the strong variation of the ODEPR lineshape with the wavelength of the detection laser. The figure contains four spectra (dots) measured at different wavelengths, at a temperature of 1.8 K and microwave frequency of 13.7 GHz. The microwave power was 120 mW for the spectra at 514 and 560 nm and 180 mW for the spectra at 476 and 532 nm.

The spectra are plotted as $\Delta\varepsilon_x$, the difference in extinction coefficients for left and right circularly polarised light. Only the dispersion signal is given, since the absorption signal is strongly saturated under our experimental conditions. Characteristic for the dispersion lineshape are the very strong high field tails.

At 1.8 K the spectra are dominated by the low energy Zeeman doublet. The medium energy doublet contributes only via a rather small feature around B=0.25 T where different g-values are not resolved for the dispersion. As a consequence, the spectrum at 514 nm is dominated by the g_{xl}-resonance around 0.7 T. This feature shows again that the sign of D must be positive, since otherwise the medium g-value would be 0.47 and the spectrum considerably shifted towards higher fields. No resonance from g_{yl}, which is expected at 0.1 T can be seen. The spectrum at 476 nm exhibits similar features, except that the sign of the spectrum is reversed and the medium doublet resonance is larger.

At 532 nm (right hand column, upper trace of Fig. 6.5), the spectrum is comparable to the 514 nm spectrum, but includes an additional resonance from g_{yl} at 0.1 T. The 560 nm spectrum is dominated by the low field features (g_{yl} and g_m).

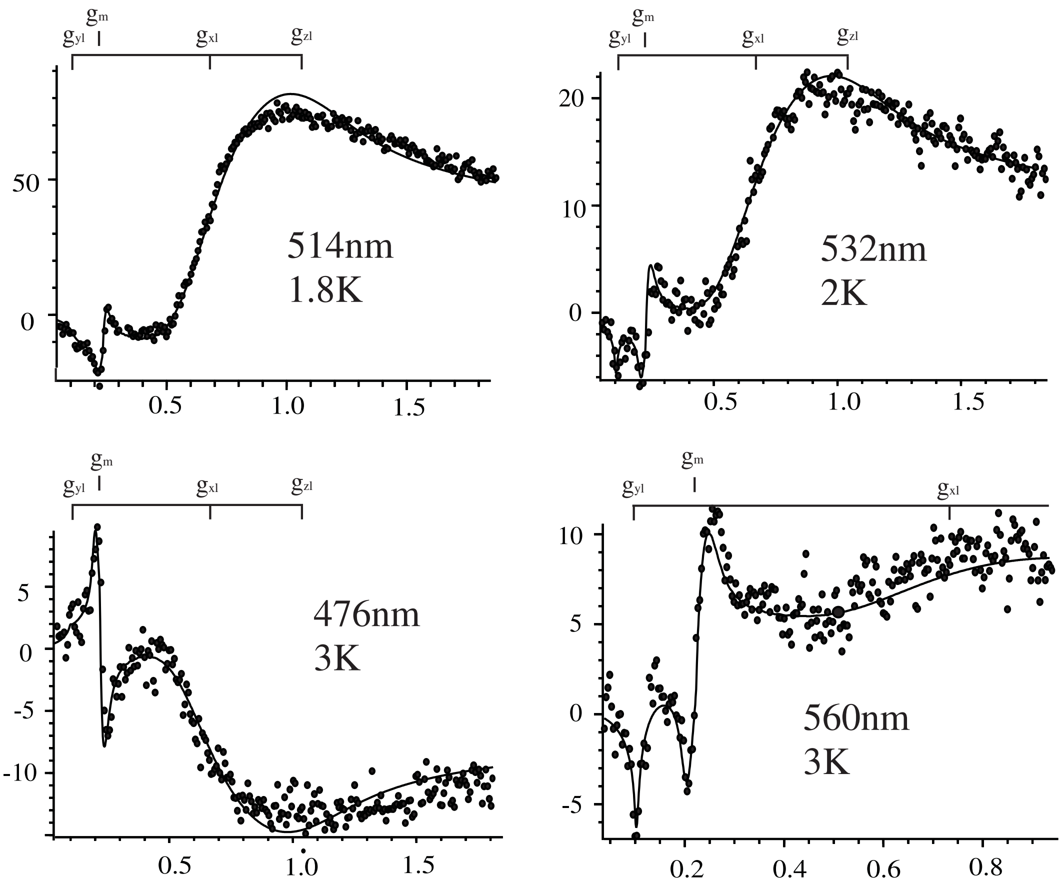

Figure 6.5: *Four experimental ODEPR spectra measured at different wavelengths (points) in units of $\Delta\varepsilon_x \times 10^{-3}$ M^{-1} cm^{-1}. Also the corresponding fit curves (solid lines) and the local temperature used for the fit are given.*

6.2.1 Wavelength-Dependence of the Optical Anisotropy

To extract the optical anisotropy, we fitted each spectrum, using the parameters obtained from the conventional EPR spectra. The fit was based on Eq. 2.13, which describes the ODEPR signal for a S=1/2 system with three distinct g-values. In analogy to conventional EPR, we calculated the expected ODEPR spectrum for each doublet separately and added contributions from all three doublets. Three prototypical, calculated rubredoxin ODEPR dispersion spectra for the three extreme cases of exclusively C_x-polarisation (C_y=C_z=0), C_y-polarisation (C_x=C_z=0), and C_z-polarisation (C_x=C_y=0) are given in Fig. 6.6. The temperature was set at 1.8 K, the resonance frequency was 13.7 GHz.

The first and the third curve, which show low intensity in the high field region, look rather similar. This effect stems from g_{xl} and g_{zl} lying close together in comparison to g_{yl}, resulting in a quasi-axial arrangement. In addition the E/D-strain obscures the high field features. The second curve is due to C_y only, which means that the g_{yl}=9.4-resonance is strongly suppressed. In contrast, g_{xl}=1.46 dominates the spectrum. The medium energy doublet, indicated by g_m, contributes only via a small dispersion-like peak at 0.25 Tesla.

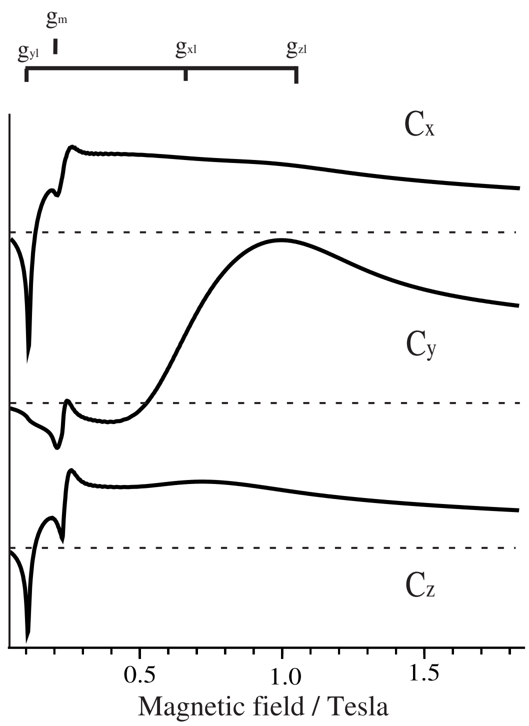

Figure 6.6: *Three calculated dispersion type ODEPR spectra with the parameters extracted from fitting the conventional EPR of rubredoxin (D=46.3, E/D =0.25, $\sigma_{E/D}$ = 0.03). The upper trace shows a spectrum expected for exclusively C_x-polarisation, the middle trace C_y-polarisation, and the bottom trace C_z-polarisation. The g-values of the lowest and the medium energy doublet are also given. The corresponding temperature was set as 1.8 K, the frequency was 13.7 GHz.*

The ODEPR spectrum measured at 514 nm is very similar to the second trace in Fig. 6.6. We performed a fit of the 514 nm spectrum on the basis of the spectra in Fig. 6.6, which is depicted in Fig. 6.5 as solid line. This fit gave a value of at least 92% C_y-polarisation for the spectrum at 514 nm. The fit curve models not only the low field region, but also the g_{xl} = 1.46 feature well. Although at a field higher than 1 Tesla the concept of effective g-values is not strictly valid any more, we found that the ODEPR dispersion lineshape is relatively unsensitive to the exact position of the high-field g_{zl}-value. Thus, the S=1/2 approach is still a good approximation and allows us to characterize the optical transition at 514 nm as polarised along the SH x- and z-axis.

The sign reversal from 514 to 476 nm parallels the sign reversal in the MCD spectrum (Fig. 6.8). At 476 nm the g_m=4.3 resonance is somewhat larger than in the 514 nm spectrum, which most likely stems from a slight heating of the sample by the laser beam due to a higher intensity of the laser beam. A local temperature increase of 1K leads already to a significant increase of the medium doublet resonance. Indeed we found that a local temperature of 3 K gave good results for the fit, where at a temperature of 1.8 K no satisfying fit of the g_m=4.3 resonance could be obtained. Setting the temperature at 3 K we found again predominant C_y-polarisation for the transition at 476 nm. The local temperature used for the fit is also indicated in the figure. Similar results have been obtained at 458 nm, where we found that a temperature 2.2 K gave optimal results (not shown).

The situation is different at 532 nm. Fits showed that the contribution of C_x and C_z are practically undistinguishable, so that we can treat these both polarisations as one combined $C_{xz} = 1/2(C_x + C_z)$. Within this assumption we found that the ratio C_{xz}/C_y is approximately 0.5 at 532 nm (local temperature 2 K). Towards longer wavelengths the g_{yl}-peak becomes increasingly prominent and finally results in the spectrum measured at 560 nm, which shows very low intensity in the high field region. This reveals a strong dipole along the molecular y-axis being present. From the fit we determined the ratio of C_{xz}/C_y as approximately 1.3.

We restricted our experiments to the low temperature region where the spectrum is dominated by the low energy doublet. Since the magnetic anisotropy is extremely large for this doublet, it is feasible to make conclusions about optical anisotropy even with a relatively poor signal-to-noise ratio. Inspection of the experimental spectra shows that the medium doublet is not sufficiently resolved to allow a detailed analysis of the lineshape.

6.2.2 Relation to MCD

As described in Chapter 2, ODEPR can be considered as microwave-modulated MCD. Correspondingly, the optical properties derived from these experiments are closely related to longitudinal MCD spectra. The absorption and the MCD spectrum of *Desulfovibrio gigas* rubredoxin was analyzed in detail by Oganesyan et al. [35] to derive the electronic structure of the Fe center. From the MCD spectrum the authors were able to identify six charge transfer transitions in the visible and near UV region of the spectrum. Four of these transitions fall into the spectral range covered by our experiments; the relevant data for these transitions are summarized in Table 6.1.

Figure 6.7 shows the corresponding room temperature absorption spec-

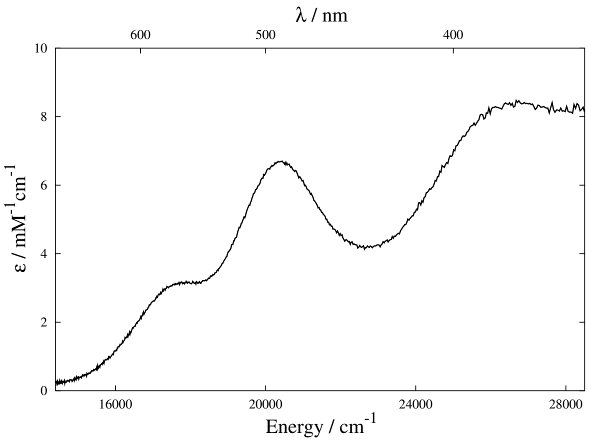

Figure 6.7: *Room temperature absorption spectrum of oxidized Clostridium pasteurianum rubredoxin in units of the molecular extinction coefficient* ε.

trum. In Figure 6.8 we show the four relevant low energy charge transfer MCD bands [35], whereby band 1, 2 and 4 have been assigned to have a Gaussian lineshape, while band 3 is correlated with a group theoretical E-term and appears therefore as an asymmetrical Gaussian derivative shape. Also given in this figure is the ratio C_{xz}/C_y as determined from ODEPR measurements measured at the corresponding wavelengths (right hand scale, filled circles). The ratio C_{xz}/C_y is close to zero for band 3 and band 4. Thus, we conclude that these bands are strongly C_y-polarised. From the ODEPR spectrum measured at 560 nm the ratio C_{xz}/C_y is 1.3 resulting in band 1 having a significant C_{xz}-contribution and thus a dipole along the SH y-axis. The considerable C_{xz}-polarisation at 532 nm (18797 cm^{-1}) agrees well with the weak band 2 situated at this position which also has a strong dipole along y. Following the same principles which we developed in [67] to determine the polarisation of overlapping optical bands, we determined the polarisation of band 1 to be approximately $C_{xz}/C_y = 1.4$ and band 2 to be approximately $C_{xz}/C_y = 1.0$. These assignments are summarized in the last column of Table 6.1.

band number	band number acc. to [35]	center energy [35]	MCD pattern [35]	polarisation from ODEPR
1	1	17541	Gaussian	C_{xz}/C_y=1.4±0.4
2	6	18975	Gaussian	C_{xz}/C_y=1.0±0.4
3	4	20243	Gauss. deriv.	C_{xz}/C_y=0 ± 0.1
4	5	21739	Gaussian	C_{xz}/C_y=0 ± 0.1

Table 6.1: *Relevant parameters for the four low-energy charge transfer bands. The optical polarisation as determined from ODEPR is given in the last column.*

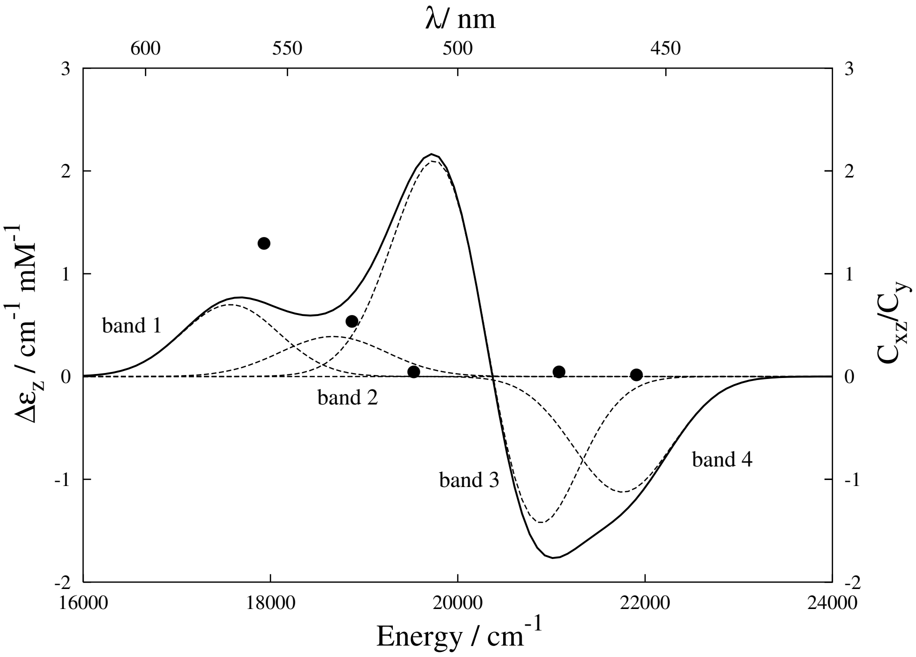

Figure 6.8: *Four low energy charge-transfer bands of the MCD spectrum of rubredoxin (according to [35]). The solid curve is the resulting of these bands. The ratio of C_{xz}/C_y from ODEPR is also given in the Figure (right hand scale).*

These findings can be compared with the assignment of the rubredoxin optical bands due to theoretical predictions made on the basis of D_{2d}-symmetry. The spectral features in the visible region have been assigned to arise from charge-transfer transitions $\mathrm{S}_\sigma \rightarrow \mathrm{Fe(III)}_\sigma$. Oxidized rubredoxin has a ground state $^6\mathrm{A}_1$. Allowed transitions are in D_{2d} only possible from $^6\mathrm{A}_1 \rightarrow {}^6\mathrm{B}$ and $^6\mathrm{A}_1 \rightarrow {}^6\mathrm{E}$, where the former transition is polarised along the symmetry axis and the latter polarised in a plane perpendicular to the symmetry axis.

Fig. 6.9 depicts the one-electron levels of high spin Fe(III)under D_{2d}-symmetry [68]. Among all $\mathrm{S}_\sigma \rightarrow \mathrm{Fe(III)}_\sigma$ transitions only the two following one-electron transitions belong to ^{6}B: S(e) $\rightarrow$ Fe(e) and S(a) $\rightarrow$ Fe(b_2). Three one-electron transitions belong to ^{6}E: S(b_2) $\rightarrow$ Fe(e), S(a_1) $\rightarrow$ Fe(e), and S(e) $\rightarrow$ Fe(b_2).

On the basis of single crystal polarisation data the transition $^6\mathrm{A}_1 \rightarrow {}^6\mathrm{B}$ (S(e) $\rightarrow$ Fe(e)) must have significant polarisation along the D_{2d}-symmetry axis and thus was assigned to be band 1 at 570 nm. In contrast, the transition from $^6\mathrm{A}_1$ to the doubly degenerate ^{6}E-state (S(a_1) $\rightarrow$ Fe(e)) is polarised in a plane perpendicular to the D_{2d}-symmetry axis, and this has been assigned to the derivative-shaped band 3 at 494 nm. Band 4 stems from a transition

$^6A_1 \rightarrow {}^6E$ ($S(e) \rightarrow Fe(b_2)$) and exhibits mainly polarisation perpendicular to the symmetry axis. Band 2 has been assigned to arise from a weak distortion from D_{2d}-symmetry and to show a strong dipole along the optical symmetry axis. The two remaining single electron transitions belong to charge-transfer bands at higher energies and are not discussed here.

Spin-orbit coupling mixes polarisation of different bands into some transitions. This is in particular the case for band 1 and 2, since a single dipole along the symmetry axis is not sufficient to exhibit MCD. Since intensity from the ^{6}E-state is coupled into the ^{6}B-state, these transitions can gain polarisation perpendicular to the symmetry axis.

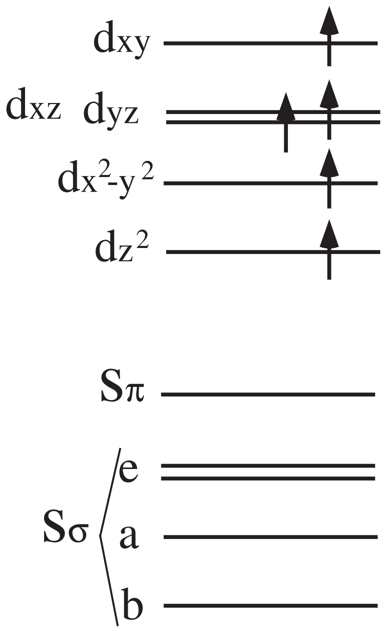

Figure 6.9: *One electron energy levels of high spin Fe(III) under D_{2d}-symmetry, which are double occupied up to the sulfur orbitals and half occupied in the Fe-d-orbitals.*

Within the D_{2d} analysis of the rubredoxin molecule, the ODEPR analysis unambiguously shows that the direction of the largest g-value (the SH y-axis in standard EPR notation) coincides with the S_4 axis. This finding is in agreement with [69] and [35]. However, it is important to note that the authors of [35] define the SH-z-axis to be parallel to the symmetry axis. This misleading assignment of the axis system leads to the incorrect result that D would be negative.

Our assignment of the axis system can be readily verified by considering for example band 3, for which single crystal polarised absorption spectroscopy [70] showed that it is polarised in the plane perpendicular to the D_{2d}-symmetry axis, while our experimental data are only compatible with C_y polarisation. Thus, the SH-y-axis lies along the D_{2d}-symmetry axis.

6.3 Discussion

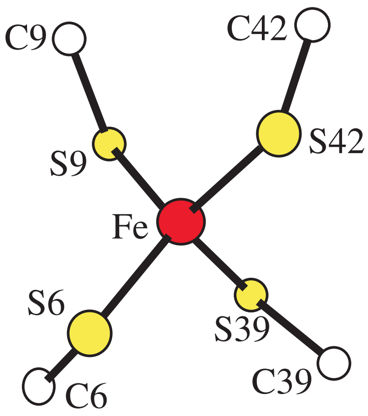

Figure 6.10: *Active site of C. pasteurianum rubredoxin. View is down the pseudo-S_4-axis and shows sulfurs and α-carbons [68].*

The electronic structure of the high spin Fe^{3+}-ion in rubredoxin has been debated extensively. Optical and EPR studies have provided most of the relevant parameters, but a number of details, such as the orientation of the interaction tensors, the sign and size of the zero field splitting have remained elusive. We have applied coherent Raman detected EPR spectroscopy to *Clostridium pasteurianum* rubredoxin, in combination with conventional EPR spectroscopy. We found a positive sign of the zero field Hamiltonian (in the usual EPR notation), with the numerical values D=46.3 GHz and E=11.6 GHz, which refines the predicted values from Mössbauer studies [65]. The ratio $(E/D)_0 = 0.25$ corresponds to a small but highly significant deviation from a fully rhombic system. In addition, an analysis of the lineshape gave clear indication of "E/D-strain", indicating that the protein is present in a number of similar conformations. Similar results have been reported from optical spectroscopy [71, 72, 73].

The orientation of the g-tensor could be identified by optically detected EPR: the EPR spectra correlate the optical anisotropy tensor with the g-tensor, clearly indicating that the optical symmetry axis is parallel to the direction of the largest g-value (the y axis in the usual EPR notation). The orientation of the optical symmetry axis with respect to the molecular structure is known from single crystal polarised absorption spectroscopy. Figure 6.10 shows the Fe-ion of rubredoxin together with the four ligands Cys(6), Cys(9), Cys(39), and Cys(42). The symmetry axis is the common bisector of the S(6)-Fe-S(42) and S(9)-Fe-S(39) bond angles, i.e. the view is down the S_4-axis. Corresponding to our results the SH-y-axis is lying parallel to this axis, while the SH-x- and z-axis lie in the plane perpendicular to this direction.

Sample heating occurred again due to high laser intensities, although the sample was highly diluted (0.14 mM). In fact rubredoxin is an ideal candidate to study the effect since the high-spin groundstate works like a built-in thermometer. Also here some more work on the optical quality of the frozen sample is necessary.

This work represents the first application of ODEPR spectroscopy to a high-spin system and to a protein with an iron-sulfur cluster. In comparison to MCD the analysis of the ODEPR spectra gave improved values for the optical polarisation of the charge transfer transitions in the 400-600 nm wavelength region. We think that it would be feasible to extend the experiment to the high-energy charge-transfer bands of the optical spectrum; for these experiments UV-laser sources are indispensable. MCD spectra were also reported for the low-energy ligand-field transitions [74]. However, since the MCD intensity of these bands is at least one order of magnitude lower than for charge-transfer transitions it is uncertain if ODEPR spectra can be measured.

Chapter 7

Conclusion and Outlook

In this thesis the application of optically detected electron paramagnetic resonance spectroscopy to the investigation of metalloproteins is presented. The results demonstrate the feasibility of this new spectroscopic technique to the study of biological systems. One of its greatest advantages lies in the possibility to measure the polarisation of optical transitions, and to relate the orientation of the optical and magnetic axis system. ODEPR can probe models for the electronic structure in order to draw conclusions about functional aspects of the protein. The technique does not require single crystals but can be used on non-oriented samples, such as frozen solutions. Determination of the optical polarisation can be achieved with much higher resolution than, for example, with MCD detected magnetisation curves.

The theoretical description of the experiment is based on the interpretation in terms of coherent Raman scattering or, alternatively, in terms of microwave modulated MCD. The compatibility of both pictures is particularly emphasized by the behaviour of the ODEPR spectra measured as function of wavelength, which clearly mirrors the behaviour of the MCD curve. Detection of transverse, microwave modulated Faraday rotation complements our theoretical model. The close relation between MCD and ODEPR proves especially useful for the analysis of the ODEPR data from the proteins under investigation, which have been studied already extensively with conventional magnetooptical methods. We demonstrate in this thesis that the theoretical approaches developed in these studies can often be extended to our experimental results.

ODEPR spectra from the copper protein *Pseudomonas aeruginosa* azurin were measured over a wide range of the optical spectrum. The shape of the spectra varies significantly with the detection wavelength. This can be attributed to the influence of the optical anisotropy, which differs from band to band of the optical spectrum. Fits of the experimental data yield exact values for the optical polarisation of the bands. The optical polarisations can be interpreted in terms of a theoretical model which was previously proposed for the closely related protein plastocyanin. We demonstrate that the data from the ligand field transitions can be readily explained in terms of D_{2d}-symmetry in direct analogy to plastocyanin. The polarisation of the charge-transfer bands is in agreement with a spin-orbit coupling model. In addition, our results enable us to identify additional bands which are not detectable in the MCD spectrum and thus to deconvolute the spectrum composed of several overlapping optical resonance lines.

For the study of the ferric high-spin protein *Clostridium pasteurianum* rubredoxin we combine data from conventional EPR and ODEPR. The analysis of the data yields that the EPR lineshape is dominated by a Gaussian variation of "E/D"-values, which corresponds to rhombicity strain. We obtain E=+11.6 GHz, D=+46.3 GHz (E/D=0.25). ODEPR spectra from several charge-transfer bands again exhibit a strong variation with the optical wavelength. With the parameters from conventional EPR we fit the ODEPR spectrum and extract the optical polarisation of the optical lines. These agree well with a theoretical model which predicts the polarisation of the charge-transfer transitions on the basis of D_{2d}-symmetry. Our analysis allows the spin Hamiltonian axes to be partially oriented relative to the optical axes; we demonstrate that the spin Hamiltonian y-axis (within the convention $E/D < 1/3$) is parallel to the optical symmetry axis and thus to the pseudo-S_4 axis of the active site. Our findings are in good agreement with previous assignments made on the basis of MCD studies.

We presented ODEPR spectra from synthetic tetrahalogeno copper complexes which serve as models for the blue copper site. These experiments, however, also indicate several problems due to strong interaction of the metal centers. Nevertheless, we think that the investigation of model compounds should be a part of future ODEPR spectroscopy. Synthetic complexes are more easily handled than protein liquids, and the electronic features frequently complement our knowledge on metalloproteins. Care must be excercised by the selection of the complex and the preparation of the sample.

The spectral resolution of ODEPR is up to two orders of magnitude higher than that of MCD. We have taken advantage of this aspect by determining the polarisation of different optical bands of a copper protein, where MCD does not provide high enough resolution due to the low g-value anisotropy. Copper species are thus ideal candidates for ODEPR spectroscopy. We propose to focus especially on other proteins with low g-value anisotropy, such as copper (for example, azurin mutants) and low-spin haem proteins.

In this thesis, we exploit the orientational selectivity of ODEPR spectroscopy. Further work should also demonstrate the chemical selectivity of the method. Application to proteins with two different centers with distinguishable magnetic and optical properties (for example, cytochrome *cd*-1) should be straightforward.

The technique shoud be readily applicable to less well-characterized proteins. Preliminary studies of 7Fe-Ferredoxin show promise for interesting results. For a protein with such a low g-value anisotropy, ODEPR spectroscopy at higher microwave frequencies will prove especially useful. A 35 GHz-ODEPR spectrometer, which is under construction at present in our group, will further improve the spectral resolution and make species with even lower g-value anisotropies accessible.

The results shown in this thesis could only be obtained by using many different laser sources to cover the range from the near infrared towards the end of the visible spectrum. For the future the number of available laser sources should even be increased. This can be realized with UV-lasers (for example, with second-harmonic generating crystal), and with laser-diodes for the infrared. In addition, some more work is necessary to improve the optical quality of the sample. Sample heating can be avoided if the transparency of the protein glass is optimally adjusted. We propose to further improve both the design of the sample cuvette and the freezing of the sample.

In the future, additional experimental techniques should also be applied. A first step in this direction is the application of microwave pulses instead of continuous wave excitation. It should also be useful to reestablish the MCD-quenching experiment which can be considered as the predecessor of the present ODEPR experiment. The combination of "longitudinal" and the "transverse" ODEPR spectroscopy might lead to a better understanding of both experiments. We could not find any evidence that spectral holeburning takes place in the protein samples. This limits the possibility of enhancing the ground state population difference by optical pumping.

Although the development of the theoretical description of ODEPR as microwave modulated MCD is at the moment still on a rather basic level, the agreement between the theoretically predicted curves and the experimental data is remarkably good. Future prospects are the extension of the microwave modulated MCD picture to a real high-spin model. In addition, it would surely be of benefit for the project to describe the experiment also mathematically in the coherent Raman picture. Interpretation of ODEPR data as coherent Raman scattering is underway at present in our group for the model compound single crystal ruby.

In conclusion, we feel that ODEPR spectroscopy has the potential to complement standard spectroscopic techniques, and to add new information to the current knowledge on metalloproteins. In this thesis we have demonstrated the applicability to well-characterized proteins. The project is now at a point where we can contribute to the biochemistry field in elucidating the electronic structure of poorly characterized proteins. However, as is frequently the case, the major challenge is not only the realisation of the experiment, but also the interpretation of the experimental data. To overcome this point, we strongly recommend to establish ODEPR spectroscopy as a cooperative project of physicists, biochemists, and theoretical chemists. Only as an interdisciplinary project will this new technique be able to develop its full potential.

Appendix A

Simulation of EPR and ODEPR Spectra

A.1 Simulation Algorithm

For a sample where all molecules are randomly oriented with respect to the magnetic field, for the evaluation of the EPR signal it is generally necessary to employ a computer program which performs the integration over all orientations. In addition, the spin Hamiltonian describing the ground state has to be diagonalized numerically for all orientations. This procedure can be simplified if the considered species is a spin 1/2-system. In this case expressions for the anisotropy of the EPR transition probability can be found in the literature [2, 3], and a diagonalisation of the Hamiltonian is needless. The basic equation describing a conventional EPR-line of a powder-like sample is for a spin 1/2 system:

$$S(\nu, B_0) \propto \int_{\theta=0}^{\theta=\pi/2} \int_{\phi=0}^{\phi=\pi/2} T(\theta,\phi)\langle g_1^2\rangle f(\theta,\phi,\sigma)\sin\theta d\theta d\phi, \tag{A.1}$$

where $T(\theta,\phi) = \tanh(g(\theta,\phi)\mu_B B_0/2kT)$ and $\langle g_1^2\rangle$ describes the anisotropy of the transition probability for a powder average. $f(\theta,\phi,\sigma)$ is the lineshape function where σ is the linewidth considered to be constant in frequency space. θ and ϕ are the two angles describing the orientation of the principal axes with respect to the magnetic field B_0, and $\sin\theta d\theta d\phi$ represents the weighting by a solid angle. The integrals over both angles represent the averaged contributions from molecules with all possible orientations. For computer simulations, the integrals over θ and ϕ have to be transformed into sums with sufficiently small angular increments. The key equation of all EPR simulation programs is therefore

$$S(\nu, B_0) = \sum_{\theta=0}^{\theta=\pi/2} \sum_{\phi=0}^{\phi=\pi/2} T(\theta,\phi)\langle g_1^2\rangle f(\theta,\phi,\sigma)\sin\theta\Delta\theta\Delta\phi. \qquad (A.2)$$

All factors which are constant during the experiment are neglected here, so that the signal amplitude is in arbitrary units. For all simulations a uniform grid of θ and ϕ-values has been used, the number of angle-steps determined by trial and error. The typical structure of an EPR simulation program is depicted in Fig. A.1. The programm is arranged in a set of nested loops. The external loop is typically the B-field, followed by integration over θ and ϕ. For a fixed B_0, θ, and ϕ the amplitude of the EPR signal is evaluated. These amplitudes are added up for all angular orientations, resulting in the EPR signal amplitude for a fixed magnetic field. Then B_0 is set to the next position, and the whole procedure is repeated, yielding the EPR resonance line as a function of magnetic field.

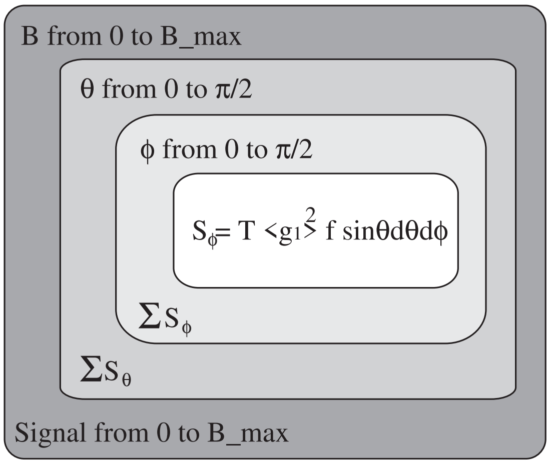

Figure A.1: *Loop structure of a simple EPR simulation program with integration over θ and ϕ.*

A.1.1 Application to Azurin

Azurin is a S=1/2 system with approximately axial symmetry. For this symmetry the system is symmetric in ϕ, so that no summation over this angle has to be performed. Two g-values have to be considered: g_z along the symmetry axis and $g_\perp$ in a plane perpendicular to that. The orientation dependent g-value is

$$g^2 = g_z^2\cos^2\theta + g_\perp^2\sin^2\theta. \qquad (A.3)$$

The transition probability can be evaluated according to

$$\langle g_1^2 \rangle = (g_\perp^2/2)(g_z^2/g^2 + 1). \tag{A.4}$$

If $f(\theta, \sigma)$ is chosen as a Lorentzian, absorption and dispersion type lineshape can be easily calculated since these curves are well defined. However, we found that for azurin a Gaussian lineshape models the EPR line better. Since the Gaussian dispersion lineshape is not available analytically, we used a numerical algorithm involving two Fourier-transformations to obtain the dispersion shape.

The Cu(II)-center shows a strong hyperfine splitting due to a nuclear spin I=3/2 of the metal ion. Hyperfine splitting is characterized by the parameter A, whereby one distinguishes A_z and $A_\perp$. The resonance condition according to first order perturbation theory is

$$\hbar\omega_0 = g\mu_B B_0 + Am_i, \tag{A.5}$$

where m_i is the magnetic quantum number for the nuclear spin, which has the allowed values -3/2, -1/2, 1/2, 3/2.

Taking into account the hyperfine coupling to first order the orientation dependent $A(\theta)$-value as a function of $g(\theta)$, g_z, $g_\perp$ A_z, and $A_\perp$ is

$$A^2 g^2 = A_z^2 g_z^2 \cos^2\theta + A_\perp^2 g_\perp^2 \sin^2\theta. \tag{A.6}$$

For the simulation of ODEPR spectra a similar approach is made using Equation 2.12. The C-parameters allow one to introduce the optical anisotropy. The integration over the angles is realized in analogy to Eq. A.2.

Please note that these programs are now part of the program "1D" ("ESR, 1/2, axial", and "ODESR, 1/2, axial"), which is available software on all MacIntosh computers of the Lehrstuhl EIII .

A.1.2 Application to Rubredoxin

Rubredoxin is a high-spin iron-sulfur protein (S=5/2). It is thus necessary to diagonalize the complete spin Hamiltonian:

$$\mathcal{H} = \mu_B g(B_x\hat{S}_x + B_y\hat{S}_y + B_z\hat{S}_z) + D(\hat{S}_z^2 - 1/3S(S+1)) + E(\hat{S}_x^2 - \hat{S}_y^2) \tag{A.7}$$

where D and E are constants describing the symmetry of the crystal field. The Hamiltonian is given as a matrix in Table A.1.

Six different energy eigenvalues are obtained. As long as the magnetic field is suffiently low, they can be grouped into three doublets well seperated

	5/2	3/2	1/2	-1/2	-3/2	-5/2
5/2	$H_z + (\frac{5}{2})^2 D$	$H_x + H_y$	$\sqrt{10}E$			
3/2	$H_x + H_y$	$H_z + (\frac{3}{2})^2 D$	$H_x + H_y$	$3\sqrt{2}E$		
1/2	$\sqrt{10}E$	$H_x + H_y$	$H_z + (\frac{1}{2})^2 D$	$H_x + H_y$	$3\sqrt{2}E$	
-1/2		$3\sqrt{2}E$	$H_x + H_y$	$H_z + (\frac{-1}{2})^2 D$	$H_x + H_y$	$\sqrt{10}E$
-3/2			$3\sqrt{2}E$	$H_x + H_y$	$H_z + (\frac{-3}{2})^2 D$	$H_x + H_y$
-5/2				$\sqrt{10}E$	$H_x + H_y$	$H_z + (\frac{-5}{2})^2 D$

Table A.1: *Matrix elements of the Hamiltonian for S=5/2, where* $H_i = g\mu_B B_i S_i$ *is the Zeeman-splitting along the principal axes.*

from each other, where each doublet represents a spin 1/2-system. For each effective S=1/2 system effective g-values g_{xeff}, g_{yeff}, and g_{zeff} are obtained. The general g-value for one doublet can be calculated according to

$$g_{eff}^2 = g_{zeff}^2 \cos^2\theta + (g_{xeff}^2 \cos^2\phi + g_{yeff}^2 \sin^2\phi)\sin^2\theta. \tag{A.8}$$

The transition probability for EPR transitions within each doublet is:

$$\begin{aligned} \langle g_1^2 \rangle &= [g_{xeff}^2 g_{yeff}^2 \sin^2\theta + g_{yeff}^2 g_{zeff}^2 (\sin^2\phi + \cos^2\phi\cos^2\theta) \\ &\quad + g_{xeff}^2 g_{zeff}^2 (\cos^2\phi + \sin^2\phi\cos^2\theta)]/2g_{eff}^2. \end{aligned} \tag{A.9}$$

Thus, the final EPR spectrum is calculated from the contribution of three Kramers doublets, where each doublet is populated according to Boltzmann's law.

As described in Chapter 6, a statistical variation of E/D gave satisfying results in order to model the exact shape of the rubredoxin EPR spectrum. This was realized by first calculating sixty spectra with fixed, but slightly varying E/D-values and by finally adding up these spectra according to a Gaussian distribution around a center value $(E/D)_0$.

The simulation of ODEPR spectra is in analogy to the EPR using Equation 2.13.

The described routines are also part of the program "1D". There is one program available which omits the E/D-strain ("ESR, 5/2" and "ODESR, 5/2"). A much more time consuming routine involves E/D-strain ("ESR, 5/2, strained" and "ODESR, 5/2, strained"). Finally, for completeness there exists a menu point which allows one to calculate a simple rhombic EPR spectrum from three input g-values ("ESR, 1/2, rhombic" and "ODESR, 1/2, rhombic").

A.2 Simplex Algorithm

An efficient way to extract parameters from an experimental curve is the use of an algorithm which minimizes the difference between the experimental and the calculated spectrum. For such purpose a Simplex-program has been employed throughout this thesis. This minimisation can lead to an optimised choice of the parameters such as g-values, linewidth, hyperfine splitting etc. However, it is important to note that the algorithm can also get stuck in a local minimum which results in a non-optimized parameter set. This has been observed especially if a lot of parameters had to be fitted. A description of the algorithm and its implementation can be found in [75].

Appendix B

Comments on the Transformation of d-Orbitals in D_{2d}- and D'_{2d}-Symmetry

The objective of this appendix is to illustrate further the conclusions drawn in Section 5 concerning the ligand-field transitions of azurin. The ligands of the copper ion impose an effective symmetry which can be characterized as D_{2d}. D_{2d}-symmetry involves a set of defined operations such as rotations and reflections. The notation of these symmetry operations is for example E for the identity operation, C_i for a rotation about an i-fold axis, σ for a reflection on a mirror plane etc. The eight symmetry operations of D_{2d} may be arranged in five classes, which are given in the upper row of Table B.1 (bold). The d-orbitals (left column) behave differently under these operations. They can be assigned to so-called irreducible representations, which are denoted as A, B, E (second column) or alternatively in another notation Γ_i. Thus, d_{xy} transforms as B_2, $d_{x^2-y^2}$ as B_1, d_{z^2} as A_1, and d_{xz}, d_{yz} as E. These findings are summarized in Fig. B.1. The half occupied orbital is B_2 (d_{xy}).

D_{2d}		$\mathbf{E}$	R	$\mathbf{2S_4}$	$2S_4R$	$\mathbf{C_2}$ C_2R	$\mathbf{2C'_2}$ $2C'_2R$	$\mathbf{2\sigma_d}$ $2\sigma_dR$
x^2+y^2, z^2	A_1, Γ_1	1	1	1	1	1	1	1
x^2-y^2	B_1, Γ_3	1	1	-1	-1	1	1	-1
xy, z	B_2, Γ_4	1	1	-1	-1	1	-1	1
$(yz, zx), (x, y)$	E, Γ_5	2	2	0	0	-2	0	0
	E', Γ_6	2	-2	$\sqrt{2}$	-$\sqrt{2}$	0	0	0
	E'', Γ_7	2	-2	-$\sqrt{2}$	$\sqrt{2}$	0	0	0

Table B.1: *Part of the D_{2d} and D'_{2d} character table (from [7], Table D1.).*

Group theory provides selection rules which determine if certain electronic transitions are allowed or not. The principle idea is the problem of deciding when integrals are necessarily zero on account of the symmetry. For this purpose the character table or a direct product table can be used (see [7], Table D2).

The electric dipole operator for a z-polarised transition transforms as B_2, whereas for xy-polarisation it transforms as E in D_{2d}. An allowed transition appears if the dipole integral contains A_1. As an example we consider the transition $A_1 \rightarrow B_2$: $A_1 \times B_2 \times B_2 = A_1$ is allowed in z-polarisation, but $A_1 \times E \times B_2 = E$ is forbidden in xy-polarisation. The allowed transitions and their polarisations are indicated by vertical arrows in Fig. B.1.

Including spin leads to the double group D'_{2d}. This allows to consider the splitting of states which are well characterized by a total angular momentum, J [76]. As a consequence, five more classes with symmetry operations are included in the character table (Table B.1, non-bold). In particular the operation R, representing a rotation about 2π, characterizes the double group. The spin transforms in this double group as E'(Γ_6). Using again the character table one finds that d_{xy} with spin transforms as $B_2 \times$ E' = E" (Γ_7), $d_{x^2-y^2}$ with spin as $B_1 \times$ E' = E" (Γ_7), d_{z^2} as $A_1 \times$ E' = E' (Γ_6), and d_{xz}, d_{yz} as E $\times$ E' = E' + E" ($\Gamma_6 + \Gamma_7$) [34, 7]. These irreducible representations are also given in Fig. B.1.

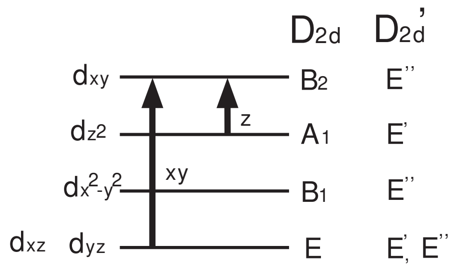

Figure B.1: *Level diagram of d-orbitals and states in D_{2d}-symmetry and D'_{2d}-symmetry. For azurin the d_{xy}-orbital is half occupied, the other orbitals are doubly occupied.*

The doubly degenerate state E contains E' + E". These states are themselves composed from the d_{xz} and d_{yz}-orbitals. The contribution from each d-orbital is listed in a vector coupling coefficient table [77]. As an example, we decompose one substate of E'(Γ_6):

$$
\begin{aligned}
E'(\Gamma_6)\,|-\rangle &= i/\sqrt{2}\,|d_{yz}\rangle\,|+\rangle - 1/\sqrt{2}\,|d_{xz}\rangle\,|+\rangle \\
&= -1/2(|2(L),1(m_l)\rangle + |2,-1\rangle)\,|+\rangle + 1/2(|2,1\rangle - |2,-1\rangle)\,|+\rangle \\
&= -\,|2(L),-1(m_l)\rangle\,|+\rangle \\
&= -\,|2(L),-1(m_l),1/2(S),1/2(m_s)\rangle \\
&\quad \text{and using tables with Clebsch-Gordan-Coeff. for ls-coupling} \\
&= -\sqrt{2/5}\,|5/2(J),-1/2(m_j),-1(L),1/2(S)\rangle - \\
&\quad \sqrt{3/5}\,|3/2(J),-1/2(m_j),-1(L),1/2(S)\rangle
\end{aligned}
$$

$|+\rangle$ and $|-\rangle$ designate up and down spin respectively. We find that the E'$|-\rangle$ ($\Gamma_6\,|-\rangle$)-state contains m_j = -1/2 only. Correspondingly we find that the E'$|+\rangle$ ($\Gamma_6\,|+\rangle$) contains m_j=+1/2, and E"$|\pm\rangle$ ($\Gamma_7\,|\pm\rangle$) has solely m_j= ± 3/2 components. Spin-orbit coupling (SOC) creates a splitting of the magnitude of the SOC-parameter λ between the two substates.

The groundstate E"(B_2) is an orbitally degenerate state. For those states the angular momentum is quenched, i.e. L is not a good quantum number anymore. Thus, the ground state is considered as a m_j = ± 1/2 Kramers doublet.

We consider first the allowed transition from the ground state E"(B_2) to the doubly degenerate state E'+E"(E), as depicted in Fig. B.2. E'(E) represents an m_j = ± 1/2 state, E"(E) an m_j = ± 3/2 state.

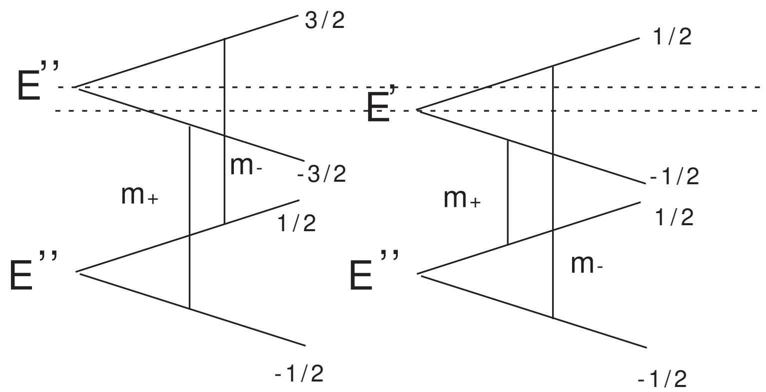

Figure B.2: *Level diagram of the transitions between the E"(B$_2$) ground state and the doubly degenerate E"+ E'(E)-state. The E"+ E'(E)-state is split due to SOC.*

The expression for a C-Term originating from randomly orientated molecules can be found in [7], Eq. 4.6.14. Since we found our transition to be xy-polarised, we neglect matrix elements containing m_z and obtain

$$C_{term} \propto -\sum_{A,J} \langle A| \mu_B(L_z + 2S_z) |A\rangle \left(\langle A| m_- |J\rangle^2 - \langle A| m_+ |J\rangle^2\right), \qquad \text{(B.1)}$$

where $\mu_B(L_z+2S_z)$ is proportional to the Zeeman-interaction, $m_\pm$ are optical transition dipoles for right and left circularly polarised light respectively, and A and J incorporate the different components of the ground and excited state. For the m_j=3/2-component we find that the C-Term is $\propto -(gm_-^2 - (-g)m_+^2) = -2gm$ and therefore negative, while for the m_j=1/2-component the C-Term is $\propto -((-g)m_-^2 - (gm_+^2)) = 2gm$ and thus positive.

The transition $B_1 \rightarrow B_2$ is group theoretically forbidden. The transition $A_1 \rightarrow B_2$ is allowed in only one polarisation, and since two orthogonal electric dipoles are required to obtain MCD, the MCD of this transition should be zero. However, spin orbit coupling is able to couple the xy-character of the fully-allowed E-states into these states. To illustrate this effect , we consider the modification of the function $|d_{x^2-y^2}\rangle$ due to SOC [59]:

$$\begin{aligned} d_{x^2-y^2}\,|+\rangle'\,(B_1\,|+\rangle) &= \left(|d_{x^2-y^2}\rangle + \frac{i\lambda}{\Delta_{xy}}\,|d_{xy}\rangle\right)|+\rangle + \left(\frac{-i\lambda}{2\Delta_{yz}}\,|d_{yz}\rangle + \frac{\lambda}{2\Delta_{xz}}\,|d_{xz}\rangle\right)|-\rangle \\ &= \left(|d_{x^2-y^2}\rangle + \frac{i\lambda}{\Delta_{xy}}\,|d_{xy}\rangle\right)|+\rangle - \frac{\lambda}{\sqrt{2}\Delta}E''(E)\,|+\rangle \end{aligned}$$

where $\Delta = \Delta_{xz} \simeq \Delta_{yz}$ is the energy difference between these states and $|d_{x^2-y^2}\rangle$. The E" (B_1)-state gains therefore only a contribution from the E"(E)-state. Since the transition E"(E)→E"(B_2) has negative, xy-polarised MCD, E"(B_1)→E"(B_2) will exhibit the same MCD characteristic. A similar analysis yields the polarisation and sign of the optical transition E' (A_1)→E"(B_2) as depicted in Fig. 5.9.

Appendix C

Additional Data from Cu-Acetate Films

For the sake of completeness in this chapter all experimental data from the copper-acetate films is summarized which has not been presented in the main body of the text. For the MCD-spectrum in the visible range of $(Et_4N)_2Cu(II)Br_4$ see Fig. 4.3. For the MCD-spectrum in the infrared range of $(Et_4N)_2Cu(II)Cl_4$ see Fig. 5.11.

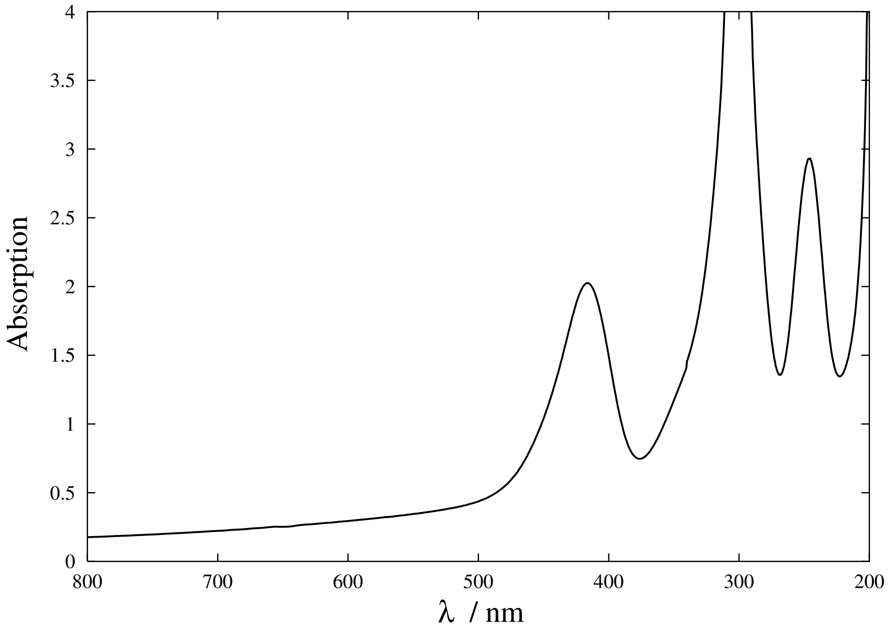

Figure C.1: *Room temperature absorption of a prototypical $((Et_4N)_2Cu(II)Cl_4)$-film.*

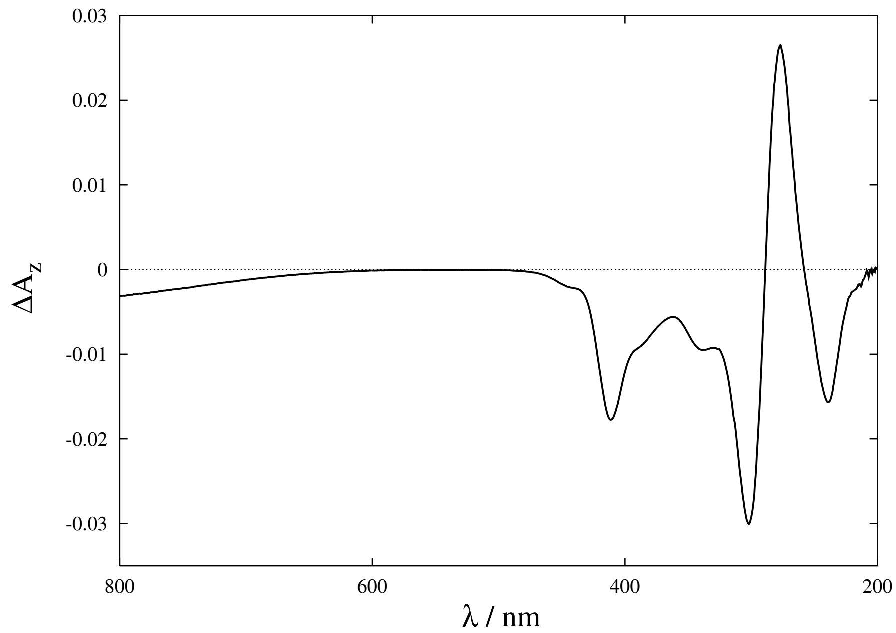

Figure C.2: *MCD spectrum in the visible of a prototypical $((Et_4N)_2Cu(II)Cl_4)$-film at 5 Tesla, 1.6 K.*

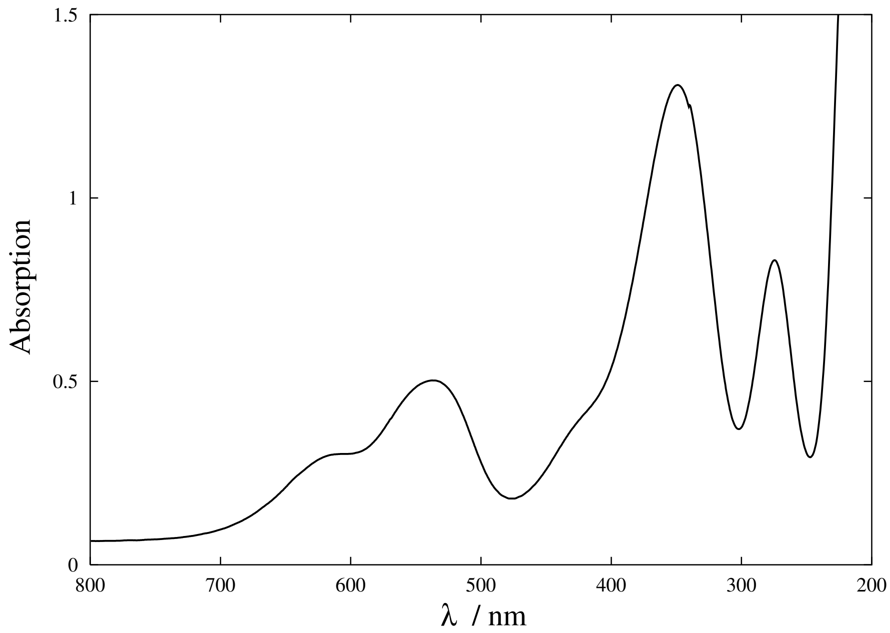

Figure C.3: *Room temperature absorption of a prototypical $((Et_4N)_2Cu(II)Br_4)$-film.*

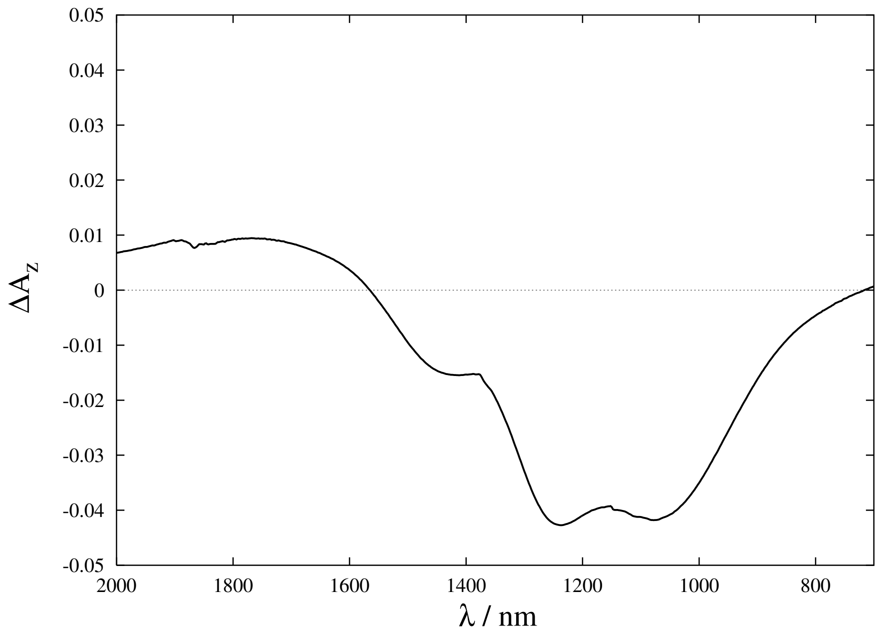

Figure C.4: *MCD spectrum in the infrared of a prototypical $((Et_4N)_2Cu(II)Br_4)$-film at 5 Tesla, 1.6 K.*

Appendix D

Publications on the Subject

S.J. Bingham, D. Suter, A. Schweiger, and A.J. Thomson, *Optical detection of transition metal ion electron paramagnetic resonance by coherent Raman spectroscopy*, Chem. Phys. Letters, 266:543, 1997.

S.J. Bingham, B. Börger, D. Suter, and A.J. Thomson, *The design and sensitivity of microwave frequency optical heterodyne receivers*, Rev. Sci. Instrum., 69:3403, 1998.

B. Börger, S.J. Bingham, J. Gutschank, M.O. Schweika, D. Suter, and A.J. Thomson, *Optically detected paramagnetic resonance by microwave modulated magnetic circular dichroism*, J. Chem. Phys., 111:8565, 1999.

S.J. Bingham, B. Börger, J. Gutschank, D. Suter, and A.J. Thomson, *Probing the electronic structure of transition metal ion centres in proteins by coherent Raman detected electron paramagnetic resonance spectroscopy*, JBIC, 5:35, 2000.

S.J. Bingham, B. Börger, J. Gutschank, D. Suter, and A.J. Thomson, *MCD anisotropy from coherent Raman detected EPR spectroscopy: Application to spin-1/2 transition metal centers in proteins*, J. Chem. Phys., 113:4331, 2000.

M.O. Schweika, S.J. Bingham, B . Börger, J. Gutschank, D. Suter, and A.J. Thomson, *Optically detected paramagnetic resonance on ruby and cytochrome c*, 30th Congress Ampere, 2000, in press.

B. Börger, S.J. Bingham, J. Gutschank, D. Suter, and A.J. Thomson, *Deconvolution and assignment of different optical transitions of the blue copper*

protein azurin from optically detected EPR spectroscopy, J. Am. Chem. Soc., 123:2334, 2001.

B. Börger and D. Suter, *Magnetic and Optical Anisotropy of Clostridium Pasteurianum Rubredoxin from Optically Detected Electron Paramagnetic Resonance*, J. Chem. Phys., 2001, submitted.

Bibliography

[1] A. Abragam. *Nuclear Magnetism.* Oxford University Press, Oxford, 1961.

[2] A. Abragam and B. Bleaney. *Electron Paramagnetic Resonance of Transition Ions.* Oxford University Press, Oxford, 1961.

[3] J. R. Pilbrow. *Transition Ion Electron Paramagnetic Resonance.* Oxford University Press, Oxford, 1990.

[4] R. Kirmse and J. Stach. *ESR-Spektroskopie, Anwendungen in der Chemie.* Akademie Verlag, Berlin, 1985.

[5] C. P. Slichter. *Principles of Magnetic Resonance.* Springer, Berlin, 1996.

[6] P. J. Stephens. *Adv. Chem. Phys.*, 52:3489, 1976.

[7] S.B. Piepho and P.N. Schatz. *Group Theory in Spectroscopy, with Applications to Magnetic Circular Dichroism.* Wiley, New York, 1983.

[8] J. C. Sutherland. *Methods in Enzymology*, 246:110, 1995.

[9] A. J. Thomson, M. R. Cheesman, and S. J. George. *Methods in Enzymology*, 226:199, 1993.

[10] P.N. Schatz, R.L. Mowery, and E.R. Krausz. *Mol.Phys.*, 35:1537, 1978.

[11] F. Neese and E.I. Solomon. *Inorg. Chem.*, 38:1847, 1999.

[12] S. J. Bingham, J. Gutschank, B. Börger, D. Suter, and A.J. Thomson. *J. Chem. Phys.*, 113:4331, 2000.

[13] S. Geschwind. *Electron Paramagnetic Resonance.* Plenum Press, New York, 1972.

[14] C.A. Moore and R.A. Satten. *Phys. Rev. B*, 7:1753, 1972.

[15] J.M. Daniels and K.E. Rieckhoff. *Can. J. Phys.*, 38:605, 1960.

[16] C.P. Barrett, J. Peterson, C. Greenwood, and A.J. Thomson. *J. Am. Chem. Soc.*, 108:3170, 1986.

[17] S.J. Bingham. *MCD and EPR of Transition Ions.* PhD thesis, University of East Anglia, 1993.

[18] N. Bloembergen, P. S. Pershan, and L. R. Wilcox. *Phys. Rev.*, 120:2014, 1960.

[19] L. L. Chase. *Phys. Rev. Letters*, 21:888, 1968.

[20] S. J. Bingham, D. Suter, A. Schweiger, and A. J. Thomson. *Chem. Phys. Letters*, 266:543, 1997.

[21] B. Börger, S. J. Bingham, J. Gutschank, D. Suter, and A.J. Thomson. *J. Chem. Phys.*, 111:8565, 1999.

[22] S. J. Bingham, B. Börger, J. Gutschank, D. Suter, and A.J. Thomson. *JBIC*, 5:30, 2000.

[23] D. Suter. *The Physics of Laser-Atom Interactions.* Cambridge University Press, Cambridge, 1997.

[24] R. Neuhaus, M.J. Sellars, S.J. Bingham, and D. Suter. *Phys. Rev. A*, 58:4961, 1998.

[25] J. Friedrich, H. Scheer, B. Zickendraht-Wendelstadt, and D. Haarer. *J. Chem. Phys.*, 74:2260, 1980.

[26] J. Gafert, J. Friedrich, and F. Parak. *J. Chem. Phys.*, 99:2478, 1993.

[27] T.H. Wilmshurst. *Electron Spin Resonance Spectrometers.* Adam Hilger Ltd, London, 1976.

[28] Oxford Instruments, England. *Spectromag system, Operator's handbook*, 1997.

[29] S. J. Bingham, B. Börger, D. Suter, and A. J. Thomson. *Rev. Sci. Instrum.*, 69:3403, 1998.

[30] E. I. Solomon, J. B. Baldwin, and M. D. Lowery. *Chem. Rev.*, 92:521, 1992.

[31] S.J. Lippard and J.M. Berg. *Bioanorganische Chemie.* Spektrum Akademischer Verlag, Heidelberg, 1995.

[32] B. G. Karlsson, T. Pascher, M. Nordling, R. H. A. Arvidsson, and L. G. Lundberg. *FEBS Letters*, 246:211, 1989.

[33] J.C. Rivoal and B. Briat. *Compt. Rend. Ac. Sc.*, 271:1166, 1970.

[34] J.C. Rivoal and B. Briat. *Mol. Phys.*, 27:1081, 1974.

[35] V.S. Oganesyan, S.J. George, M.R. Cheesman, and A.J. Thomson. *J. Chem. Phys.*, 110:762, 1999.

[36] J. Meyer, J. Gaillard, and M. Lutz. *Biochem. Biophys. Res. Com.*, 212:827, 1995.

[37] H. Fridén, M. R. Cheesman, L. Hederstedt, K. K. Andersson, and A. J. Thomson. *Biochim. Biophys. Acta*, 1041:207, 1990.

[38] J. Gutschank. Diploma thesis, University of Dortmund,unpublished. 1999.

[39] A. Dwivedi, W.A.Jr. Toscano, and P. Debrunner. *Biochim. Biophys. Acta*, 576:502, 1979.

[40] B. Börger. Diploma thesis, University of Dortmund,unpublished. 1998.

[41] N. Foote, J. Peterson, P. M. A. Gadsby, C. Greenwood, and A. J. Thomson. *Biochem. Journal*, 223:369, 1984.

[42] A.K. Zvezdin and V.A. Kotov. *Modern Magnetooptics and Magnetooptical Materials.* Institute of Physics Publishing, Bristol, 1997.

[43] M.O. Schweika-Kresimon. Unpublished results.

[44] A. G. Sykes. *Advances in Inorganic Chemistry*, 36:377, 1991.

[45] P. J. Kraulis. *J. Appl. Crystall.*, 24:946, 1991.

[46] J.W.A. Coremans, O.G. Poluektov, E.J.J. Groenen, G.W. Canters, H. Nar, and A. Messerschmidt. *J. Am. Chem. Soc.*, 116:3097, 1994.

[47] A. A. Gewirth and E. I. Solomon. *J. Am. Chem. Soc.*, 110:3811, 1988.

[48] E. I. Solomon, J.W. Hare, D.M. Dooley, J.H. Dawson, P.J. Stephens, and H.B. Gray. *J. Am. Chem. Soc.*, 102:168, 1980.

[49] A. Aqualino, A.S. Brill, G.F. Bryce, and B.S. Gerstman. *Phys. Rev. A*, 44:5257, 1991.

[50] W.E. Antholine, M.H. Phillip, and D.R. McMillin. *Biophys. J.*, 64:267, 1993.

[51] K. W. Penfield, R. R. Gay, R. S. Himmelwright, N. C. Eickman, V. A. Norris, H. C. Freeman, and E. I. Solomon. *J. Am. Chem. Soc.*, 103:4382, 1981.

[52] S. Larsson, B. Anders, and L. Sjölin. *J. Chem. Phys.*, 99:4860, 1995.

[53] J.W.A. Coremans, O.G. Poluektov, E.J.J. Groenen, G.W. Canters, H. Nar, and A. Messerschmidt. *J. Am. Chem. Soc.*, 118:12141, 1996.

[54] K. Pierloot, J.O.A. De Kerpel, U. Ryde, and B.O. Roos. *J. Am. Chem. Soc.*, 119:218, 1997.

[55] F.A. Cotton. *Chemical Applications of Group Theory*, chapter 9. Wiley, New York, 1971.

[56] C.J. Ballhausen. *Introduction to Ligand Field Theory*, chapter 6. Mac Graw-Hill, New York, 1962.

[57] L.B. LaCroix, D.W. Randall, A.M. Nersissian, C.W.G Hoitink, G.W. Canters, J.S. Valentine, and E.I. Solomon. *J. Am. Chem. Soc.*, 120:9621, 1998.

[58] A. Abragam and B. Bleaney. *Electron Paramagnetic Resonance of Transition Ions*, chapter 7. Oxford University Press, Oxford, 1961.

[59] C.J. Ballhausen. *Introduction to Ligand Field Theory.* Mac Graw-Hill, New York, 1962.

[60] J. Ferguson. *J. Chem. Phys.*, 40:3406, 1964.

[61] S.R. Desjarding, K.W. Penfield, S.L. Cohen, R.L. Musselman, and E.I. Solomon. *J. Am. Chem. Soc.*, 105:4590, 1983.

[62] C.P. Barrett. *Optical-Microwave Double Resonance.* PhD thesis, University of East Anglia, 1985.

[63] J. Peisach, W.E. Blumberg, E.T. Lode, and M.J. Coon. *J. Biol. Chem.*, 246:5877, 1971.

[64] A. Abragam and B. Bleaney. *Electron Paramagnetic Resonance of Transition Ions*, chapter 3. Oxford University Press, Oxford, 1961.

[65] C. Schulz and P.G. Debrunner. *J. de Physique, Colloque C6*, 37:153, 1976.

[66] W.E. Blumberg and J. Peisach. *Ann. New York Acad. Sci.*, 222:539, 1973.

[67] B. Börger, S. J. Bingham, J. Gutschank, D. Suter, and A.J. Thomson. *J. Am. Chem. Soc.*, 123:2334, 2001.

[68] M.S. Gebhard, J.C. Deaton, S.A. Koch, M. Millar, and E.I. Solomon. *J. Am. Chem. Soc.*, 112:2217, 1990.

[69] D.E. Bennett and M.K. Johnson. *Biochem. Biophys. Acta*, 911:71, 1986.

[70] W. Eaton, W.A. Lovenberg. The iron-sulfur complex in rubredoxin. In *Iron-Sulfur Proteins*. Academic Press, 1973.

[71] J. Schlichter, J. Friedrich, L. Herenyi, and J. Fidy. *J. Chem. Phys.*, 112:3045, 2000.

[72] H. Frauenfelder, S.G. Sligar, and P.G. Wolynes. *Science*, 254:1598, 1991.

[73] W. Köhler, J. Friedrich, and H. Scheer. *Phys. Rev. A*, 37:660, 1988.

[74] V.S. Oganesyan and A.J. Thomson. *J. Chem. Phys.*, 113:5003, 2000.

[75] W.H. Press. *Numerical Recipes in Pascal.* Cambridge University Press, Cambridge, 1989.

[76] F.A. Cotton. *Chemical Applications of Group Theory.* Wiley, New York, 1971.

[77] G.F. Koster, J.O. Dimmock, R.G. Wheeler, and H. Statz. *Properties of the 32 Point Groups.* MIT Press, Cambridge, Massachusetts, 1963.

Acknowledgement

Zu großem Dank verpflichtet bin ich Professor D. Suter für die Bereitstellung dieses interessanten Themas mit interdisziplinärem Charakter, sein stetes Interesse am Fortgang dieser Arbeit und seine fortwährende Unterstützung.

I wish to thank Professor A.J. Thomson, University of East Anglia, U.K. for the possibility to work with his laboratory equipment not only in Norwich, but also during the ODEPR experiments in Dortmund, and for the provision of the metalloprotein samples.

Den Mitarbeitern am Lehrstuhl EIII möchte ich für ihre Hilfsbereitschaft und natürlich auch für das angenehme Arbeitsklima danken, welches viel zum Gelingen dieser Arbeit beigetragen hat. Besonders richtet sich mein Dank an Jörg Gutschank und Marc-Oliver Schweika-Kresimon für die gute Zusammenarbeit über mehrere Jahre. Rudolf Neuhaus war stets eine große Hilfe beim Aufbau von Farbstofflasern, so wie Björn Lenzmann und Marcus Eickhoff mich an ihrer Expertise in Sachen Laserdioden haben teilhaben lassen.

I am indebted to Dr. Stephen J. Bingham who initiated the ODEPR experiment during his postdoc time in Dortmund and who was my supervisor at the beginning of my PhD. I wish him good luck for his career in the UK.

I am especially grateful to Dr. Vasily Oganesyan for many helpful discussions and to Dr. Myles Cheesman for experimental assistance.

Bei Dr. Eckhard Bill vom MPI Mühlheim bedanke ich mich für die Möglichkeit, X-Band ESR-Spektren von Azurin und Kupferacetat-Filmen messen zu können.

Ich danke der Arbeitsgruppe von Professor Goody am MPI für molekulare Physiologie dafür, daß ich mit ihrer Hilfe die Rubredoxin-Probe anfertigen konnte.

An Professor H.J. Weber geht mein Dank für die Nutzungsmöglichkeit des Absorptionspektrometers in seinem Labor.

Dirk Schemionek und Gisela Pike vom Präparationslabor danke ich für ihre Hilfe bei der Herstellung der Kupferacetat-Filme und bei vielen anderen kleinen und grossen technischen Problemen.

Meinem Mann Hartmut und meinen Eltern danke ich herzlich für die tatkräftige Unterstützung während meiner gesamten Promotionszeit.

Das Graduiertenkolleg Festkörperspektrokopie und die Deutsche Forschungsgesellschaft (Proj.Nr. SU 192/9 -1) haben dieses Projekt finanziell unterstützt.